Technical Report Documentation Page

1. Report No.	2. Government Accession No.	3. Recipient's Catalog No.
SWUTC/14/600451-00009-1		

4. Title and Subtitle	5. Report Date
SUSTAINABILITY OF TRANSPORTATION STRUCTURES USING COMPOSITE MATERIALS TO SUPPORT TRADE AND GROWTH	June 2014
	6. Performing Organization Code

7. Author(s)	8. Performing Organization Report No.
Shobeir Pirayeh Gar, Stefan Hurlebaus, John B. Mander, Wesley Cummings, Michelle J. Prouty, and Monique H. Head	SWUTC 600451-00009-1

9. Performing Organization Name and Address	10. Work Unit No. (TRAIS)
Texas A&M Transportation Institute College Station, Texas 77843-3135	11. Contract or Grant No. DTRT12-G-UTC06

12. Sponsoring Agency Name and Address	13. Type of Report and Period Covered
Southwest Region University Transportation Center Texas A&M Transportation Institute College Station, Texas 77843-3135	Research Report: January 2013–January 2014
	14. Sponsoring Agency Code

15. Supplementary Notes

Supported by a grant from the U.S. Department of Transportation University Transportation Centers Program and general revenues from the State of Texas.

16. Abstract

Corrosion-induced deterioration of steel rebar is one of the main reasons for repair and rehabilitation programs for conventional steel-reinforced concrete bridge decks. According to the National Association of Corrosion Engineers (NACE), of all bridges in the United States, over 50 percent are constructed of conventional steel-reinforced or prestressed concrete, and one in three bridges is considered structurally deficient or functionally obsolete due to corrosion of steel reinforcement. NACE has estimated the annual cost of corrosion-related maintenance of highway bridges in the United States at $8.3 billion.

To overcome corrosion-induced structural issues, researchers have introduced and applied fiber-reinforced polymer (FRP) bars, over the past couple of decades, as a corrosion-resistant candidate for either conventional reinforcing steel or prestressing strands. High strength-to-weight ratio, corrosion resistance, and accelerated construction due to ease of placement of the bars and implementation are the special characteristics that make these bars an appealing alternative for either steel-reinforcing bars or prestressing strands.

This report presents the experimental and analytical investigations of structural performance of a full-scale American Association of State Highway and Transportation Officials (AASHTO) I-girder Type I, reinforced and prestressed with aramid-fiber-reinforced polymer (AFRP) bars, where the bridge girder is composite with a topping deck. The major objectives of this research included evaluating (1) the constructability, (2) the load and deformation capacities under either flexure or shear tests, and (3) the structural performance per AASHTO load and resistance factor design (LRFD) criteria.

The results of this research confirm the adequate strength and deformation capacities of the composite girder, satisfying the AASHTO LRFD criteria. The flexural capacity of the composite girder was about 1582 kNm (1167 kft.), which is 20 percent greater than the maximum factored load, 1326 kNm (978 kft.), per AASHTO LRFD. Under the flexure test, the failure mode of the girder was recognized as the tendon rupture in the bottom flange, where the maximum compressive strain in the topping deck did not reach a failure value equal to −0.003. Such a failure mode was expected because it is not practical to fit too many FRP bars within the bottom flange of the girder to over-reinforce the section and change the failure mode from tendon rupture to concrete crushing in the top fiber of the section.

17. Key Words	18. Distribution Statement
Bridge Girder, Aramid-Fiber-Reinforced Polymer (AFRP), I-Girder, Composite Action, Composite Material	No restrictions. This document is available to the public through NTIS: National Technical Information Service Alexandria, Virginia 22312 http://www.ntis.gov

19. Security Classif.(of this report)	20. Security Classif.(of this page)	21. No. of Pages	
Unclassified	Unclassified	126	

SUSTAINABILITY OF TRANSPORTATION STRUCTURES USING COMPOSITE MATERIALS TO SUPPORT TRADE AND GROWTH

by

Shobeir Pirayeh Gar
Texas A&M University

Stefan Hurlebaus
Texas A&M University

John B. Mander
Texas A&M University

Wesley Cummings
Texas A&M University

Michelle J. Prouty
Texas A&M University

and

Monique H. Head
Texas A&M University

Report SWUTC/14/600451-00009-1
Project 600451-00009 and 161206
Project Title: Sustainability of Transportation Structures Using Composite Materials to Support Trade and Growth

Southwest Region University Transportation Center
Texas A&M Transportation Institute
College Station, Texas 77843-3135

June 2014

DISCLAIMER

The contents of this report reflect the findings and viewpoints of the authors, who are responsible for the content and fidelity of the data presented. This document is disseminated under the sponsorship of the U.S. Department of Transportation University Transportation Centers Program in the interest of information exchange. This report does not constitute a standard, specification, or regulation. The U.S. Government assumes no liability for the contents or use thereof. The engineer in charge was Stefan Hurlebaus, Ph.D.

ACKNOWLEDGMENTS

The authors recognize that support for this research was provided by a grant from the U.S. Department of Transportation University Transportation Centers Program to the Southwest Region University Transportation Center, which is funded, in part, with general revenue funds from the State of Texas. This project was conducted at Texas A&M University as part of Project 600451-00009 and 161206, Sustainability of Transportation Structures Using Composite Materials to Support Trade and Growth. The authors would like to express appreciation for the support provided by the Texas A&M Transportation Institute. The authors would like to thank Dr. P. Keating and M. Potter of the Civil Engineering High Bay Structural and Materials Testing Laboratory at Texas A&M and all the students who worked on the project. The research team would also like to acknowledge the contribution made by Heldenfels Company of San Marcos, Texas, where the fabrication of the girder and topping deck was done.

TABLE OF CONTENTS

LIST OF FIGURES

LIST OF TABLES

EXECUTIVE SUMMARY

Corrosion-induced deterioration of steel rebar is one of the main reasons for repair and rehabilitation programs for conventional steel-reinforced concrete bridge decks. According to the National Association of Corrosion Engineers (NACE 2013), of all bridges in the United States, over 50 percent are constructed of conventional steel-reinforced or prestressed concrete, and one in three bridges is considered structurally deficient or functionally obsolete due to corrosion of steel reinforcement. NACE has estimated the annual cost of corrosion-related maintenance of highway bridges in the United States at $8.3 billion.

To overcome corrosion-induced structural issues, researchers have introduced and applied fiber-reinforced polymer (FRP) bars, over the past couple of decades, as a corrosion-resistant candidate for either conventional reinforcing steel or prestressing strands. High strength-to-weight ratio, corrosion resistance, and accelerated construction due to ease of placement of the bars and implementation are the special characteristics that make these bars an appealing alternative for either steel-reinforcing bars or prestressing strands.

Extensive research has been conducted on the structural performance of FRP-reinforced concrete members such as beams and slabs; however, less attention has been paid to full-scale FRP-reinforced concrete bridge girders in composite action with the bridge deck, where realistic dimensions, structural details, and girder-to-slab connections are all physically modeled. Accounting for the effect of composite action between the bridge girder and the topping deck can drastically impact the structural performance of the girder, including the load and deformation capacities as well as the failure mode. Furthermore, full-scale modeling with real dimensions and structural details helps to more accurately evaluate the structural performance and constructability, and to provide more reliable design guidelines for engineers.

This report presents the experimental and analytical investigations of structural performance of a full-scale American Association of State Highway and Transportation Officials (AASHTO) I-girder Type I, reinforced and prestressed with aramid-fiber-reinforced polymer (AFRP) bars, where the bridge girder is composite with a topping deck. The major objectives of this research included evaluating:

- The constructability.
- The load and deformation capacities under either flexure or shear tests.
- The structural performance per AASHTO load and resistance factor design (LRFD) criteria.

Only the instantaneous structural behavior, or short-term response, is considered in this research. This briefly includes the load and deformation capacities under monotonically increasing load, failure mode, and crack pattern. The long-term performance of the composite girder is beyond the scope of the present project.

This research was conducted over a 24-month period. The specimen was constructed at a prestressing plant in San Marcos, Texas, and tested at the High Bay Structural and Materials Testing Laboratory on the campus of Texas A&M University. The bridge girder was composed of self-consolidating concrete with 24 prestressed and eight non-prestressed AFRP bars. For shear reinforcement, AFRP bars were bent to make R-shape stirrups. The bridge deck consisted of a 203-mm (8-in.) thick conventional steel-reinforced concrete slab. For the flexure test, the bridge girder was simply supported and tested under a four-point loading configuration, where the moment-curvature relationship, flexural load and deformation capacities, and failure mode were studied. For the shear test, the uncracked parts of the girder at both ends were tested under a three-point loading configuration, where the shear load and deformation capacities, maximum strain in the girder's web, development length, and failure modes were studied. The results of these tests were compared with an identical system, except for being reinforced with conventional steel rebar and prestressing strands—the controlling specimen.

The results of this research confirm the adequate strength and deformation capacities of the composite girder, satisfying the AASHTO LRFD criteria. The flexural capacity of the composite girder was about 1582 kNm (1167 kft.), which is 20 percent greater than the maximum factored load, 1326 kNm (978 kft.), per AASHTO LRFD. Under the flexure test, the failure mode of the girder was recognized as the tendon rupture in the bottom flange, where the maximum compressive strain in the topping deck did not reach a failure value equal to −0.003. Such a failure mode was expected because it is not practical to fit too many FRP bars within the bottom flange of the girder to over-reinforce the section and change the failure mode from tendon rupture to concrete crushing in the top fiber of the section. Although AFRP bars behave linearly

and the compressive concrete could not develop considerable inelastic stresses, significant flexural deformability was observed after the cracking and prior to failure as a result of the low elastic modulus of AFRP bars, about one-third that of steel. This was confirmed by the load-deflection response and extensive flexural cracks concentrated at the midspan and propagating toward the supports. Full composite action between the girder and the topping deck was achieved, where no local failure was seen at the girder-to-deck interface, confirming the adequacy of the shear connections.

Using self-consolidating concrete, which inherently does not need vibration to place, along with light-weight reinforcing AFRP bars provided easy and accelerated construction that can be effectively applied in practice. The only challenging part of the construction was using the applicable and reliable anchorage system for prestressing AFRP bars. For this purpose, the researchers developed and extensively tested a special anchorage system to improve the gripping capacity and sustainability performance. A successful prestressing operation was conducted, where only a couple of failures occurred at the bar-to-anchorage interface. The replacement of the failed bars was quickly performed, and the prestressing was repeated, this time with lower prestressing forces to avoid further failure.

1 INTRODUCTION

1.1 Research Motivation

Critical infrastructure in the United States, particularly roadways and bridges, are deteriorating and becoming a nationwide problem due to corrosion of the reinforcing steel as a result of aging and aggressive environments. This is a major concern because the economy of the United States is greatly tied to its transportation system, where bridges are an integral part of the transportation network that connects people and businesses. Steel corrosion leads to member degradation, endangers structural integrity, and may even cause catastrophic failures. The corrosion decay in concrete structures has continued to be a challenge in the scientific and engineering communities. In 1997, the Intermodal Surface Transportation Efficiency Act (ISTEA) spent $2.5 billion for the Highway Bridge Replacement Program, where a majority of the funds went toward replacement or rehabilitation of bridge decks that were damaged by corrosion deterioration. This problem has led to a serious need for finding alternative design strategies that can reduce the likelihood of corrosion decay in concrete structures and the subsequent maintenance cost.

The main idea to overcome corrosion-induced deterioration is the use of high-performance materials that have inherent properties to provide durable corrosion protection and prevent premature spalling or corrosion-induced cracking. Recent advancements in the field of material science have resulted in the development of new products that can be used in many areas of civil engineering, where conventional materials have failed to provide satisfactory service life. In particular, aramid-fiber-reinforced polymer (AFRP) materials, which present unique properties such as very high strength-to-weight ratio and corrosion resistivity, have received significant attention and have been considered an ideal alternative for steel. AFRP bars can be manufactured as reinforcing or prestressing bars for reinforced concrete (RC) or prestressed reinforced concrete (PRC) structures, sheets and laminates for external strengthening of beams, slabs and masonry walls, wraps and shells for confinement of columns, etc.

To this end, considerable research has been conducted on the structural behavior of prestressed and non-prestressed fiber-reinforced polymer (FRP) concrete beams and slabs; however, less attention has been paid to the structural performance of full-scale FRP RC or PRC

bridge girders in composite action with the topping deck. Accounting for the effect of composite action between the bridge girder and the topping deck can drastically impact the structural performance of the girder, including the load and deformation capacities as well as the failure mode. Furthermore, full-scale modeling with real dimensions and structural details helps to more accurately evaluate the structural performance and constructability, and to provide more reliable design guidelines for engineers. These knowledge gaps are the main motivation behind the present research.

This research is intended to experimentally and analytically evaluate the structural performance and constructability of a full-scale concrete bridge girder reinforced and prestressed with AFRP bars through flexure and shear tests.

1.2 Research Need

As stated, most of the investigations on FRP-reinforced concrete members have been focused on individual beams or slabs, and little research has been performed on the structural performance of a full-scale bridge girder with realistic dimensions, boundary conditions, and structural details. One of the main items that must be physically modeled is the bridge topping deck. The bridge topping deck provides a composite action with the bridge girder, which substantially impacts the structural capacity and failure mode of the bridge girder. Only under such circumstances are the experimental and analytical results reliable. Design guidelines can be established based on these results, and the overall system can be recommended for practical use.

On the other hand, the analysis and design process of FRP concrete bridge girders are not as clear as that of the conventional steel case since FRP bars do not have a yielding point and behave linearly up to rupture; hence, the classic methods of plastic analysis may not be applicable. Moreover, since FRP bars have a brittle failure mode, it is typically desired to over-reinforce the section so that concrete crushing, rather than tendon rupture, is the dominant failure mode. This may not be practical because it is very difficult to fit too many FRP bars in the bottom flange of the bridge to exceed the balance ratio; hence, further research is essential to clarify the actual failure mode.

1.3 Research Objectives

This research evaluated the structural performance of a full-scale concrete bridge girder reinforced and prestressed with AFRP bars in composite action with the bridge deck. The main objectives of the present research project were to:

- Evaluate the constructability.
- Experimentally and analytically evaluate the load and deformation capacities through flexure and shear tests.
- Evaluate the structural performance per American Association of State Highway and Transportation Officials (AASHTO) load and resistance factor design (LRFD) criteria.

1.4 Research Approach

Experimental investigation was the main approach taken in this project to study the structural performance of a full-scale bridge girder reinforced and prestressed with AFRP bars. The experimental results were subsequently checked with analytical solutions. In the first phase of the project, the mechanical characteristics of the material including self-consolidating concrete and AFRP bars were tested. Given the material characteristics, the bridge girder (AASHTO I-girder Type I) was analyzed and designed per AASHTO LRFD criteria. The topping deck was assumed to be in composite action with the bridge girder. Upon specifying the reinforcement layout and details, the construction process was determined. The major construction challenge was the prestressing operation of the AFRP bars because these bars in transverse direction were not as strong as in the longitudinal direction; hence, the gripping stress of the anchorage could have resulted in premature failure. Therefore, before starting to construct the girder in the precast plant, a practical and reliable anchorage system was developed and tested in the laboratory.

Once the prestressing system was successfully developed and tested, the full-scale AASHTO I-girder Type I, along with its topping deck, was constructed in the precast plant. The specimen was then transported to the High Bay Structural and Materials Testing Laboratory at Texas A&M University. The flexure test was first conducted under a monotonically increasing load with a four-point configuration until failure was observed. Then two shear tests were performed at both uncracked ends of the girder close to the supports.

The experimental results were first checked with analytical solutions to verify the results and to evaluate the accuracy of the numerical analyses and hand calculations based on classic theories of strength of materials. Then, the results were evaluated to see if the AASHTO LRFD criteria were met. Finally, the results were compared with the conventional steel-reinforced concrete system.

1.5 Research Background

Most of the research on the application of FRP bars in reinforced and prestressed concrete has focused on beams. McKay and Erki (1993) investigated the flexural behavior of concrete beams prestressed with AFRP bars. One of the major findings of this research was that FRP prestressed beams should only be designed as fully prestressed members; otherwise, fretting of the rod surface decreases the bond strength between the rods and the concrete, leading to concrete horizontal splitting failures at the level of the rods.

Naaman et al. (1993) tested two T-beams partially prestressed with carbon fiber polymer (CFRP) strands. The beams had conventional steel reinforcing bars in addition to CFRP. An accidental CFRP strand failure during stressing and anchoring was experienced, which suggested that extreme care should be taken with prestressing operations. A comparison with similar beams using steel strands showed that for the same global reinforcing index, the cracking load is lower and the crack width is larger, while the beam stiffness is smaller when CFRP strands are used. The load-deflection responses of the beams prestressed or partially prestressed with FRP bars can be predicted with reasonable accuracy using conventional methods of equilibrium, strain compatibility and material stress-strain relationships.

Abdelrahman et al. (1995) tested four prestressed concrete T-beams pretensioned with FRP cables as girders of the first smart highway bridge built in Canada. The authors concluded that the behavior of the beams with carbon fiber composite cables (CFCC) and leadline cables were bilinearly elastic up to failure. Unloading of the beams showed an elastic response and negligible residual deformations. Beams pretensioned by FRP normally exhibit considerable warning before failure due to the presence of large, extensively distributed cracks and large deflection before failure. The authors found that in beams with a wide flange in the compression zone, such as T-sections, failure normally occurs by rupture of the FRP bars. The authors also proposed a

ductility method providing an adequate model to measure ductility of the beams prestressed by FRP bars.

Shahawy and Beitelman (1995) studied the static flexural response of members pretensioned with multiple layered AFRP bars. The authors concluded that ARAPREE® bars can be successfully employed as prestressing strands; however, durability and long-term performance should be investigated. The double-tee beam that the authors tested exhibited excessively large deformations in the post-cracking stage and had excellent deformation recovery of about 95 percent upon removal of the applied load, which corresponds to about 80 percent of the theoretical ultimate load. Methods for evaluating the flexural strength of an FRP prestressed beam were published by Dolan and Burke (1996). Their paper covered the derivation of the flexural strength equations and provided a calibration against test beams taken from the available published literature.

Abdelrahman (1997) tested prestressed and partially prestressed concrete beams with CFRP bars to study their flexural behavior. Eight beams were prestressed with CFRP bars and two with conventional steel bars. The beams were tested using quasi-static monotonic concentrated loads. The research studied the serviceability limit states in terms of crack width, crack spacing, and deflection prior to and after cracking. The modes of failure and the ultimate carrying capacity of the beams were also investigated. The tested beams were analyzed using a strain compatibility approach to predict the moment-curvature relationship. The deflection was calculated using two different techniques, integration of the curvature at many sections along the beam span, and a simplified method where the deflection was calculated using an equivalent moment of inertia for the entire beam. The proposed models had less than a 20 percent margin of error compared to the experimental results. The tested beams pretensioned by CFRP exhibited considerable warning before failure due to the presence of extensively distributed cracks and large deflection prior to failure. A change of the reinforcement ratio resulted in a change in failure mode and deformability. Partial prestressing increased the deformability of the beams. New parameters were proposed based on experimental and analytical results to accurately predict the deflection, prior to and after cracking, and crack width. Recommendations for flexural design and the deflection and crack width computation of beams partially prestressed with CFRP bar were introduced.

Lu (1998) performed flexural tests on beams prestressed with three types of FRP bars including two kinds of CFRP bars and one kind of AFRP bar. The primary variable in the study was the type of FRP materials. The flexural test was a four-point bending test to evaluate the moment-curvature and load-deflection behavior of the specimens. Two methods were used to determine curvature. The first method was to attach linear variable differential transducers (LVDTs) on one side of the beam to directly measure concrete strains. The second method was to measure beam deflection at five different locations along the beam within the constant moment zone using potentiometers. The deflection curve formed by the five points should be a part of the circle, and the radius of the circle should be equal to the inverse of the curvature in the constant moment zone. Both bond slip failure and flexural failure occurred. Beams with AFRP bars exhibited larger deflection, curvature, and more cracks at failure than the beams with CFRP bars, but the CFRP prestressed beams had greater moment capacity. The FRP prestressed beams had smaller incremental crack width openings than those reinforced with steel strands, indicating a stronger bond mechanism between concrete and the FRP bars.

The performance of concrete beams prestressed with AFRP bars has been investigated by Toutanji and Saafi (2000). The results of their experiments show that ductility can be significantly enhanced by using a combination of bonded and unbonded bars or by the addition of non-tensioned rebar. Dolan et al. (2001) proposed detailed equations to determine the capacity of vertically aligned bars, which is also valid for harped prestressing. The authors found the difference in estimating capacity using both the proposed formula and the simplified equation for bars in a single layer within 1 percent. For the application of aramid bars in high-strength concrete, Rashid et al. (2005) conducted some experimental tests and investigated the behavior of 10 AFRP-reinforced high-strength concrete beams under three-point loading. Their test results showed that a concrete beam, when reinforced with AFRP bars, becomes more flexible in the post-cracking range than an equivalent steel-reinforced beam and may fail in an unusual flexure-shear mode.

The research clearly shows that the structural behavior of a full-scale FRP concrete bridge girder in composite action with the topping deck, where the realistic dimensions, boundary conditions, and structural details are all physically modeled, has not been well studied. Conducting a full-scale test with realistic details, where the effect of the bridge deck has been

accounted, is crucial because it substantially impacts the structural capacity and failure mode of the bridge girder. Moreover, only under such circumstances are the experimental and analytical results reliable. Design guidelines can be established based on these results, and the overall system can be recommended for practical use.

1.6 Organization of the Report

This report includes six main chapters. The introduction to this research investigation is given in Chapter 1. Chapter 2 presents the experimental program including design and analysis of the specimen, structural details, and testing plan. Chapter 3 discusses the material properties of self-consolidating concrete and AFRP bars based on the experimental tests conducted by the authors. Chapter 4 illustrates the newly developed anchorage system for prestressing operations and portrays the state of the art and state of the practice on this topic. Chapter 5 presents the construction process along with discussion of advantages and difficulties. Chapter 6 presents the experimental results, verifications with numerical analyses, and comparison with the control specimen. Chapter 7 summarizes the conclusions and recommendations.

2 EXPERIMENTAL PROGRAM

2.1 Introduction

The experimental program of this research was basically divided into two different tests, flexure and shear. The first test plan was the flexure test, where a large region at the middle of the girder was cracked and damaged to some extent. The second test plan was the shear tests, which was conducted on the two uncracked ends of the girder close to the supports. These flexure and shear tests were both conducted at the High Bay Structural and Materials Testing Laboratory on the campus of Texas A&M University.

A flexure test was conducted to determine the load and curvature capacities of the specimen. The flexure test was set up as a four-point bending test in order to create a region of constant maximum moment in the center of the specimen. The main factors that were studied in the flexure test included flexure load, curvature capacities, failure mode, cracking pattern, strain distribution over the height of the section, deflection profile, and moment-curvature relationship. The flexure load was determined by monitoring the pressure from the 2700-kN (600-kips) actuator used to load the specimen. Concrete strain gages were attached to the top of the deck to determine the failure mode of the specimen. Conventional steel-reinforced concrete sections typically fail when the top fiber reaches 3000 micro-strain; however, an AFRP-reinforced section typically fails due to rupture of the AFRP bars in the bottom flange. LVDTs were attached to the top and bottom flanges of the specimen to investigate the strain distribution over the height of the section, along with the crack widths. String potentiometers were attached to the bottom of the specimen to monitor the deflection profile, curvature capacity, and moment-curvature relationship. A data acquisition (DAQ) system collected data every 5 seconds to determine the following characteristics:

- Moment-curvature relationship (load-displacement relationship).
- Initial stiffness.
- Bond performance prior to cracking.
- Bond performance after cracking.
- Crack patterns.

After the flexure test was completed, both ends of the specimen were tested in shear to determine the shear capacity, failure mode, and maximum strain in the web of the specimen. The specimen was moved via a 178-kN (40-kips) overhead crane in the High Bay Structural and Materials Testing Laboratory, and the supports were adjusted to create the proper clear span. The non-testing end was raised using the overhead crane to ensure that it did not affect the results. A load cell was attached to the overhead crane, and the load was held constant to ensure consistent testing. The placement of the load point varied to determine the transition point from flexure to shear failure along the length of the specimen. The main factors that were studied in the shear test included shear capacity and failure mode, and maximum strain in the web. Concrete strain gages were attached to the top of the deck to determine the failure mode of the specimen. The shear capacity was investigated by monitoring the load applied to the specimen via the pressure from the 2700-kN (600-kips) actuator. LVDTs were attached in a crossing pattern in the center of the web to determine the maximum strain in the web. The cracking patterns and crack width were also monitored. A DAQ system collected data every 5 seconds to determine the following characteristics:

- Moment-curvature relationship.
- Bond characteristics of the development length region.
- Shear performance.
- Crack patterns.

2.2 Bridge Girder Design

2.2.1 Bridge Prototype

The girder design was based on the bridge prototype shown in Figure 2-1, including the prestressed precast AASHTO I-girder Type I and a cast-in-place topping deck. As shown, simply supported girders were spaced 1.8 m (6 ft.) on the center and 12.2 m (40 ft.) on the span. The girder was designed based on the AASHTO *LRFD Bridge Design Specifications* (2010) to meet the service and ultimate limit states. The modulus of elasticity of AFRP bars is considerably less than that of steel, about one-third, so once the section is cracked, there is a substantial decline in the flexural stiffness of the girder, leading to a larger deflection. Therefore, for the sake of controlling the deflection and satisfying the serviceability criteria, the bridge

girder was designed as a fully prestressed beam. As opposed to reinforced concrete, the prestressed concrete beams and slabs are commonly designed for serviceability limit states and then checked for the ultimate (strength) limit state.

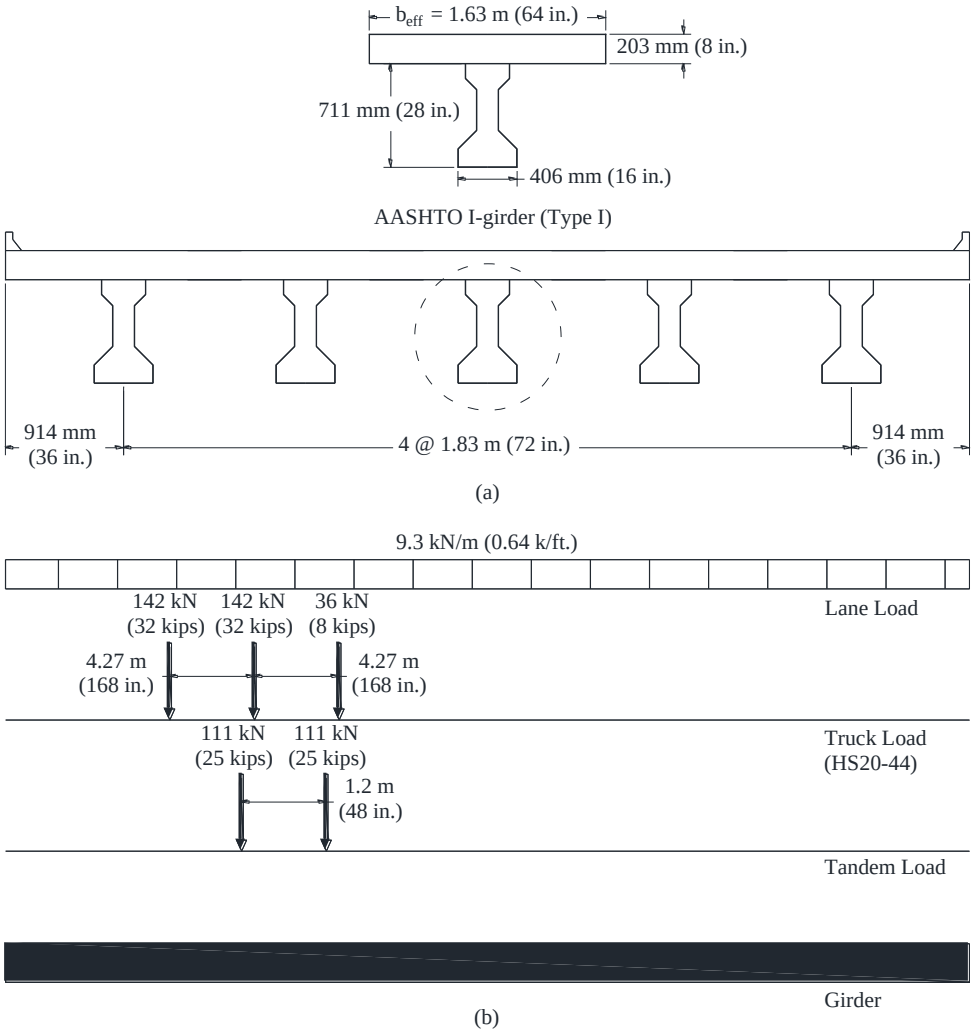

Figure 2-1. Bridge Prototype: (a) Geometry and (b) Design Vehicle Load Cases.

Table 2-1 shows the section characteristics for the AASHTO I-girder Type I either alone or with the topping deck. The effective width of the topping deck was selected as the minimum of the three following values according to the AASHTO *LRFD Bridge Design Specifications* (2010):

$$B_w + 12h_f = 1371.6 \text{ mm (54 in.)}$$

$$B_w + L_c = 1981.2 \text{ mm (78 in.)}$$

$L/4$ = 3657.6 mm (144 in.)

where B_w and h_f are respectively the width and thickness of the top flange of the girder, L_c is the slab span between the girders, and L is the girder length. The minimum is equal to 1.37 m (54 in.); however, the width of the topping deck was selected as 1.62 m (64 in.) to be the same as that of the controlling specimen (Trejo et al. 2008).

Table 2-1. Section Properties of the Girder.

Section	A mm^2 (in.^{2})	Y_b mm (in.)	Y^t mm (in.)	I mm^4 (in.^{4})	S_b mm^3 (in.^{3})	S^t mm^3 (in.^{3})
Girder	17.81×10^4 (276)	319.78 (12.59)	391.41 (15.41)	9.47×10^9 (22,750)	29.61×10^6 (1807)	24.19×10^6 (1476)
Girder & Deck	50.83×10^4 (788)	640.08 (25.2)	274.32 (10.8)	38.73×10^9 (93,043)	60.5×10^6 (3692.18)	141.17×10^6 (8615.1)
A	cross-sectional area					
Y_b	distance from neutral axis to the bottom flange					
Y^t	distance from neutral axis to the top flange					
I	moment of inertia					
S_b	section modulus with respect to the bottom fiber of the section					
S^t	section modulus with respect to the top fiber of the section					

2.2.2 Flexural Design Based on Serviceability Limit States

The maximum dead load moments induced by each component of the bridge prototype are summarized in Table 2-2 including the dead load of the girder, slab, barrier, and future wearing. Maximum live load moments, per lane, due to the truck load and lane load are calculated as $M_{L\text{-}Truck}$ = 623 kNm (450 kft.) and $M_{L\text{-}Lane}$ = 177 kNm (128 kft.). For the girder shown in Figure 2-1, tandem load results in almost the same maximum moment as the truck load.

Table 2-2. Maximum Dead Load Moments (kNm [kft.]).

$M_{D\text{-}Beam}$	$M_{D\text{-}Slab}$	$M_{D\text{-}Barrier}$	$M_{D\text{-}Wearing}$
76(55)	152(110)	33(24)	36(26)
$\sum$ = 228(165)		$\sum$ = 69(50)	
M_D = 297(215)			

The distribution factor for moment is computed as DFM = 0.56 based on AASHTO *LRFD Bridge Design Specifications* 4.6.2.2.2b-1 (2010). Assuming the impact factor of *IM* = 1.33, the maximum live load moment can be computed from the following equation:

$$M_L = DFM\left(M_{L-Truck} \times IM + M_{L-Lane}\right) \tag{2-1}$$

which gives M_L = 550 kNm (405 kft.). According to AASHTO 3.4, the service load for deflection control (D+L) is M_s = 841 kNm (620 kft.), and the ultimate load for strength design (1.25D+1.75L) is M_u = 1326 kNm (978 kft.). To compute the required number of AFRP tendons, the service load for controlling the tension in prestressed concrete (D+0.8L) is considered as follows:

$$f_b = \left(\frac{M_{D-Beam} + M_{D-Slab}}{S_b}\right) + \left(\frac{M_{D-Barrier} + M_{D-Wearing} + 0.8\left(M_{L-Truck} + M_{L-Lane}\right)}{S_{bc}}\right) \tag{2-2}$$

Given that the section modulus for the bottom fiber of the girder and the composite section are S_b = 29.61×10^6 mm^3 (1807 in.^{3}) and S_{bc} = 60.5×10^6 mm^3 (3692.18 in.^{3}), respectively, the tensile normal stress at the bottom fiber of the section is computed as f_b = 16.56 MPa (2.4 ksi). Based on AASHTO 5.9.4.2.2-1, the allowable tensile stress is $f_t = 0.5\sqrt{f_c'} = 4.64$ MPa (0.67 ksi). The compressive strength of the self-consolidating high-strength concrete was deemed to be 86.2 MPa (12.5 ksi), which will be discussed in Chapter 3. Based on these calculations, the compressive stress required by prestressing must be equal to f_{bp} = 16.56 − 4.64≈12 MPa (1.74 ksi). This compressive stress can be written as:

$$f_{bp} = \frac{P}{A} + \frac{Pe}{S_b} \tag{2-3}$$

where the cross-sectional area of the girder is A = 17.81×10^4 (276 in.^{2}). As shown in Figure 2-2, the prestressing eccentricity is e = 190 mm (7.5 in.), which gives the required prestressing force to be equal to P = 990 kN (223 kips). As will be discussed, AFRP bars are prestressed up to 50 percent of their ultimate strength, and it can be rationally assumed that the total loss during the lifetime of the structure is 15 percent. Thus, the required number of AFRP tendons in the bottom flange is:

$$N = \frac{990 \times 10^3}{78.5 \times 1393 \times 0.5 \times (1 - 0.15)} \approx 22 \tag{2-4}$$

where the cross-sectional area and strength of each AFRP bar are respectively equal to 78.5 mm^2 (0.122 in.^{2}) and 1393 MPa (202 ksi). The tensile stress at the top flange of the girder and close to the support, where there is no positive moment, needs to be controlled at transfer (before prestressing loss) to meet the serviceability criteria. Therefore, two more prestressed AFRP tendons are used at the top flange. The normal tensile stress at the top fiber can be calculated as:

$$f^T = \left(-\frac{22+2}{A} + \frac{22 \times e}{S^T} - \frac{2 \times e'}{S^T} \right) \times 78.5 \times 1393 \times 0.5 \tag{2-5}$$

where positive and negative signs indicate tension and compression, respectively. Substituting the section modulus for the top fiber of the girder, S^T = 24.19×10^6 mm^3 (1476 in.^{3}), gives $f^T = 0.55$ MPa (0.08 ksi), which is less than the allowable tension at transfer, $f_{ti} = 0.63\sqrt{f_{ci}'} = 5.85$ MPa (0.85 ksi) based on AASHTO 5.9.4.1.2-1.

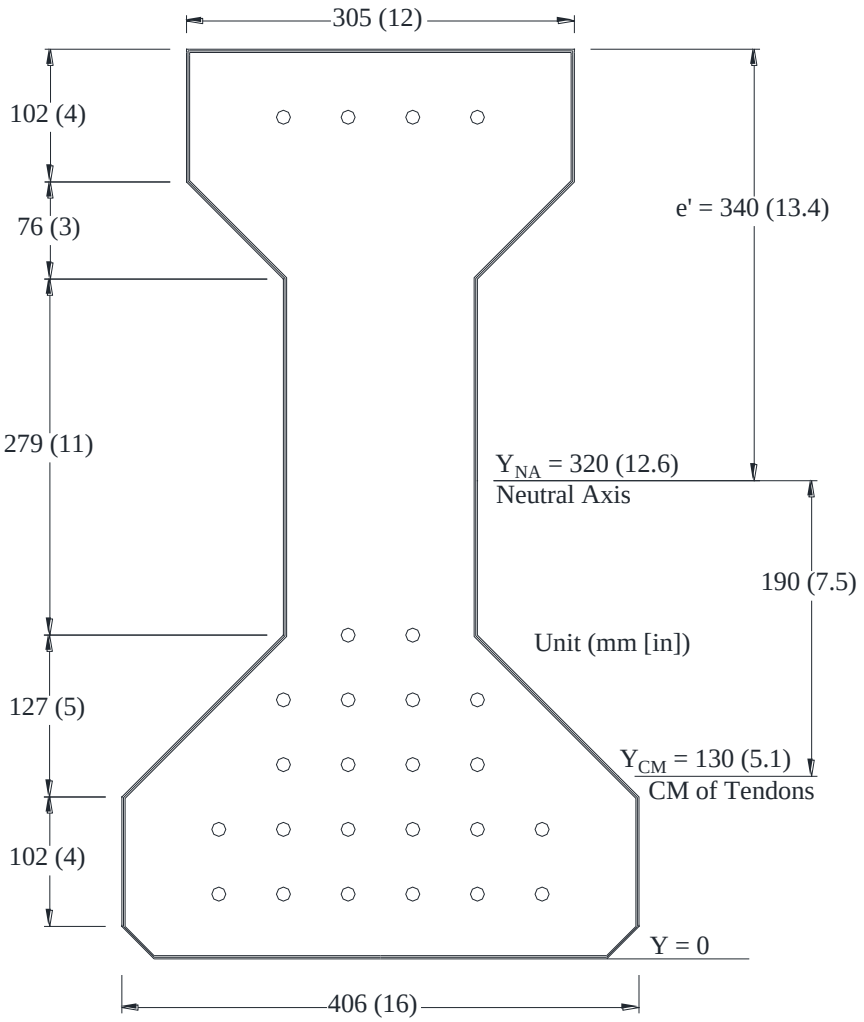

Figure 2-2. Dimensions, Neutral Axis Location, and Center of Mass of Tendons for AFRP Prestressed Girder.

2.2.3 Flexural Design Check for Ultimate Limit State

As discussed, the bridge girder was first designed for the serviceability limit state and then checked for the ultimate (strength) limit state. Based on the AASHTO LRFD load cases, the ultimate load for strength design (1.25D+1.75L) is equal to M_u = 1326 kNm (978 kft.). Assuming the plane section remains plane after bending, and using the basic equilibrium and compatibility equations, the flexural strength of the composite girder was calculated. Before calculating the flexural strength, the failure mode of the girder, whether tendon failure or concrete crushing, needed to be specified by the balanced ratio concept. The condition where the tendon ruptures simultaneously with the concrete compression failure is called the balanced condition (ACI 440.4R 2004), and the corresponding reinforcement ratio is called the balanced ratio (ρ_b). If the

reinforcement ratio of the section is less than ρ_b—the under-reinforced section—the failure mode is due to tendon rupture; otherwise, the girder fails due to concrete compression failure. As illustrated in Figure 2-2, the location of the neutral axis (c/d) under the balanced condition can be determined from the compatibility equations:

$$\frac{c}{d} = \frac{\varepsilon_{cu}}{\varepsilon_{cu} + \varepsilon_{pu} - \varepsilon_{pe}} \tag{2-6}$$

where ε_{cu}, ε_{pu}, and ε_{pe} respectively represent the failure compressive strain of the concrete, the strain capacity of the AFRP bars, and the strain used by prestressing the AFRP bars. In fact, $\varepsilon_{pu} - \varepsilon_{pe}$ indicates the strain of AFRP bars left for flexure. Using ε_{cu} = 0.003, ε_{pu} = 0.02, ε_{pe} = 0.008, and d = 863.6 mm (34 in.) gives the neutral axis location equal to c = 30.73 mm (1.21 in.); this implies that the neutral axis is within the topping deck. The balanced ratio (ρ_b) can be determined through the equilibrium equation, which balances the tensile force of the tendons with the compressive force on the concrete:

$$0.85 f_c' \beta_1 cb = \rho_b b d f_{pu} \tag{2-7}$$

where β_1 = 0.85 for concrete strengths up to 27.5 MPa (4 ksi), and for greater strength values it is reduced at a rate of 0.05 for each 6.9 MPa (1 ksi) to a minimum value of 0.65; and f_{pu} is the ultimate strength of the AFRP bars. Solving the equation gives the balanced ratio equal to ρ_b = 0.008. The reinforcement ratio of the girder is equal to ρ_b = 0.0012, which is about 18 percent of the balanced ratio, and hence the failure mode of the girder is governed by tendon rupture. Based on this failure mode, the flexural capacity for vertically distributed tendons in an under-reinforced section can be determined according to ACI 440. 4R (2004) equations 3-18, 3-19, and 3-20:

$$f_i = f_{pe} + f_m \left(\frac{\frac{d_i}{d} - \frac{c}{d}}{1 - \frac{c}{d}} \right) \tag{2-8}$$

where d_i is the depth of each individual tendon, d is the depth of the bottom tendon, f_{pe} is the tendon stress due to pre-tensioning, and f_m is the tendon stress due to flexure. If the initial prestressing ratio is defined as ξ = (f_{pe}/ f_{pu}), the neutral axis location is $c = kd$, and the

reinforcement ratio at level i is $\rho_i = (A_{pi} / bd)$; then the following equation gives the neutral axis location:

$$k = \frac{\sqrt{\left(n\sum_{i=1}^{m}\rho_i\right)^2 + 2(1-\xi)n\sum_{i=1}^{m}\rho_i\left(\xi + \frac{d_i}{d}(1-\xi)\right)} - n\sum_{i=1}^{m}\rho_i}{1-\xi} \tag{2-9}$$

where m is the number of layers of tendons. If the depth ratio of the tendons is defined as $\varphi_i = (d_i/d)$, then the flexural capacity can be expressed as:

$$M_n = bd^2\sum_{i=1}^{m}\rho_i f_i\left(\psi_i - \frac{\beta_1 c}{2d}\right) \tag{2-10}$$

The prestressing ratio is deemed to be constant over the different layers of AFRP tendons. Using a spreadsheet, the flexural capacity is calculated as M_n = 1762.5 kNm (1300 kft.). This is a conservative calculation because the contribution of non-prestressed AFRP bars within the girder's web, the two prestressed AFRP bars within the top flange of the girder, and the bottom layer of steel reinforcement in the deck is ignored. The theoretical flexural capacity is almost 33 percent greater than the maximum factored AASHTO load of M_u = 1326 kNm (978 kft.). This implies that a strength reduction factor of 0.75 can be applied, which is close to the strength reduction factor of 0.7 suggested by ACI 440.4R (2004) for cases where the failure mode is governed by a tension-controlled behavior such as tendon rupture.

2.2.4 Shear Design

The shear design of the girder was performed based on AASHTO *LRFD Bridge Design Specifications* (2010) section 5.8.2 through 5.8.4 and ACI 440.4R (2004) section 5-2. The following strength load combination was used to calculate the ultimate shear force:

$$V_u = 1.25(V_D + V_S + V_B) + 1.5(V_W) + 1.75(V_{LL} + V_{LT}) \tag{2-11}$$

where V_D, V_S, V_B, and V_W respectively represent the shear due to uniformly distributed dead load of the beam (W_D = 4.2 kN/m [0.287 k/ft.]), dead load of the slab (W_S = 8.8 kN/m [0.6 k/ft.]), barrier load (W_B = 1.8 kN/m [0.12 k/ft.]), and future wearing load (W_W = 2.0 kN/m [0.135 k/ft.]). V_{LL} and V_{LT} denote the shear due to lane load and truck load, which can be readily calculated as shown on Figure 2-1. The shear is calculated at a distance d away from the support. If the shear

components are substituted in Equation (2-11), the ultimate shear load equals V_u = 566.12 kN (127.275 kips). The shear strength of the concrete (V_C) can be found in kN as follows:

$$V_C = \left(0.166\sqrt{f'_C}\right) b_w d_w \tag{2-12}$$

where the shear stress capacity is $v_C = 0.166\sqrt{f'_C}$ = 1.54 MPa (0.233 ksi), the girder's web thickness is b_w = 152.4 mm (6 in.), and the effective depth is d_w = 863.6 mm (34 in.). Therefore, the shear strength is evaluated as V_C = 140.62 kN (31.61 kips). To satisfy the shear design criteria, the shear resistance by AFRP stirrups (V_S) can be found as:

$$V_u = \phi(V_c + V_s) \tag{2-13}$$

where the strength reduction factor is equal to $\phi = 0.9$ per AASHTO 5.5.4.2. This gives *Vs* = 488.4 kN (109.8 kips). The distance between stirrups (*S*) can be calculated as:

$$V_S = A_v f_v (d / S) \cot\theta \tag{2-14}$$

where θ is the shear crack inclination angle, A_v is the area of the stirrup's legs equal to 2×78.5 = 157 mm^2 (0.243 in.^{2}) , and f_v = min (0.3 f_{pu}, 0.002*E*) per ACI 440.4R (2004) section 5-2. As already shown, for AFRP bars f_{pu} = 1393 MPa (202 ksi) and *E* = 68,950 MPa (10,000 ksi), which results in f_v = 137.9 MPa (20 ksi). The inclination of shear cracks close to the support is equal to θ = 25° based on the modified compression field theory (MCFT) as discussed in AASHTO *LRFD Bridge Design Specifications* sections 5.8.2–5.8.3. Substituting these values into Equation (2-14) gives the distance between stirrups approximately equal to *S* = 101.6 mm (4 in.). The stirrup spacing is less than the maximum limit of $d_w/2$ = 431.8 mm (17 in.) or 600 mm (24 in.) stipulated by ACI 440.4R (2004) section 5.3. The stirrup distance is doubled to 203.2 mm (8 in.) at 1371.6 mm (54 in.) away from the end supports. The minimum amount of shear reinforcement ($A_{v,min}$) can be checked through ACI 440.4R Equation 5-6, which gives $A_{v,min}$ = 64.5 mm^2 (0.1 in.^{2}) < A_v = 157 mm^2 (0.234 in.^{2}):

$$A_{v,\min} = \frac{1}{16}\sqrt{f'_c}\,\frac{b_w S}{f_v} \quad (\text{mm}^2) \tag{2-15}$$

Other than the shear capacity of the girder close to the end supports, the girder-to-slab interface shear capacity needs to be checked as well. A similar load combination as stated in

Equation (2-11) can be written for the interface shear excluding the dead load of the slab and girder:

$$V_u = 1.25(V_B) + 1.5(V_W) + 1.75(V_{LL} + V_{LT}) \quad (2\text{-}16)$$

which gives the ultimate shear equal to V_u = 475.9 kN (107 kips). In a conservative assumption, the maximum shear stress at a neutral axis (which is close to the girder-to-slab interface) is found. Given the first moment of area of the girder's section with respect to the neutral axis $Q_{N.A}$ = 57.82×10^6 mm^3 (3528.64 in.^{3}) and the second moment of inertia I = 38.73×10^9 mm^4 (93043 in.^{4}), the maximum shear stress equals $\tau = V_u Q_{N.A} / It$ = 2.33 MPa (0.337 ksi), where t is the top flange equal to 304.8 mm (12 in.). This implies that at every 304.8 mm (12 in.), the maximum horizontal shear force at the girder-to-slab interface is equal to V_h = 215.85 kN (48.528 kips). Considering high-strength A490 bolts with a 25.4-mm (1-in.) diameter, which has 157-kN (35.3-kft.) allowable shear stress, results in using the shear bolts at approximately every 304.8 mm (12 in.).

2.3 The Experimental Specimen

The cross section of the AASHTO I-girder Type I was composed of self-consolidating concrete reinforced and prestressed with AFRP bars having a 10-mm (0.393-in.) diameter. The dimensions and reinforcement layout are shown in Figure 2-3. Twenty-four prestressed AFRP bars were used within the girder section: 22 in the bottom flange and two in the top flange. In addition to prestressed AFRP bars, eight non-prestressed AFRP bars were used within the girder section: six in the web and two in the top flange. The shear reinforcement dimensions and layout for the R-shape, top, and bottom stirrups are also presented in Figure 2-3 and Figure 2-4. R-shape stirrups were spaced 203 mm (8 in.) apart along the girder except at the support region, where the stirrup spacing was reduced to 102 mm (4 in.) to better resist the diagonal shear. The top and bottom stirrups were placed only at the support region and spaced 102 mm (4 in.) apart, similar to the manner for R-shape stirrups. In addition to AFRP shear reinforcement, steel shear bolts were added at the deck/girder interface to help make a better transfer of horizontal shear through the deck/girder composite action. The shear bolts were spaced 457 mm (18 in.) apart along the girder.

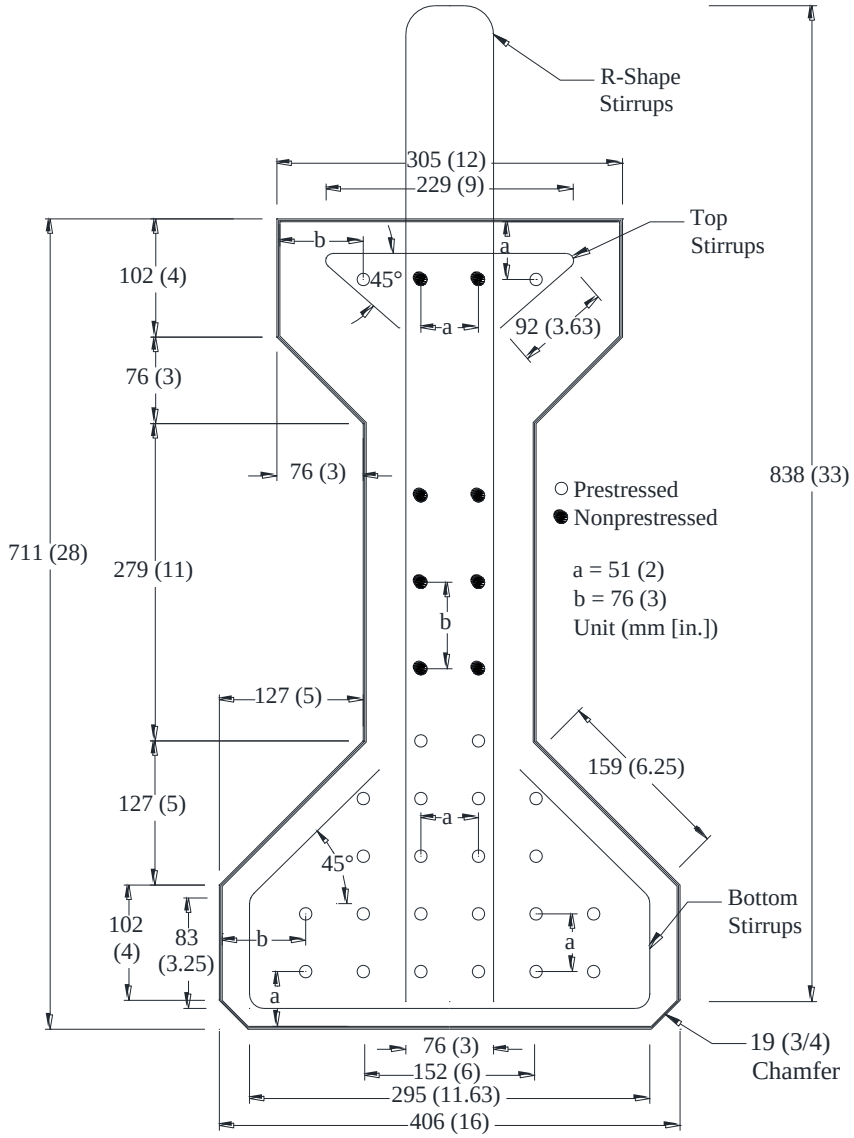

Figure 2-3. AASHTO I-Girder Type I with Composite Topping Deck Dimensions and Reinforcement.

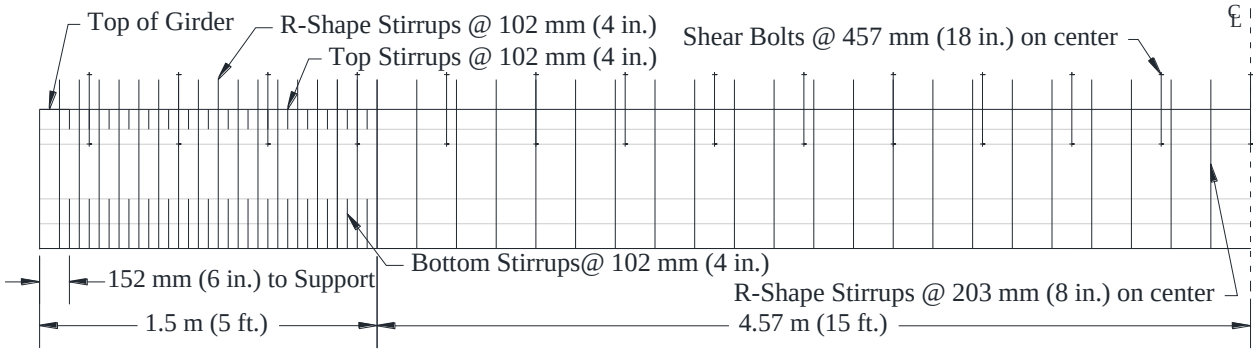

Figure 2-4. Shear Reinforcement Layout of the Girder.

The reinforcement for the topping deck consisted of conventional steel rebar to reinforce the slab either longitudinally or transversely. AFRP reinforcement was not used in the topping deck because the deck was modeled only to provide composite action with the girder. The reinforcement layout for the topping deck is shown in Figure 2-5. The longitudinal reinforcement was composed of two D16 (#5) rebar bisecting the center, six D13 (#4) rebar spaced at 203 mm (8 in.) apart in the bottom, and nine D13 (#4) rebar spaced at 178 mm (7 in.) at the center on the top. The transverse reinforcement was composed of D13 (#4) rebar placed 203 mm (8 in.) apart on the top and bottom.

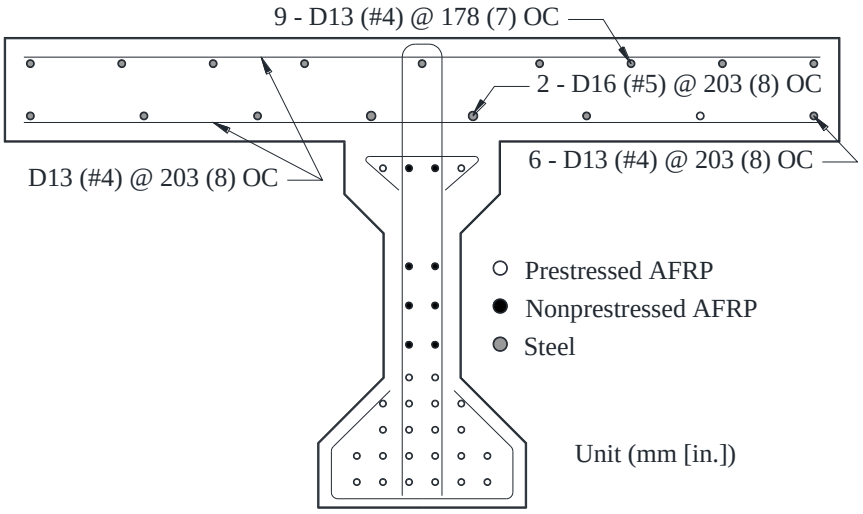

Figure 2-5. Deck Reinforcement Detail.

2.4 Flexure Test Setup

The flexure test setup is shown in Figure 2-6, Figure 2-7, and Figure 2-8. Steel frames were anchored to the strong floor at the High Bay Structural and Materials Testing Laboratory using post-tensioned dywidag threaded rods. A 2700-kN (600-kips) actuator was attached to the steel frame and used to load the specimen. A steel W-shape was positioned under the load point and supported by two 914×203-mm (36×8-in.) rocker supports placed 915 mm (36 in.) apart to distribute the load evenly throughout the composite topping deck. Rocker supports with 203×203×76-mm (8×8×3-in.) Neoprene bearing pads supported the girder. The bearing pads were positioned to create an 11.8-m (39-ft.) clear span. The specimen was manually loaded under displacement control at a rate approximately equal to 44 kN (10 kips) per minute before first cracking at the midspan, and then the rate was decreased to 22 kN (5 kips) per minute after cracking. The load was halted periodically to record and mark crack locations and width.

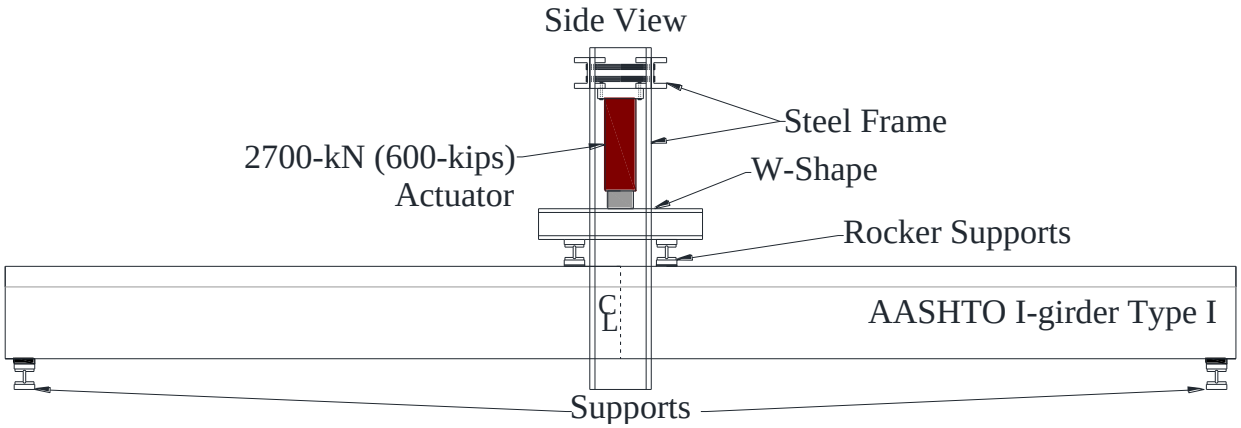

Figure 2-6. Side View of Flexure Test Setup.

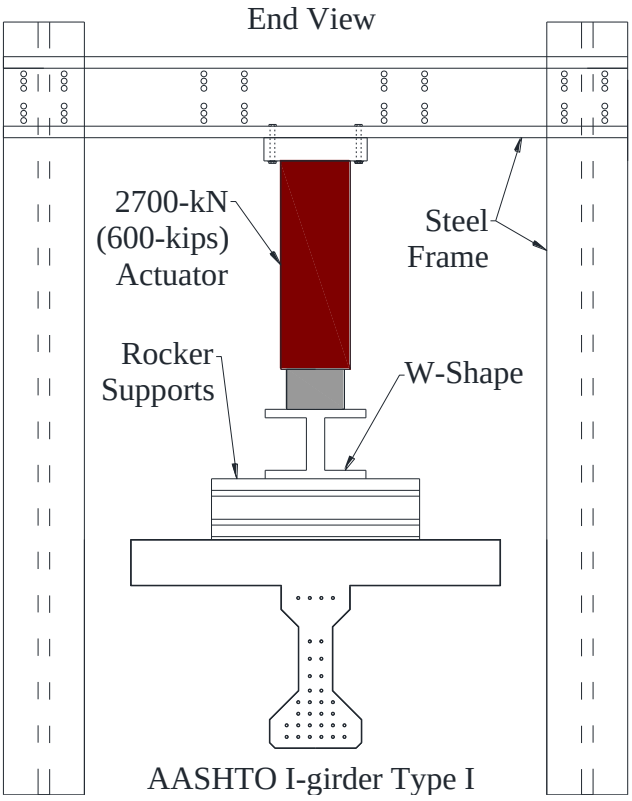

Figure 2-7. End View of Flexure Test Setup.

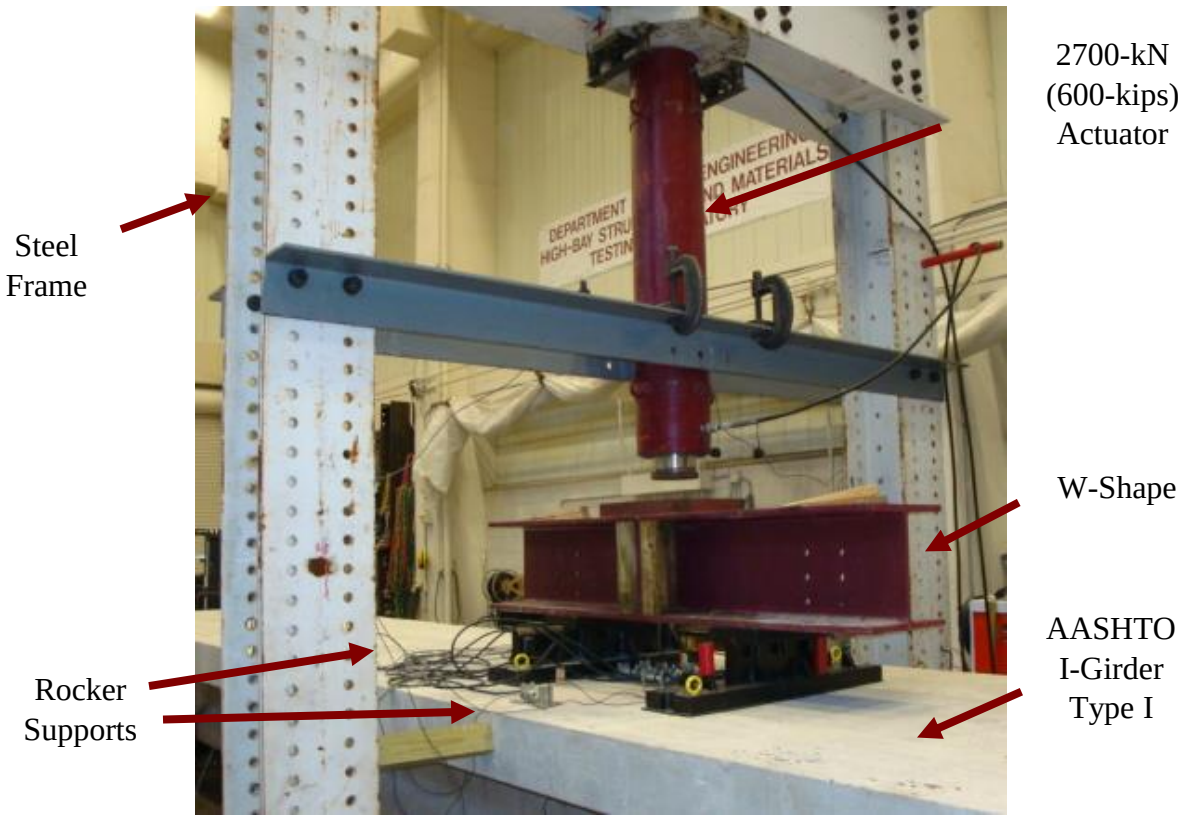

Figure 2-8. Flexure Test Setup.

2.5 Instrumentation for Flexure Test

Concrete strain gages and LVDTs were placed on the top of the deck to measure the strain at the top fiber of the concrete. The top of the deck was sanded with a concrete grinder to create a smooth surface for the gages to adhere to. The gages were attached to the deck using a quick-setting epoxy resin. The locations of the concrete strain gages are shown in Figure 2-9.

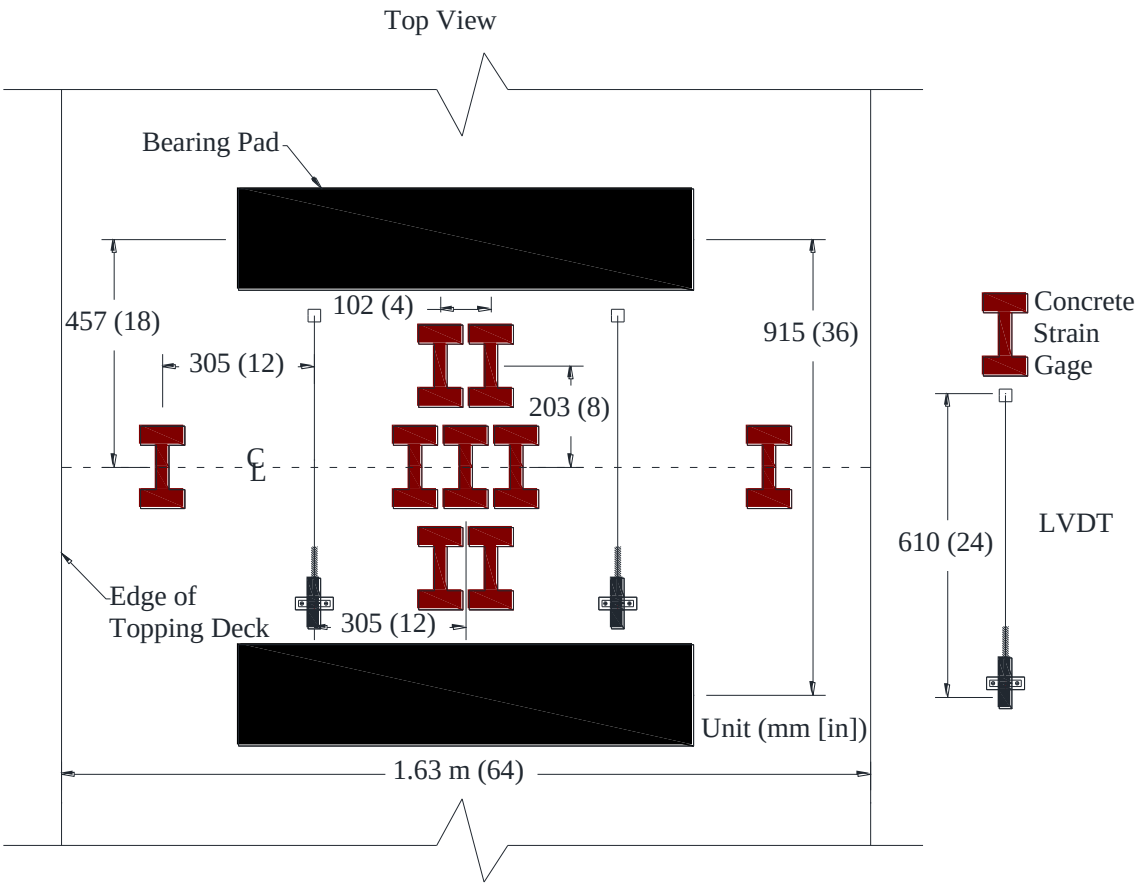

Figure 2-9. Strain Gage and LVDT Layout on Topping Deck at Middle of the Girder (Flexure Test).

Eight LVDTs were attached to measure the strain: five to the bottom and three to the top flange of the girder. The LVDTs were attached by securing the body to a piece of wood epoxied to the girder. Small-diameter threaded rods were attached to the carrier in order to extend the gage length to 610 mm (24 in.) for a better capture of the strains and crack widths. The layout of the LVDTs is presented in Figure 2-10.

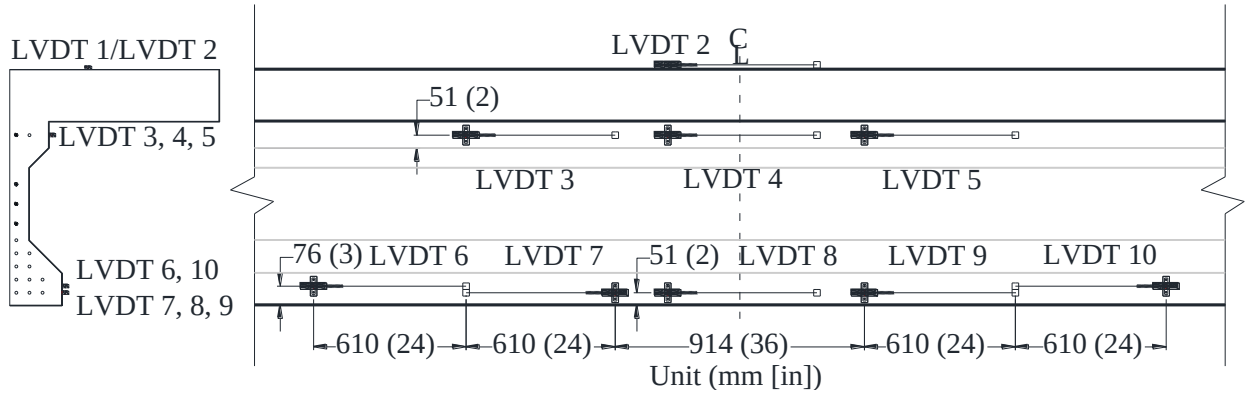

Figure 2-10. LVDT Layout—Flexure Test.

Thirty-one string potentiometers were attached to the bottom of the girder to measure the deflection along the girder. The string potentiometers were secured to a piece of wood that was epoxied to a steel plate in order to overcome the retracting force. A piece of wood with a small metal hook was attached to the bottom of the girder and connected to the measuring cable of the string potentiometer via fishing line. The locations of the string potentiometers are presented in Figure 2-11. The test was terminated when the AFRP in the bottom flange ruptured.

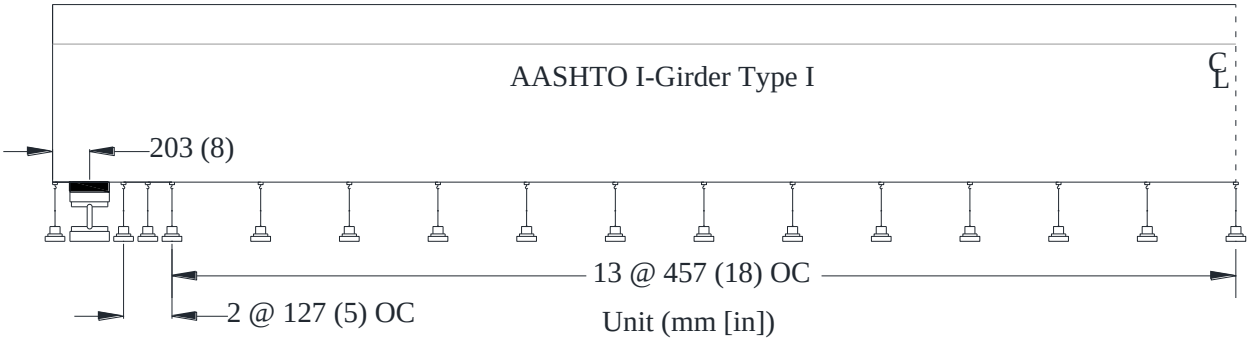

Figure 2-11. String Potentiometer Layout—Flexure Test.

2.6 Shear Test Setup

Following the flexure test, both ends of the girder were tested to determine the shear capacity of the girder. The steel frame and actuator remained stationary while the girder and supports were repositioned for the shear tests. The shear test setup is shown in Figure 2-12, Figure 2-13, and Figure 2-14. The non-testing end was raised using the overhead crane to ensure that it did not affect the results. A load cell was attached to the overhead crane, and the load was held constant to ensure consistent testing. A 914×203-mm (36×8-in.) rocker support was placed under

the actuator to distribute the load evenly throughout the topping deck. Rocker supports with 203×203×76-mm (8×8×3-in.) Neoprene bearing pads were positioned 3.7 m (12 ft.) apart to support the girder. The specimen was manually loaded under displacement control at a rate approximately equal to 22 kN (5 kips) per minute. The load was halted periodically to record and mark crack locations and width. The test was terminated when the AFRP in the bottom flange ruptured.

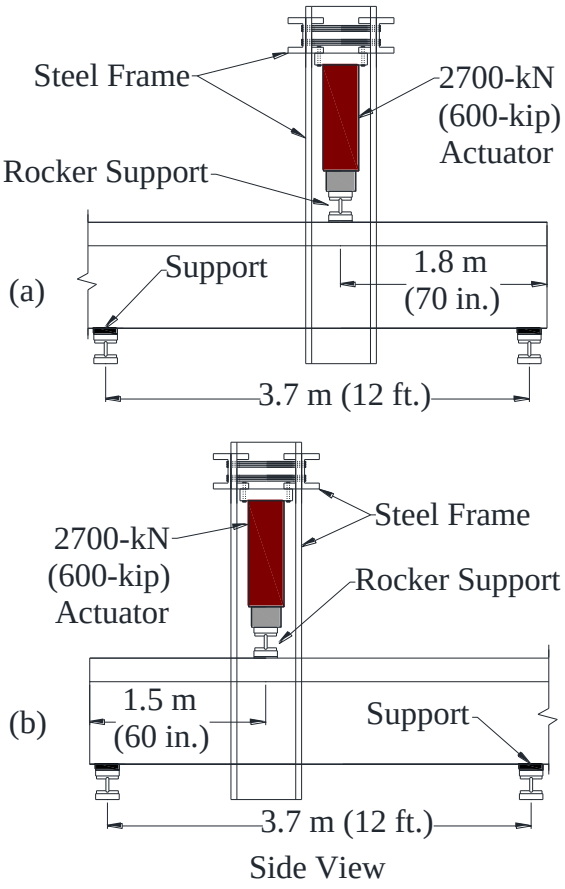

Figure 2-12. Side View of Shear Test Setup: (a) Shear Test 1 and (b) Shear Test 2.

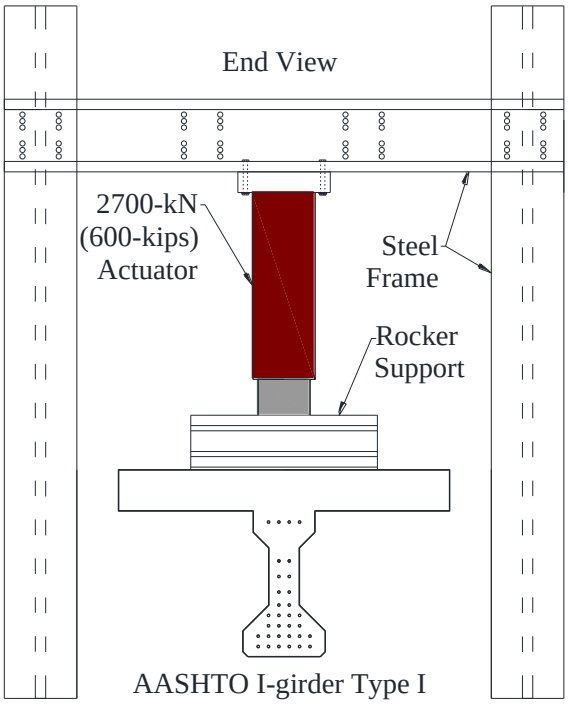

Figure 2-13. End View of Shear Test Setup.

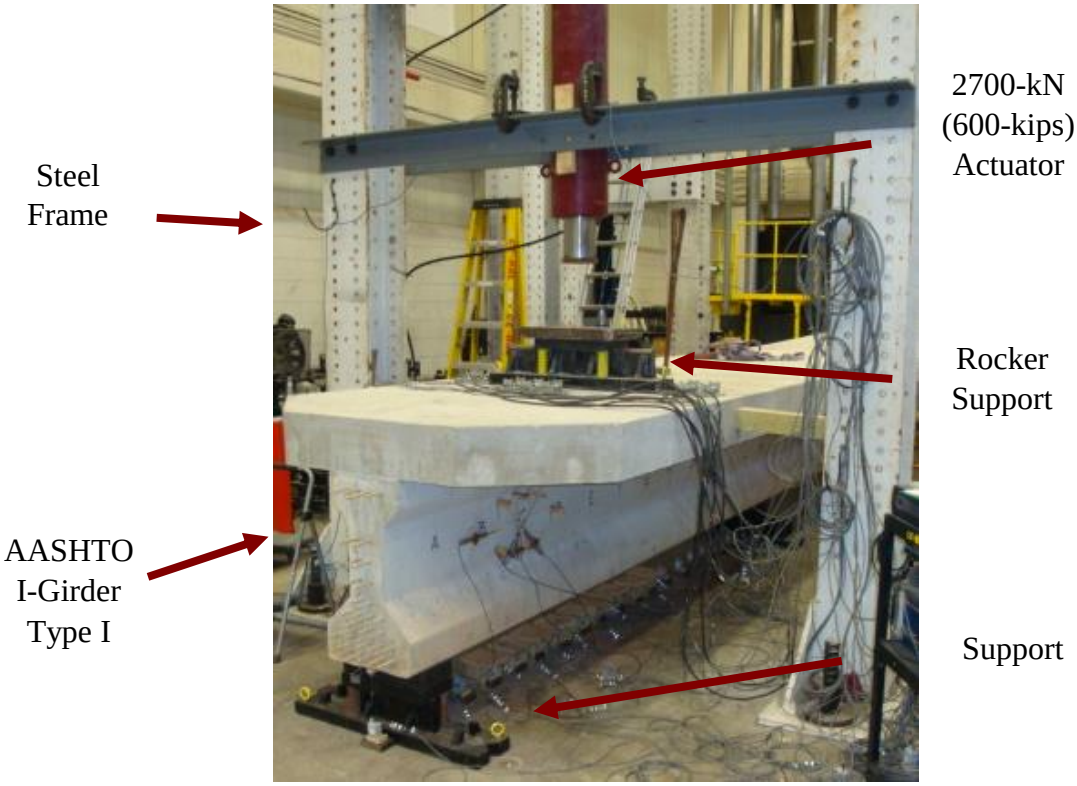

Figure 2-14. Shear Test Setup.

The embedment length and test span were varied between the tests to determine the transition point from flexure to shear failure. In order for the specimen to fail in shear, the embedment length must be shorter than the required development length. The embedment length is defined as the length of the embedded AFRP bars from the end of the girder to the loading point. The embedment lengths for shear test 1 and shear test 2 were 1.8 m (70 in.) and 1.5 m (60 in.), respectively.

2.7 Instrumentation for Shear Tests

Concrete strain gages were attached to the top of the deck to measure the strain in the top fiber of the concrete. The gages were attached in the same manner as described earlier, and the layout is shown in Figure 2-15. The concrete gage layout for the second shear test was identical to the first.

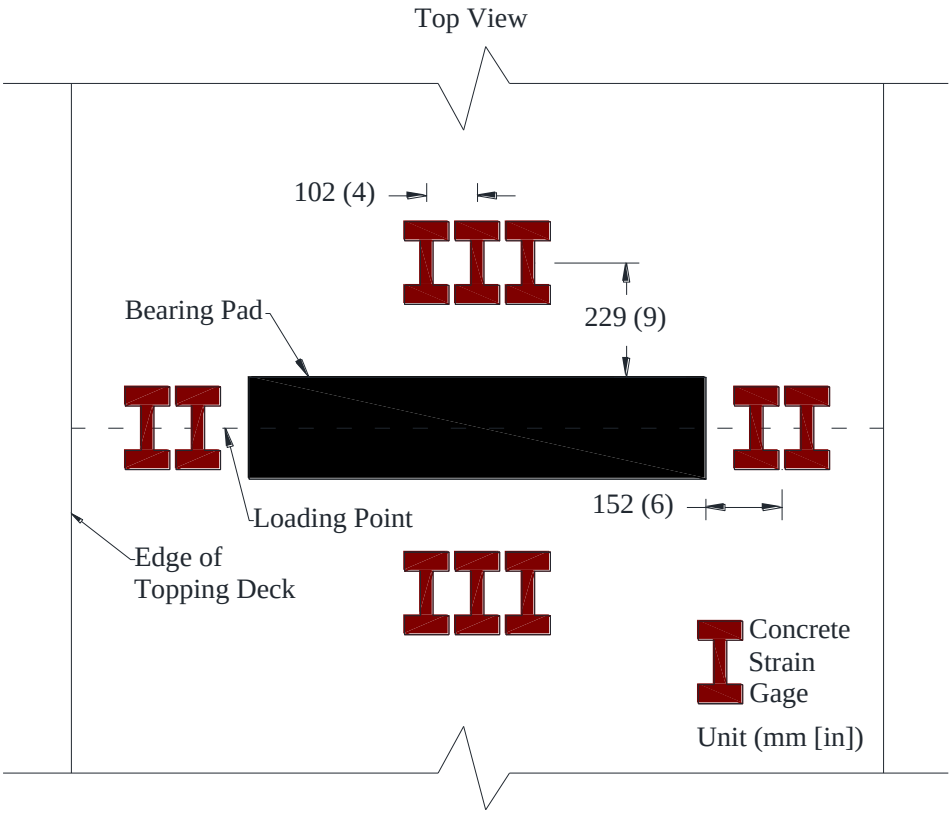

Figure 2-15. Concrete Gage Layout—Shear Test.

Four LVDTs were attached to the web on each side of the girder to measure diagonal tensile and shear strains and stresses. The LVDTs were attached using the same procedure as discussed

previously. The LVDT layout for the shear tests is shown in Figure 2-16. In order to install the LVDTs in the locations presented in Figure 2-16, the bodies of the LVDTs were attached to the girder using pieces of wood of varying thicknesses.

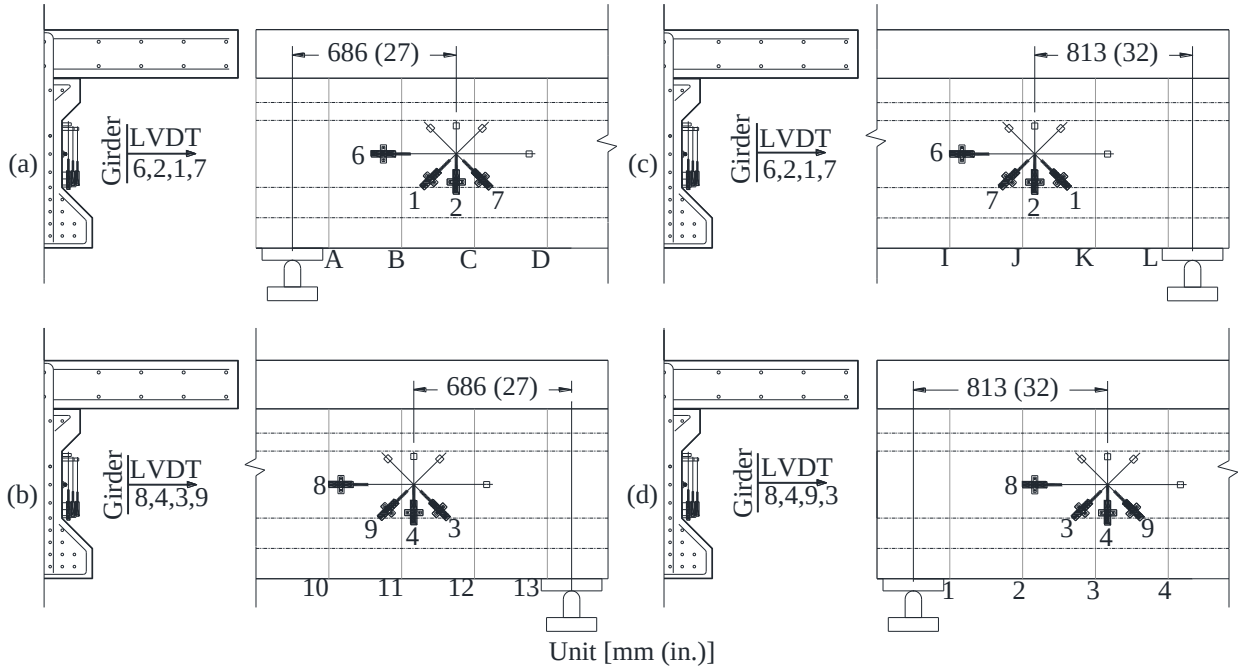

Figure 2-16. LVDT Layout: (a and b) Shear Test 1 and (c and d) Shear Test 2.

String potentiometers were attached to the bottom of the girder, using the same procedure as discussed previously, to measure the deflection of the girder. The string potentiometers were placed directly under the load point, and the remaining potentiometers were spaced 203 mm (8 in.) apart. Additional string potentiometers were placed on either side of the Neoprene bearing pads at the supports. The string potentiometer layout for the shear tests are shown in Figure 2-17.

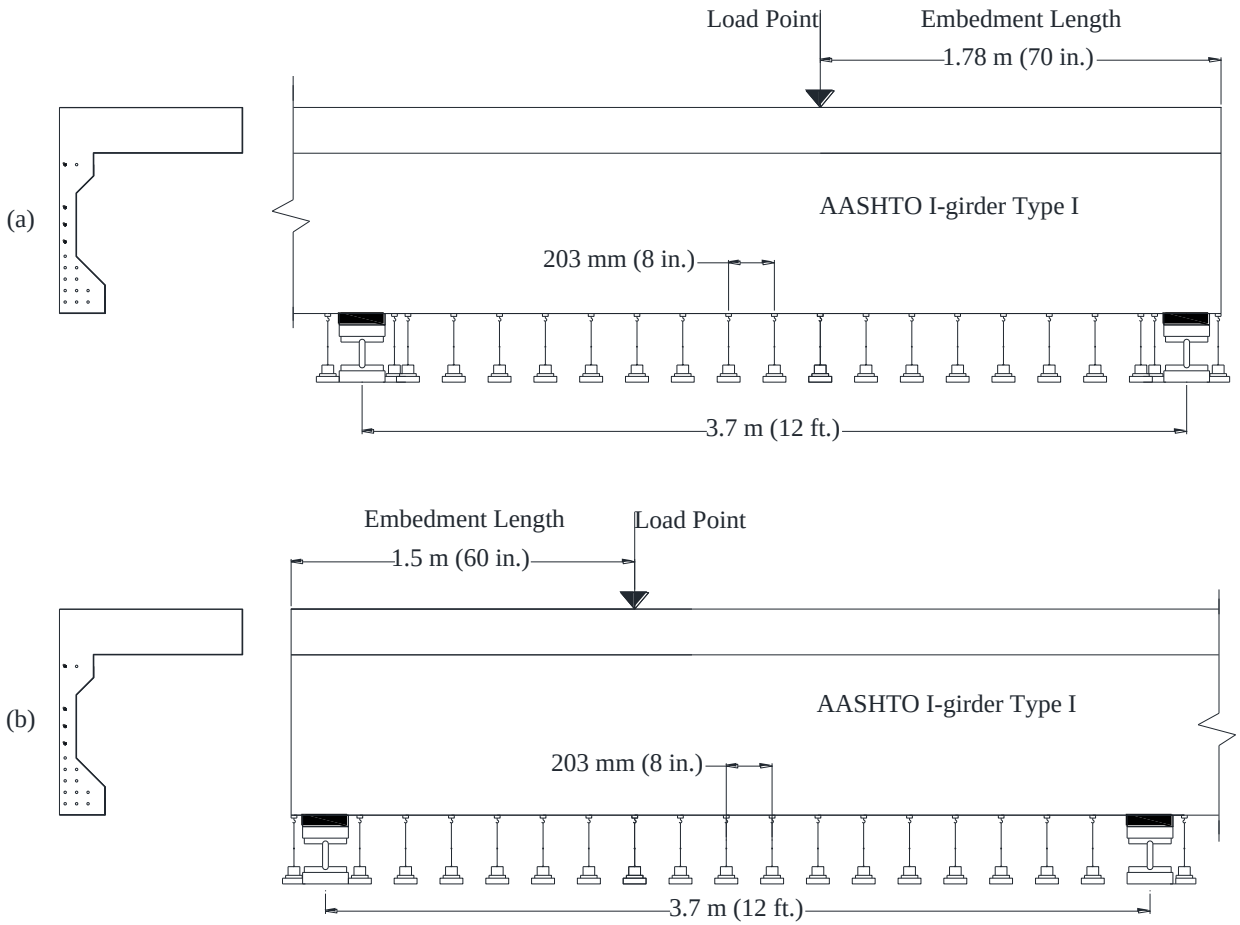

Figure 2-17. String Potentiometer Layout: (a) Shear Test 1 and (b) Shear Test 2.

3 MATERIAL CHARACTERISTICS

3.1 Aramid-Fiber-Reinforced Polymer

Fiber-reinforced polymer bars are composite bars that are manufactured by embedding fibers in a resin matrix. Depending upon the type of fiber, FRP bars may be categorized as aramid, glass (GFRP), or carbon (CFRP) bars. High strength-to-weight ratio, corrosion resistance, ease of placement of the bars, and accelerated implementation due to light weight are the special characteristics that make these bars an appealing substitute for conventional steel in either reinforced or prestressed concrete.

There is little convention, however, regarding the manufacturing process of FRP bars (ACI 4401R-06). Because of this, many factors such as fiber type, volume fraction of fiber, fiber orientation, and even the manufacturing process itself can significantly affect the mechanical properties of FRP. For example, since the fibers are the main loading-carrying component in FRP bars, the fiber-volume fraction and fiber orientation will significantly affect the tensile strength (ACI 4401R-06). For prestressed concrete applications, the tensile characteristics of FRP bars are of significant importance. Unlike steel reinforcement, FRP bars do not yield when loaded in tension. FRP bars with constant cross section and single fiber type display a linear elastic stress-strain relationship until failure.

ACI 440.1R-06 recommends only AFRP and CFRP for prestressing applications. GFRP is not recommended because of its large susceptibility to creep rupture. AFRP was chosen for use in this project because it has a greater strain capacity and lower elastic modulus when compared to CFRP. The low elastic modulus of AFRP reduces the prestress losses due to creep and elastic shortening of the concrete. Large strain capacity allows for considerable post-cracking deflections in the AFRP-reinforced concrete and results in clear warning of imminent failure when compared to CFRP or conventional steel reinforcement (Pirayeh Gar 2013).

In this project, 10-mm (0.394-in.) diameter AFRP ARAPREE® bars were used as a substitute for either steel rebar or prestressing strands. The surface of the bars was coated with quartz and resin to create a rough surface and increase the bond strength of the bar. The manufacturer reports the tensile strength, elastic modulus, and fiber content of the AFRP bars as 1400 MPa

(203 ksi), 60 GPa (8702 ksi), and 50 percent, respectively. Table 3-1 shows the detailed material properties given by the manufacturer. Pirayeh Gar (2012) has recently investigated the uniaxial characteristics of 10-mm (0.394-in.) diameter ARAPREE® bars by conducting tensile tests, short-term and long-term creep and relaxation tests, and tension stiffening tests.

Table 3-1. ARAPREE® 10 Material Properties.

Material	Fiberglass	Resin	Sand
Density, kg/m^3 (lb/ft.^{3})	1400 (87.4)	1150 (71.8)	2650 (165.4)
Minimum Tensile Strength, MPa (ksi)	2800 (400)	55 (8)	N/A
Minimum Breaking Elongation (%)	2.8	2	N/A
Minimum Elastic Modulus GPa (ksi)	120 (17,400)	N/A	N/A
Composition	N/A	N/A	SiO_2 > 98%
Grading Curve	N/A	N/A	0.15/0.3 mm

Tensile tests on bare bars were conducted under displacement control according to ASTM D638 to determine the tensile strength, elastic modulus, and strain capacity of the AFRP bars. Six ARAPREE® bar specimens with a 10-mm (0.393-in.) diameter and 1420-mm (55.9-in.) length were tested under uniaxial tensile load. The anchorage system consisted of steel pipes with a 457-mm (18-in.) length, 48-mm (1.9-in.) diameter, and 5-mm (0.2-in.) wall thickness, which were filled with an expansive and quick-setting grout called Shep Rock. The anchorage steel pipes were gripped by the jaws of a 250-kN (56.2-kips) MTS® machine where the load was monotonically applied at a rate of 22 kN (5 kips) per minute, according to ASTM D638. The applied load was recorded via a load cell connected to the MTS® machine, and the elongation of the specimen was measured through strain gages mounted at the middle of the bar.

For all specimens, the bar ruptured in a brittle fashion and resulted in a linear stress-strain relationship, as shown in Figure 3-1. No local failure was seen at the anchorage, indicating sufficient grip of the bar inside the pipe. The tensile test results are displayed in Table 3-2 (Pirayeh Gar 2012). The means of elastic modulus and strain capacity are equal to 69 GPa (10,000 ksi) and 0.02 mm/mm (0.02 in./in.), respectively, with small standard deviations. Given

a linear stress-strain relationship, the dependable value for ultimate stress can be calculated as 69,000 × 0.02 = 1380 MPa (200 ksi), which is very close to the lower bound of 95 percent confidence interval equal to 1457 − 63.4 = 1393.6 MPa (202 ksi). According to ACI 440.4R (2004), the longitudinal tensile strength of ARAPREE® is expected to be between 1200 MPa (174 ksi) and 1500 MPa (218 ksi), the modulus of elasticity between 62GPa (9.0 ksi) and 64 GPa (9.3 ksi), and the maximum longitudinal strain about 0.024 mm/mm (in./in.). The tensile strength and strain capacity was in the acceptable range; however, the elastic modulus was greater than what has been suggested, 62–64 GPa (9.0–9.2 ksi). According to ASTM A416, the stress-relieved seven-wire strands (Grade 270) have the ultimate strength 1860 MPa (270 ksi), elastic modulus 186 GPa (26977 ksi), and strain capacity 0.04 mm/mm (in./in.). The strands are typically prestressed up to 70–75 percent of the ultimate strength, where the yielding is at 85 percent of ultimate strength corresponding to the 0.01 strain. Comparison shows that the ultimate strength, strain capacity, and elastic modulus of an ARAPREE® bar with a 10-mm (0.393-in.) diameter are about 75 percent, 50 percent, and 37 percent of that of prestressing steel strands, respectively.

Table 3-2. Tensile Test Results (Pirayeh Gar 2012).

Specimen	Ultimate Stress (MPa [ksi])	Strain Capacity	Elastic Modulus (GPa [ksi])
1	1549.9 (225)	0.022	70.4 (10,211)
2	1448.2 (210)	0.021	68.9 (9993)
3	1431.3 (208)	0.021	69.2 (10,037)
4	1358.8 (197)	0.021	64.7 (9384)
5	1464.2 (212)	0.021	69.7 (10,109)
6	1489.1 (216)	0.020	74.4 (10,791)
Mean	**1457 (211)**	**0.021**	**69.38 (10,063)**
Standard Deviation (Unbiased Estimator)	**63.4**	**0.0006**	**3.16**

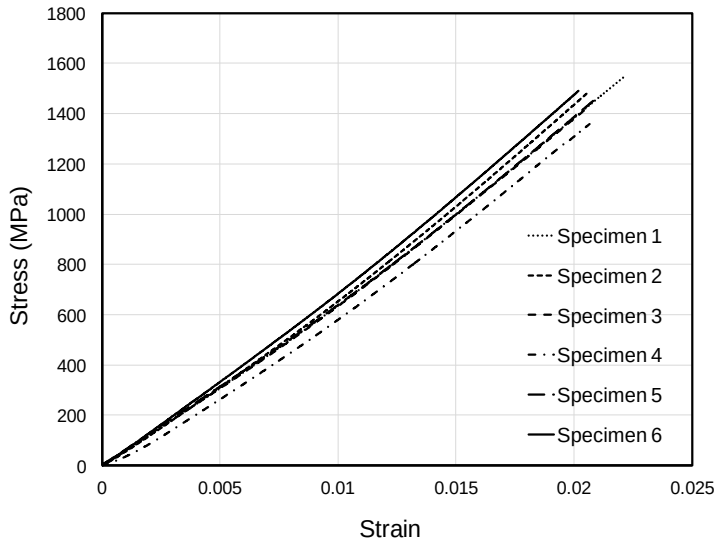

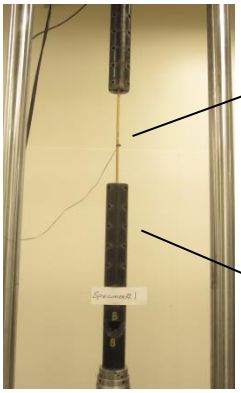

ARAPREE® bar instrumented with strain gage

Gripping system of MTS® machine

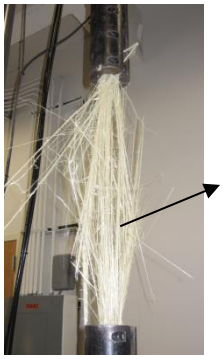

Brittle failure (rupture of tendons)

Figure 3-1. Tensile Test of AFRP ARAPREE® Bars (Pirayeh Gar 2012).

Relaxation and creep tests were performed using a newly developed potted anchorage system (Pirayeh Gar 2012). The anchorage system was composed of a steel pipe with a 457-mm (18-in.) length, 48-mm (1.9-in.) outer diameter, and 5-mm (0.2-in.) wall thickness filled with an expansive and quick-setting grout. The AFRP bar was passed through the center of the pipe and held in place by plastic stoppers, which had central holes drilled through the center. Two surface holes were drilled in the pipe to allow for injecting the grout. The grout was poured through the first hole until the grout came out the second hole to ensure that no air bubbles were present. Figure 3-2 presents the experimental setup for the preliminary anchorage tests. The pipe at the dead end was grouted first and left to set. The live end consisted of one pipe in front of and another behind the hydraulic jack. The front pipe was grouted, and then after 3 hours, the hydraulic jack was pumped to push the front pipe. The rear locking pipe was then injected with grout to lock the bar, and then after 3 hours, the hydraulic jack was released. The bars were

successfully prestressed to 60 percent of the bar capacity, and the anchorage was able to sustain the load for a long time without significant prestressing loss. The prestressing loss after 100 hours was less than 5 percent.

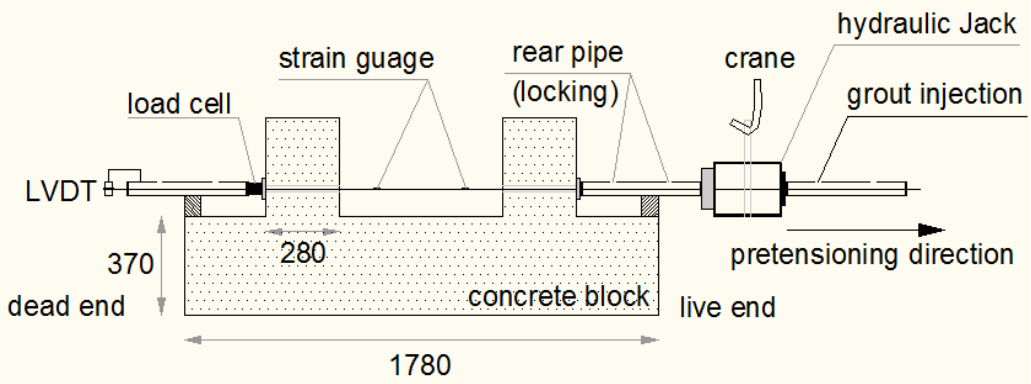

Figure 3-2. Experimental Setup for Preliminary Anchorage Tests (Pirayeh Gar 2012).

The relaxation and creep tests were conducted (Pirayeh Gar 2012) using the same anchorage system and experimental setup shown in Figure 3-2. The long-term relaxation test was conducted over a 1000-hour period with AFRP bars prestressed to 50 and 60 percent. After 70 hours, concrete was poured around the bare bars to mimic the actual surrounding environment. A load cell was installed at the dead end to measure the total prestressing loss, and an LVDT was installed at the live end where the bar extended from the anchorage pipe. The total loss was composed of the relaxation of the bar, slippage of the bar inside the grout pipe, and the increase in strain due to creep. The results of the relaxation tests are shown in Table 3-3. Based on these results, the relaxation loss varies between 6 and 10 percent depending on the initial prestressing ratio. For comparison, the prestressing losses after 1000 hours for conventional stress-relieved steel strands is between 8 and 12 percent (Naaman 2004).

Table 3-3. Results of Relaxation Tests (Pirayeh Gar 2012).

Specimen	Initial Prestressing (%)	Relaxation Loss (%)	Average Relaxation Loss (%)
1	49.4	5.5	7.5
2	47.5	9.2	
3	49.7	8	
4	57.5	10.2	9.7
5	57.8	14.6	
6	55	9.3	

Long-term creep tests were conducted using the same experimental setup and instrumentation as the relaxation tests with the addition of disc springs at the dead end to keep the load constant. The long-term creep deformation was composed of primary, secondary, and tertiary phases. The primary phase started with a high strain rate and quickly converged to the secondary phase observed by a constant strain rate. If the prestressing load was very high, a tertiary phase was observed where the strain rose considerably, resulting in rupture of the bar. The results of the long-term creep tests are presented in Table 3-4. For specimens prestressed up to 50 percent of ultimate capacity, the rise in strain after 1000 hours is about 4 percent. Results show that for an initial prestressing of 50–60 percent, the tertiary phase is unlikely to be reached. Due to complication and eventual rupture of the AFRP bars, initial prestressing of 60 percent of ultimate capacity is not recommended.

Table 3-4. Results of Long-Term Creep Tests (Pirayeh Gar 2012).

Specimen	Initial Prestressing (%)	Duration (Hours)	Rise in Strain (%)
1	50	700	4
2	50	1000	4
3	50	1000	3.5
4	60	550	6.5
5	60	100	1.4
6	60	200	4.5

Short-term creep tests were conducted using the same experimental setup and instrumentation as the tensile tests discussed earlier in the chapter. Five specimens were tested with 80 and 85 percent initial prestressing. Slippage occurred in two of the specimens, which terminated the test prematurely. The primary phase lasted 2.5 and 1 hour for the specimens with 80 and 85 percent prestressing, respectfully. The last specimen prestressed up to 85 percent of ultimate capacity showed step-wise rupture of the fibers and failed suddenly after 2 hours. The results from this test show that initial prestressing significantly affects the creep-rupture strength of the ARAPREE® bars.

3.2 Steel Rebar

Grade 60, D13 (#4), and D16 (#5) steel rebar, according to ASTM A615, was used for the longitudinal and transverse reinforcement in the deck. This rebar has a minimum yield strength, f_y, of 413.7 MPa (60 ksi) and a minimum tensile strength, f_u, of 620.5 MPa (90 ksi). Steel rebar was used in the deck instead of AFRP bars because the topping deck was only modeled to provide composite action with the girder. Figure 2-5 presents the details of the deck reinforcement.

3.3 High-Strength Bolts

In addition to AFRP shear reinforcement, high-strength steel bolts (Grade 8), according to ASTM A354 BD, were used as shear bolts within the deck/girder interface. This could help to achieve the full composite action between the girder and the topping deck. The shear bolts had a diameter of 38 mm (1 in.) and were 381 mm (15 in.) long. The minimum tensile strength was 1035 MPa (150 ksi) per the manufacturer's specifications.

3.4 Grout

A quick-setting expansive cement-based grout was used as the bonding material for the anchorage system, which will be discussed in further detail later in this report. An expansive cement-based grout increases the slipping resistance and prevents stress concentrations by producing lateral pressures of up to 40 MPa (5.8 ksi) on the AFRP bar. A quick-setting grout was selected to accelerate the construction process. Quick-setting grout develops load-bearing properties in less than an hour as opposed to a few days with a non-expansive grout. The grout-to-water ratio is a critical parameter because it significantly influences the compressive strength. If the grout mixture has too much water, its strength will suffer; however, if the mixture lacks water, the grout will not be able to flow properly through the anchorage.

Preliminary tests were carried out to determine the optimum grout-to-water ratio that would provide the required strength while still maintaining the required flowability. A steel pipe with a 457-mm (18-in.) length, 48-mm (1.9-in.) outer diameter, and 5-mm (0.2-in.) wall thickness was used to examine the flowability of the grout inside the pipe anchorage. A section of 15-mm (0.6-in.) diameter prestressing steel was passed through the center of the pipe and held in place by a plastic stopper with a central hole. Two surface holes were drilled in the pipe to allow for injecting the grout. The grout was poured through the first hole until the grout flushed the pipe's surface at the second hole to ensure that no air bubbles were entrapped inside the pipe. If the pipe could be filled completely before the grout set, the mixture was considered flowable. For each trial, the amount of water was held constant, while the amount of grout powder was varied.

The manufacturer suggests 1 pint of water to 5 lb. of grout powder for a pourable consistency. This was the starting point for the preliminary tests. The manufacturer's grout-to-water ratio proved to be too stiff for use in this particular application. After multiple trials, a

grout-to-water ratio of 8:3 by volume was determined to be able to provide the required strength and flowability. This grout-to-water ratio corresponds to 1 pint of water to 3.5 lb. of grout. The workability and flowability of the grout decreases quickly once the grout is finished mixing. The grout becomes unworkable in about 5 minutes, and it takes about 1 minute to fill each 457-mm (18-in.)-length pipe with grout. The expansive grout fully sets in 10 minutes and achieves load-bearing and bond strength properties in about 45 minutes. Table 3-5 shows the compressive strengths of the grout given by the manufacturer based on the ASTM C 109 standard using 50-mm (2-in.) cubes at 22° C (72° F). The early expansion of this grout according to ASTM C 157 is 0.04 percent.

Table 3-5. Compressive Strength of Expansive Grout (MPa [ksi]).

Setting Time	Compressive Strength
3 Hours	20 (3.0)
1 Day	28 (4.1)
7 Days	39 (5.8)
28 Days	55 (8.0)

Grout cubes were tested to find the compressive strength of the grout mix corresponding to a grout-to-water ratio of 1 pint of water to 3.5 lb. of grout. The average compressive strength after 7 days was 35 MPa (5.1 ksi). This is less than the manufacturer's specifications because the mixture used for this project contained more water for proper flowability.

3.5 Self-Consolidating Concrete

Self-consolidating concrete (SCC), or self-compacting concrete, is a relatively recent advancement in the concrete industry. SCC has a high slump and consolidates under its own weight. Therefore, it is poured requiring no mechanical vibration, which allows the mix to be used for heavily congested reinforced shapes, particularly bridge deck girders.

SCC was first used in Japan in the late 1980s and gained wide acceptance for casting in congested members as well as concrete placement in difficult-to-access areas, where

consolidation may not be feasible. SCC is considered a new class of high-performance concrete (HPC) used to facilitate and accelerate concrete placement without hindering in-situ properties and durability (Khayat 1999). The creation of this HPC that no longer requires mechanical vibration allows for less labor and increased worker safety, quicker installations, and reduced construction noise (Okamura and Ozawa 1996).

The modern concrete industry is more than aggregates, water, and cement. It has become more common to see a variety of cementitious components, such as fly ash, or chemical admixtures, such as superplasticizers, to give concrete certain desired characteristics. Okamura and Ouchi (2003) reference Okamura and Ozawa as achieving self-compactibility by limited aggregate content, a low water–cement powder ratio, and the use of superplasticizer.

The AASHTO I-girder Type I is made using SCC. Fresh property tests of the concrete, such as slump flow and unit weight, and making molds for future hardened material properties testing were conducted on the day of the concrete pour of the full-scale specimen. Hardened properties tests, such as compression strength, modulus of rupture, splitting tensile strength, modulus of elasticity, and shrinkage, are measured based on different test sample ages per standard codes of practice (ASTM C39, C78, C496, C469, and C596, respectively). Shrinkage and durability tests show the long-term characteristics of SCC considering the environmental effects.

Fresh property tests of the concrete such as slump flow and unit weight were conducted on the day of casting the full-scale specimen. Fly ash and chemical admixtures, such as superplasticizers and retarders, are used in SCC mixtures in order to achieve low water-cement ratios, achieve a high slump, and maintain workability. When determining water content for a mix design, the operator must consider the moisture content in the aggregates and adjust accordingly.

The slump flow of the concrete mix was tested in accordance with ASTM C1611. This test is performed using the same slump cone used for the slump test of conventional concrete. The cone can be used in the standard upright position or inverted position (Daczko 2012). Rather than filling the cone in three lifts with rodding as with conventional concrete, the cone is fill in one lift without rodding since the concrete consolidates on its own. Figure 3-3 shows the slump flow test.

Figure 3-3. Slump Flow Test.

Once the cone is lifted, the diameter of the spreading of the fresh concrete is measured rather than the height of displacement as done with conventional slump testing. When performing this test, the operator must also take care to observe that there is no standing water around the slump diameter to ensure there is no segregation of materials and that the concrete is well mixed. During this test, whether it is conducted by one operator or multiple operators, the slumps shall not differ by more than 76.2 mm (3 in.) (ASTM C1611). The optimum slump diameter is within the range of 558 to 711 mm (22 to 28 in.).

The unit weight of the concrete mix was tested in accordance with ASTM C138. First, the weight of the empty unit weight bucket was determined. The bucket was 0.01 m^3 (0.5 $ft.^3$), allowing for a maximum-size coarse aggregate of 50.8 mm (2 in.). The bucket was filled in three lifts, each rodded 25 times and the sides of the bucket tapped with a rubber mallet 10–12 times. According to ASTM C138, "the bucket is to be made of steel or some other suitable metal." This ensures the bucket will not lose its shape or affect the contents that have been prepared before weighing the full bucket. Since SCC consolidates itself, rodding may be deemed unnecessary in this test. The unit weight was then calculated by subtracting the weight of the empty bucket from the weight of the full bucket and dividing by the volume of the bucket.

Mechanical properties testing results are used for two primary purposes: engineering design (e.g., failure theories based on strength, or deflections based on elastic constants and component geometry) and quality control either by the materials producer to verify the process or by the end user to confirm the material specifications (University of Washington). For the purpose of this research, the mechanical properties of the concrete were tested with test specimens of

100×200-mm (4×8-in.) cylinders and 150×150×500-mm (6×6×20-in.) beams as specified in ASTM test procedures. While these specimens are presumed to have minimal flaws, they provide valuable information about the materials used in the full-scale specimens. Specimens were fabricated and stored under laboratory conditions as a control group. Through the uniformity of testing, according to ASTM standards, the results had reliability and repeatability with the same materials. These standards prescribe the method by which the test specimen are prepared and tested, as well as how the test results are analyzed and reported.

Compressive strength concrete cylinder specimens were tested in accordance with ASTM C39. Three 100×200-mm (4×8-in.) cylinder samples were made for compressive strength (f'_c) for each test age. The girder and deck samples were cured in situ, next to the girder, for 4 days and 1 day, respectively. The specimens were then transported to College Station, Texas; the molds were removed and the samples stored in an environmental curing room of 25° C and greater than 97 percent relative humidity. Compressive strength was evaluated at 16 hours and 3, 7, 28, and 56 days as well as on the day of the large-scale tests. Type III Portland cement was used in order to achieve high early strength and allow the forms to be removed within a day after casting.

The modulus of elasticity of the concrete specimens was tested in compression in accordance with ASTM C469. Three 100×200-mm (4×8-in.) cylinder samples were made for modulus of elasticity (MOE) for each test age. The curing procedure was the same as the compressive strength test. The MOE was evaluated at 7, 28, and 56 days.

The MOE of concrete is influenced by the porosity of the cement paste, which is a function of the water/cement (w/c) ratio used, and the relative proportion of cement and aggregate (Gutierrez and Manuel 1995). For the mixes used, some of the water was accounted for as moisture in the aggregates in the w/c ratio. Typical w/c ratios range from 0.4 to 0.6, but for higher-strength concrete, lower w/c ratios are used with superplasticizers to maintain flowability.

Splitting tensile specimens were tested in accordance with ASTM C496. Three 100×200-mm (4×8-in.) cylinder samples were made for splitting tensile strength (STS) for each test age. The curing procedure was the same as that for the compressive strength test. STS was evaluated at 7, 28, and 56 days.

Studies show that the true tensile strength, as obtained from the splitting tensile test, is between 65 and 75 percent of the modulus of rupture for normal concrete. The acceptance of the STS is based on the knowledge that the stress distribution is uniform along the vertical diameter of the cylinder, which is the plane of principle tensile stress for roughly 80 percent of its length (SeshaPhani et al. 2013)

Modulus of rupture specimens were tested in accordance with ASTM C78. Three 150×150×500-mm (6×6×20-in.) beam samples were made for each test age of modulus of rupture (MOR). The curing procedure was the same as that for the compressive strength test. MOR strength was evaluated at 7, 28, and 56 days. A 89-kN (20-kips) capacity MTS® machine was used to evaluate MOR at a load rate of 13.6 kg/sec (30 lb/sec) until failure.

Research shows that the MOR decreases with increasing beam size. The cause of the size effect on MOR stems from the semi-brittle nature of the material, and particularly the stress redistribution and energy release caused by a fracture within a large fracture process zone (Bazant and Novak 2001). The MOR test is deemed invalid if the beam does not break somewhere in the middle third region. For instance, the beams used for this project were 150×150×500 mm (6×6×20 in.). The testing apparatus allows for a 25.4-mm (1-in.) overhang on either side of the roller supports so that the remaining 457 mm (18 in.) in length is the region of interest. When this length is broken into thirds, the beam must fail with the crack propagation beginning and ending somewhere in the middle third region of the beam. The SCC mix design used for the bridge deck girder is shown in Table 3-6.

Table 3-6. Design Summary.

Materials Properties		Type	Supplier		Weights @ Saturated Surface Dry (SSD)	
					1 Cubic Meter (CM)*	% Vol.
Avg. Target f'_c (MPa [ksi])	12-hr			44 (6.4)		
	7d			62 (8.9)		
	28d		0.31	75 (10.9)		
w/c ratio				380 (640)	0.25	
Cement (kg/m^3 [lb./yd.^{3}])		III	Capitol	126 (213)	380 (640)	15.7
Fly Ash (kg/m^3 [lb./yd.^{3}])				157 (264)	126 (213)	5.2
Water kg/m^3 [lb./yd.^{3}])				0.75	128 (216)	5.3
Max Nominal Aggregate Size (mm [in.])				Capitol-Marble Falls		
Aggregate (kg/m^3 [lb./yd.^{3}])	Coarse	Concrete rock	Capitol-Austin River	1016 (1712)	1025 (1727)	42.5
	Fine	Washed river sand	1508 (51)	736 (1240)	753 (1270)	31.2
Admixtures (ml [oz.])		High-Range Water-Reducing Admixture (HRWRA)	Sika 4100	503 (17)		
		Retarder	Sika Plastiment			

*With aggregate absorption corrections

Type III Portland cement was used in order to achieve high early strength and allow the forms to be removed within a day after casting. Fly ash is used in order to decrease the required amount and is cost effective. Fly ash and chemical admixtures, such as superplasticizers and retarders, are used in SCC mixtures in order to achieve low water-cement ratios, achieve a high slump, and maintain workability. When determining water content for a mix design, the operator must consider the moisture content in the aggregates and adjust accordingly.

The mix design was corrected for aggregate moisture content. The aggregate properties are provided in Table 3-7.

Table 3-7. Heldenfels Aggregate Specific Gravity and Absorption.

Aggregate	Specific Gravity	Absorption
Coarse	2.78	15.41
Fine	2.58	30.13

3.6 Mechanical Properties

3.6.1 Test Procedure

The SCC was mixed on site at the precast plant in San Marcos, Texas; the girder and the deck were cast on separate days. For each day of casting, samples were made to test the fresh and mechanical properties of each concrete batch. The main mechanical properties of interest at certain test ages (days) were compressive strength (f'_c), MOE, STS, MOR, and shrinkage. The girder was poured with one batch, and the deck required two batches, each batch having a maximum volume of 3.06 m^3 (4 $yd.^3$). Specimens made from the second batch for the deck only included 100×200-mm (4×8-in.) cylinders for compressive strength tests as a reliability check of the first batch. Table 3-8 summarizes the test matrix and the test ages of each mechanical characteristic for the first batch of the girder and the deck. All laboratory concrete samples were made and cured in accordance with ASTM C31.

Table 3-8. Test Matrix of Mechanical Properties.

Age of Samples	Mechanical Tests			
	f'_c	MOE	MOR	STS
1d	X	-	-	-
3d	X	-	-	-
7d	X	X	X	X
28d	X	X	X	X
Day of Test (42d)	X	-	-	-
56d	X	X	X	X

The compressive strength of concrete cylinder specimens was tested in accordance with ASTM C39. Three 100×200-mm (4×8-in.) cylinder samples were made for compressive strength (f'_c) for each test age. The girder and deck samples were cured in situ, next to the girder for 4 days and 1 day, respectively. The specimens were then transported to College Station, Texas; the molds were removed and the samples stored in an environmental curing room of 25° C and greater than 97 percent relative humidity. Compressive strength was evaluated at 16 hours and 3, 7, 28, and 56 days as well as on the day of the test (42 days).

The MOE of the concrete specimens was tested in compression in accordance with ASTM C469. Three 100×200-mm (4×8-in.) cylinder samples were made for the MOE for each test age. The curing procedure was the same as that for the compressive strength test. MOE was evaluated at 7, 28, and 56 days.

Figure 3-4 shows the MOE testing apparatus with two LVDTs on either side of the cylinder. The metal cage that encompasses the cylinder is attached by tightening the screws into the concrete cylinder to hold the cage in place with a 4-in. gage length for the LVDTs.

Figure 3-4. Modulus of Elasticity Testing Apparatus.

The MOE of concrete is influenced by the porosity of the cement paste, which is a function of the w/c ratio used and the relative proportion of cement and aggregate (Gutierrez and Manuel 1995). For the mixes used, some of the water is accounted for as moisture in the aggregates in the w/c ratio. Typical w/c ratios range from 0.4 to 0.6, but for higher-strength concrete, lower w/c ratios are used with superplasticizers to maintain flowability.

Splitting tensile specimens were tested in accordance with ASTM C496. Three 100×200-mm (4×8-in.) cylinder samples were made for STS for each test age. The curing procedure was the same as the compressive strength test. STS was evaluated at 7, 28, and 56 days.

As seen in Figure 3-5, the splitting tensile test is performed with the cylinder on its side. As the force is applied by the MTS® machine, a vertical crack should begin to appear and propagate down the vertical diameter of the cylinder. The crack will eventually propagate to failure by splitting the cylinder into two halves.

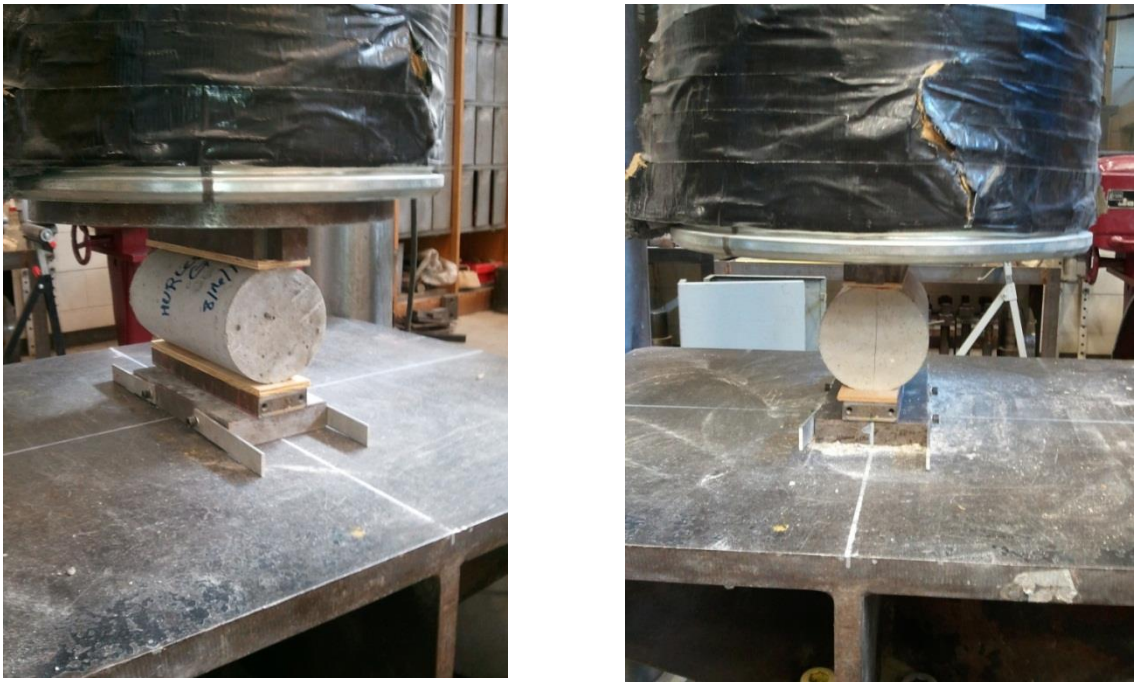

Figure 3-5. Splitting Tensile Test.

MOR specimens were tested in accordance with ASTM C78. Three 150×150×500-mm (6×6×20-in.) beam samples were made for each test age of MOR. The curing procedure was the same as the compressive strength test. MOR strength was evaluated at 7, 28, and 56 days. A 89-kN (20-kips) capacity MTS® machine was used to evaluate MOR at a load rate of 14 kg/sec (30 lb./sec) until failure.

Research shows that MOR decreases with increasing beam size. The cause of the size effect on MOR stems from the semi-brittle nature of the material, and particularly the stress redistribution and energy release caused by a fracture within a large fracture process zone (Bazant and Novak 2001). The MOR test is deemed invalid if the beam does not break somewhere in the middle third region. For instance, the beams used for this project were 150×150×500 mm (6×6×20 in.). The MOR testing setup and tested beams are shown in Figure 3-6. The testing apparatus allows for a 25.4-mm (1-in.) overhang on either side of the roller supports so that the remaining 457 mm (18 in.) in length is the region of interest. When this length is broken into thirds, the beam must fail with the crack propagation beginning and ending somewhere in the middle third region of the beam.

Figure 3-6. Modulus of Rupture Testing Apparatus and Tested Beams.

A 2224-kN (500-kips) capacity materials MTS® machine was used to test all mechanical characteristics of the girder and deck mixtures except for MOR. For compressive strength and STS tests, the machine was load controlled at a rate of 14.5 MPa (2.1 ksi) until failure. MOE tests were displacement controlled until failure by using an apparatus with two LVDTs to measure the strain of concrete in compression up to 40 percent of compressive strength at the age of testing.

3.6.2 Test Results

Fresh properties were determined for the SCC mix designs used for the deck. The unit weight was 2371 kg/m^3 (148 lb./ft.^{3}), and the slump flow was 584.2 mm (23 in.). Compressive strength enables the operator to know the strength of the concrete of the full-scale specimen, thus enabling the operator to better predict the failure modes and loads during testing. The trend of compression strength at each test age is shown in Figure 3-7 and Figure 3-8.

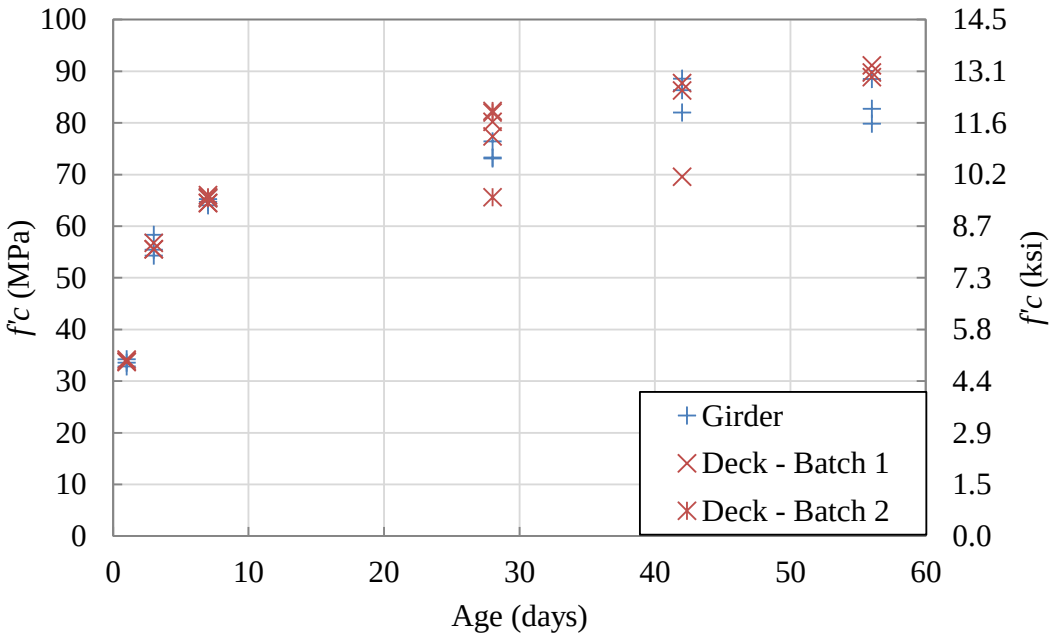

Figure 3-7. Compressive Strength.

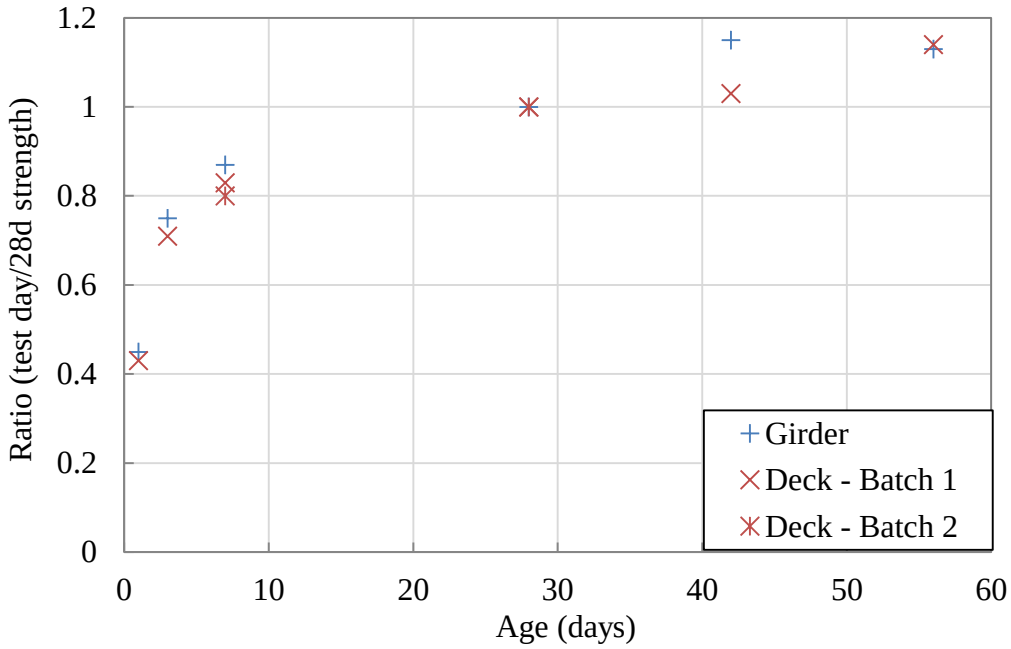

Figure 3-8. Development of Compressive Strength.

Type III cement was used in both the girder and deck mixtures in order to achieve a high early strength. This trend can be seen in the increase of approximately 21 MPa (3 ksi) from

16-hour strength to 3-day strength. The average 3-day strength is approximately 75 percent of the 28-day strength of each batch.

The MOE of concrete is influenced by the porosity of the cement paste, which is a function of the w/c ratio used, and the relative proportion of cement and aggregate (Gutierrez and Manuel 1995). The w/c ratio for this mix was 0.31, where some of the water is accounted for as moisture in the aggregates. Typical w/c ratios range from 0.4 to 0.6, but for higher-strength concrete, lower w/c ratios are used with superplasticizers to maintain flowability. MOE development with age can be seen in Figure 3-9 and compared to compressive strength in Figure 3-10.

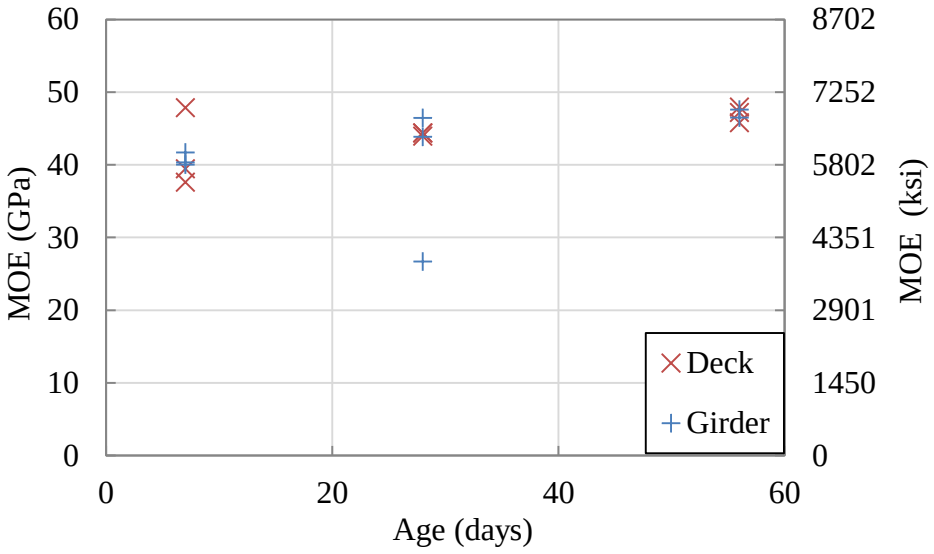

Figure 3-9. Development of MOE.

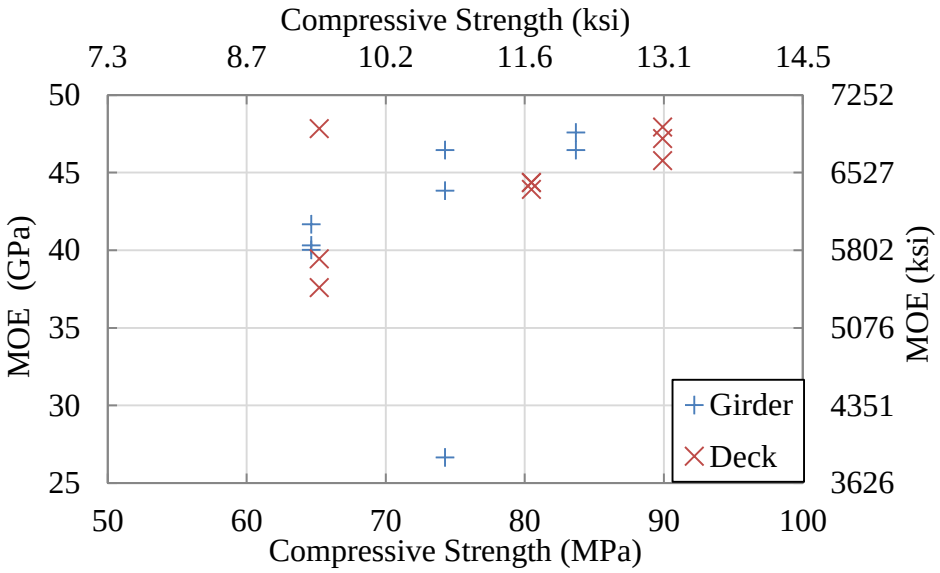

Figure 3-10. MOE.

Research shows that the true tensile strength, as obtained from the splitting tensile test, is between 65 and 75 percent of the MOR for normal concrete (SeshaPhani et al. 2013). The trend of STS at each test age can be seen in Figure 3-11. Figure 3-12 shows the relationship between the average MOR and the STS of the SCC mixtures for the girder and the deck.

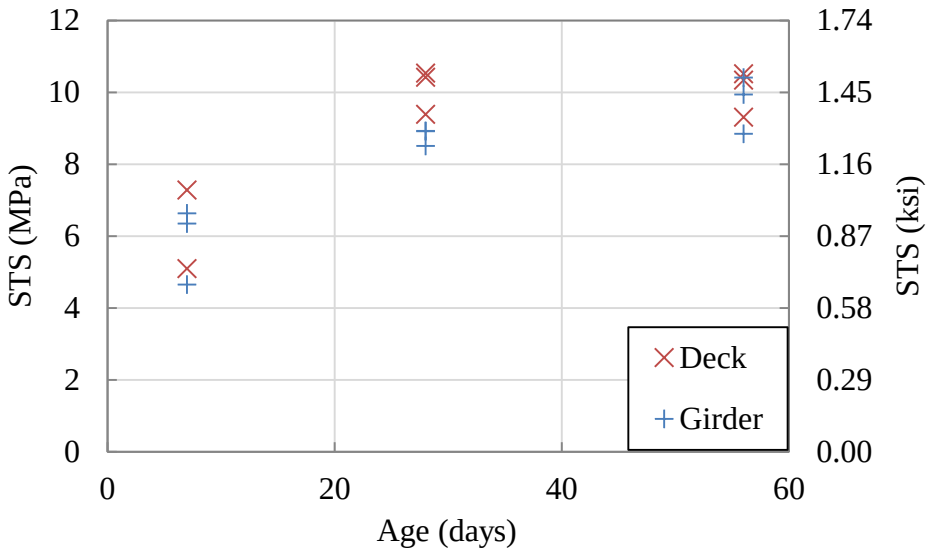

Figure 3-11. Development of Splitting Tensile Strength.

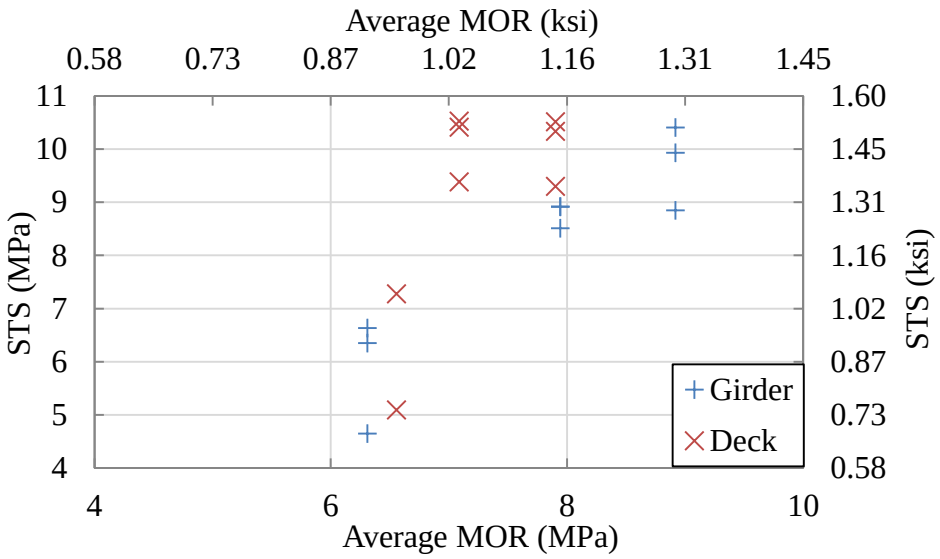

Figure 3-12. STS versus MOR.

Research shows that the MOR decreases with increasing beam size. The cause of the size effect on MOR stems from the semi-brittle nature of the material, and particularly the stress redistribution and energy release caused by a fracture within a large fracture process zone (Bazant and Novak 2001). The MOR test is deemed invalid if the beam does not break somewhere in the middle third region. For instance, the beams used for this project were 150×150×500 mm (6×6×20 in.). The testing apparatus allows for a 25.4-mm (1-in.) overhang on either side of the roller supports so that the remaining 457 mm (18 in.) in length is the region of interest. When this length is broken into thirds, the beam must fail with the crack propagation beginning and ending somewhere in the middle third region of the beam. The trend of MOR at each test age can be seen in Figure 3-13. Figure 3-14 shows the relationship between the compressive strength and the MOR of the SCC mixtures for the girder and the deck.

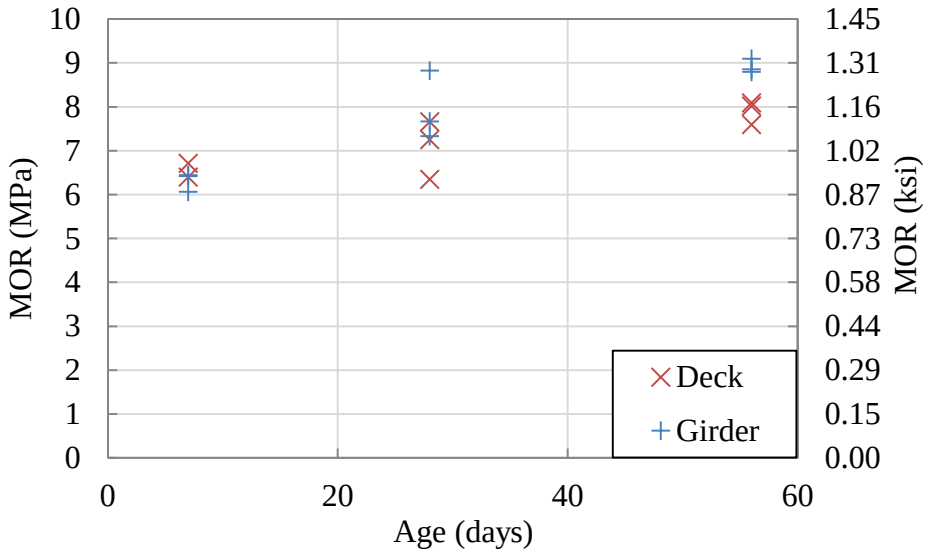

Figure 3-13. Development of Modulus of Rupture.

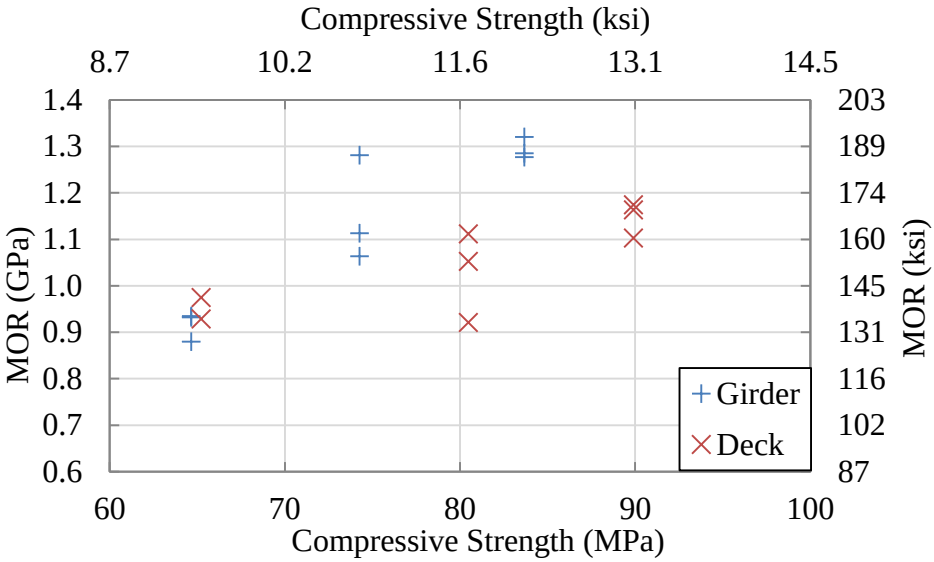

Figure 3-14. MOR.

4 PRESTRESSING ANCHORAGE SYSTEM

4.1 Introduction

Due to the weak strength of FRP bars in the transverse direction, the prestressing level (prestressing force over strength) is a critical design parameter that needs to be carefully selected to avoid either short-term or long-term failure. For instance, ACI 440.4R (2004) limits the prestressing level to 0.5 and 0.65 for AFRP and CFRP bars, respectively. This limitation depends upon the anchorage type and creep-rupture characteristics of FRP bars. It has also been stipulated that the prestressing level should not exceed 65 percent of the anchorage capacity (ACI 440.4R 2004), and also the tertiary stage of creep rupture should never be reached. Thus, GFRP bars are not recommended for prestressing application since they have poor resistance to creep.

Therefore, a practical anchorage system should have a minimum capacity equal to the prestressing level with a safety factor of 0.65, and transfer the prestressing load to the bar in a uniform manner to avoid stress concentration, which may cause fatigue and creep issues. Furthermore, the anchorage system should sustain the load without any considerable loss in prestressing force. With that being said, a practical and reliable anchorage system is a design concern because FRP bars are weak in the transverse direction, and the fibers can be damaged under the gripping force of the anchorage.

For prestressing application, there are basically two common types of anchorage systems, wedge anchorages and potted anchorages. Wedge anchorages are composed of a number of wedges, a conical barrel, and an optional sleeve. Wedge anchorages are mostly preferred over potted anchorages because of wedge anchorages' reusability, ease of assembly, compactness, and familiarity. Figure 4-1 shows a wedge anchorage system schematically. As the bar is forced into the conical barrel, the wedges apply a compressive force along the bar. These compressive forces grip the bar and allow the bar to be pre-tensioned. A sleeve can also be used to uniformly distribute the compressive forces and protect the bar from premature failure due to compressive stress concentrations.

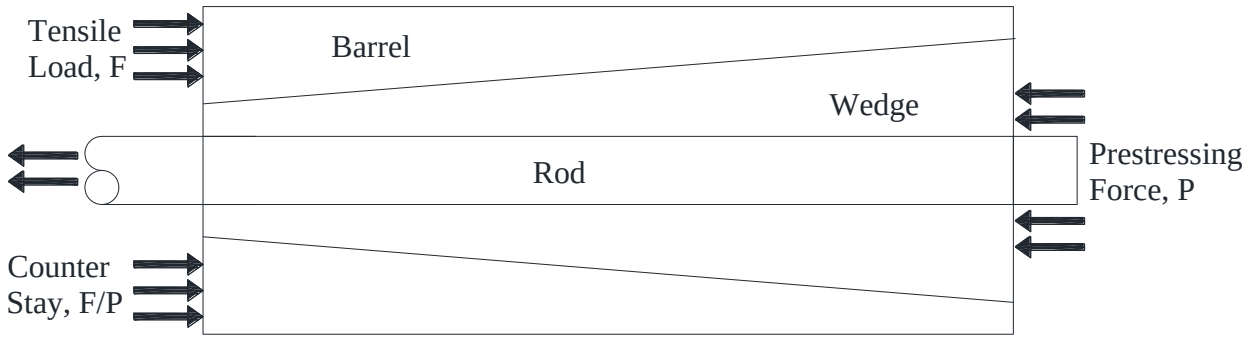

Figure 4-1. Schematic of Conventional Wedge Anchor System (Bennitz and Schmidt 2012).

4.2 State of the Art

4.2.1 Wedge Anchorage Systems

Considerable experimental investigations have been conducted on wedge anchorage systems for use in FRP prestressed concrete. Conventional wedge anchorages consist of a multi-wedge and barrel system, where the wedge applies a transverse gripping force to the exterior surface of the prestressing strand. Because FRP bars are not strong in the transverse direction, the wedge tends to crush the fibers with a large stress concentration, followed by a premature failure (Al-Mayah et al. 2001b, Bennitz and Schmidt 2012). Therefore, to overcome this problem, the conventional wedge anchorage needs to be properly modified to avoid direct contact between the wedge and FRP bar, and also to transfer the gripping force in a more distributed manner. Using a sleeve between the wedge and FRP bar is one solution that researchers have recently introduced and investigated (ACI 440.4R 2004).

Shrive (2000) introduced a stainless steel anchorage system, similar to that shown in Figure 4-2, for CFRP bars and investigated the effect of wedge, sleeve, and barrel material. The preliminary tests on wedge anchorage without a sleeve showed high stress concentrations and resulted in premature failure due to crushing of the fibers. In the next step, a sleeve was used to alleviate the stress concentration and to avoid premature failure. A sandblasted copper sleeve of 0.48-mm (0.019-in.) thickness was tested against an aluminum sleeve of 0.64-mm (0.025-in.) thickness. The aluminum sleeve performed better than the copper sleeve because the softer aluminum had the ability to plastically deform and flow into the indentations of the CFRP bar, providing a better grip. The authors recommend the use of steel wedges because they performed better than either aluminum or copper wedges in preliminary tests.

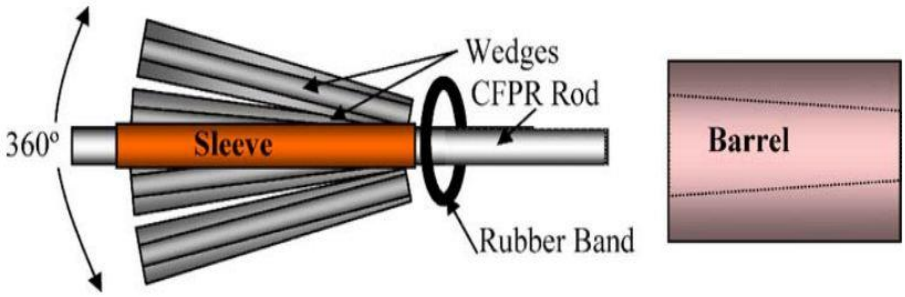

Figure 4-2. Schematic of a Wedge Anchorage System (Al-Mayah et al. 2006).

Al-Mayah et al. (2001a) investigated a similar wedge-type anchorage system consisting of a stainless steel barrel, a four-piece stainless steel conical wedge set, and an aluminum sleeve. Two LVDTs were attached to the CFRP bar to measure the slip of the bar and sleeve relative to the barrel. Prestressing loads equal to 48, 63, 77, and 96 percent of the ultimate strength of the CFRP bar were applied. As shown in Figure 4-3, the test results revealed three distinct regions of slippage. When the load reached the first threshold value (F1), only the bar moved. This behavior continued until the load reached the second threshold value (F2) when the sleeve started to slip. At a load of 100 kN (22.5 kips), the bar moved by an amount Slip1, and the sleeve moved by an amount Slip2. During the third stage, the sleeve and wedges moved together. This slip behavior was similarly observed in all the tests conducted, where the threshold values F1 and F2 varied for each experiment. As the prestressing load increased, the slippage of the bar decreased due to the larger gripping force. Al-Mayah recommended that a prestressing load in the range of 60 to 80 percent of the ultimate strength of the bar be applied using the anchorage system tested.

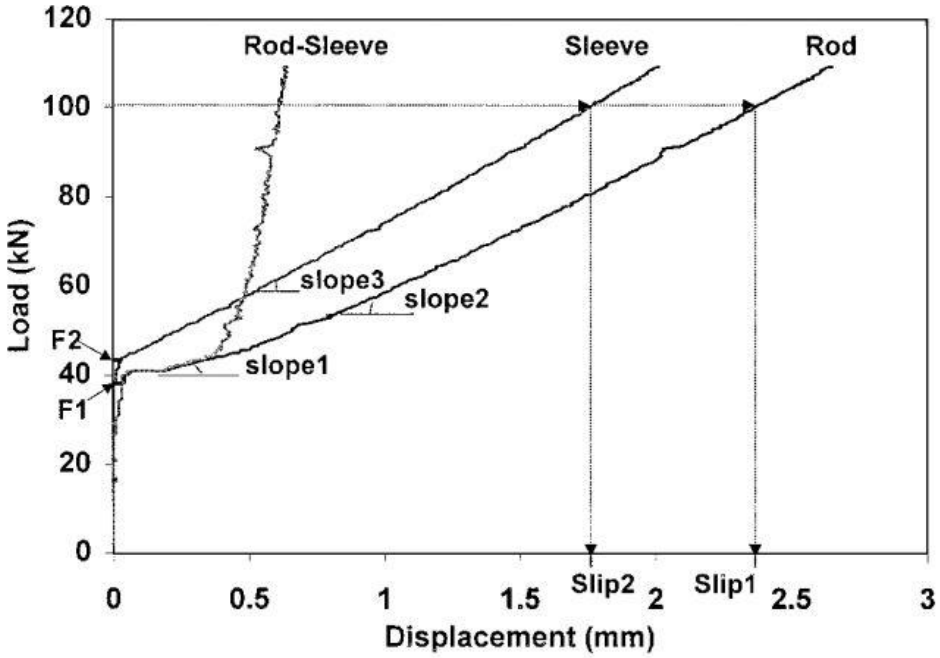

Figure 4-3. Typical Slip Behavior of Wedge Anchorage Components (Al-Mayah et al. 2001b).

Al-Mayah et al. (2001b) also studied the effect of sleeve material on performance of the anchorage for CFRP bars. The researchers designed the sleeve material such that it would be able to plastically deform into the indentations of the CFRP bar but be strong enough not to fail during the prestressing process. The same prestressing loads of 48, 63, 77, and 96 percent of the ultimate strength of the bar were used. Sleeves with an inner diameter of 7.9 mm (0.31 in.) and outer diameter of 9.18 mm (0.39 in.) made of 6061-T6 aluminum and oxygen-free high thermal conductivity (OFHC) copper were tested. The typical slippage showing three distinct regions was observed. The static tests showed that the copper sleeve performed poorly at low presetting loads but better at high presetting loads, when compared to aluminum sleeves. Due to unreliability, however, further investigation was recommended as to the performance of copper sleeves.

Although the experimental tests showed that using a sleeve could enhance the load capacity of the wedge anchorage, the bond strength between the sleeve and FRP bar could still be improved to reduce the slippage and the subsequent prestressing loss. For this purpose, the effect of sandblasting the inner surface of the sleeve was investigated by Al-Mayah et al. (2005). The sandblasting technique increases the coefficient of friction between the sleeve and FRP bar,

thereby improving the bond strength. A similar load-slippage relationship to that of Figure 4-3 was observed. In fact, this graph represents the stick-slip behavior of the anchorage. When the contact pressure was low, the load rose to threshold level F1, and the bar gradually slipped out of the sleeve. When the contact pressure was high, region2 was drastically reduced, and sticking occurred after a slippage of about 10–25 mm (0.4–1.0 in.). These tests have revealed that complete sticking occurred earlier, and within a shorter sliding distance, when a sandblasted sleeve was used. Also in the case of very high contact pressures, region3 appeared where sticking occurred after a little slip, which is a desired outcome for a CFRP anchorage system. This experiment confirmed that that the friction coefficients and the contact pressure are the two critical design parameters that can improve sleeve-to-bar bond strength. In an ideal design, the contact pressure should be lowest at the loading end and highest at the free end, where little to no tensile stress is applied, as shown in Figure 4-4. This ideal contact pressure distribution prevents stress concentrations from forming at the loading end of the anchorage, which in turn prevents premature failure due to crushing of the bar.

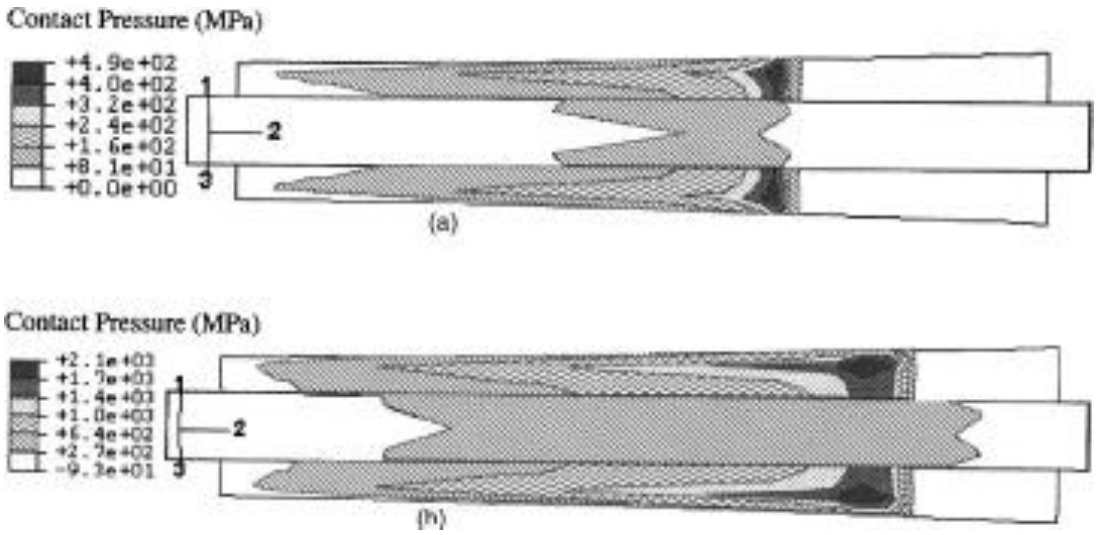

Figure 4-4. Contact Pressure Distribution (Al-Mayah et al. 2007).

To increase the sleeve-to-bar bond strength, there some other alternatives such as using swaged sleeves, resin-filled sleeves, and epoxy-bonded sleeves. Swaging is the process of gradually reducing the diameter of tubes or rods by radial hammering inside a dye. This is used to permanently attach the sleeve to the bar and provides clamping pressure to develop shear friction between the sleeve and bar. The clamping pressure, reduction in cross-sectional area, and

swaged length are the critical parameters directly affecting the anchorage's performance. Pincheira et al. (2005) investigated the performance of cold-swaged sleeves, resin-filled sleeves, and epoxy-bonded sleeves in tension and under displacement-control loading conditions. All specimens with epoxy-bonded sleeves failed due to bar pullout. Resin-filled sleeves were used on both smooth and deformed CFRP bars. The deformed CFRP bars featured 3.8-mm (0.15-in.) indentations spaced 13 mm (0.5 in.) along the bar, as shown in Figure 4-5. Two specimens had an indentation depth of 0.13 mm (0.005 in.), and one specimen had an indentation depth of 0.25 mm (0.1 in.). All resin-filled sleeves with smooth bars failed due to bar pullout. The resin-filled sleeves with deformed CFRP bars failed due to bar pullout and bar fracture regardless of the indentation size. The swaged sleeve was formed from a low-carbon stainless steel tube with an outer diameter of 9.5 mm (0.375 in.) and wall thickness of 1.2 mm (0.049 in.). The tube was swaged until the outer diameter was reduced to 8.6 mm (0.34 in.). The swaged length varied from 53 mm (2.1 in.) to 94 mm (3.7 in.). Swaged sleeves with conventional wedge anchorage failed due to either sleeve yielding or bar pullout. Swaged sleeves with a longer barrel and wedges failed due to bar fracture, which was the desired failure mode. Although the combination of swaged sleeves and a longer barrel proved to be successful, the major practical drawback is the implementation process, which is time consuming and also requires highly skilled workers. Furthermore, swaged sleeves are not reusable because the swaging process permanently attaches the sleeve to the bar.

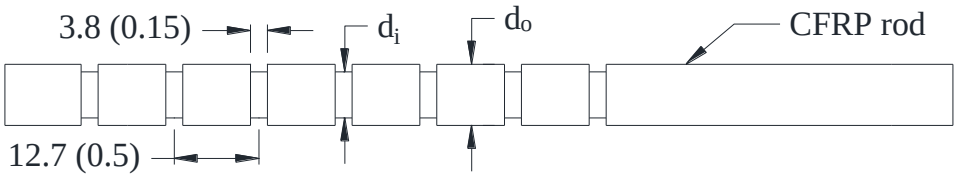

$(d_o + d_i)/2 = 0.127$ (0.005) (specimens RF1-D and RF2-D)
$= 0.254$ (0.010) (specimen RF3-D

Figure 4-5. CFRP Bar Indentations (Pincheira 2005).

The performance of the conventional anchorage with plastic wedges developed by the manufacturer for AFRP ARAPREE® bars has been recently investigated by Pirayeh Gar (2012). The conventional anchorage was tested using an MTS® testing machine with a monotonically applied load at the rate of 22 kN (5 kips) per minute according to ASTM 638. The applied load was recorded via a load cell connected to the MTS® machine, and the elongation of the specimen

was measured through strain gages mounted at the middle of the bar. The anchorage consisted of hard plastic wedges with a steel casing. All specimens failed in a brittle fashion near the anchorage location before reaching the ultimate stress, as shown in Figure 4-6. The failure stress for each specimen is presented in Table 4-1 and compared with the failure stresses observed in the uniaxial tests previously discussed in Chapter 3. This anchorage was also tested to investigate if the anchorage could sustain a prestressing load for a significant period of time. The anchorage was tested in an MTS® testing machine at a prestressing load equal to 55 percent of the ultimate capacity. After about 20 hours, the bar failed near the anchorage, similar to the failure shown in Figure 4-6. This implies that the anchorage was unable to sustain the prestressing load for a long period of time. For both tests, transverse stresses, caused by the hard plastic wedges, crushed the AFRP bar and caused premature failure since AFRP bars are weak in the transverse direction.

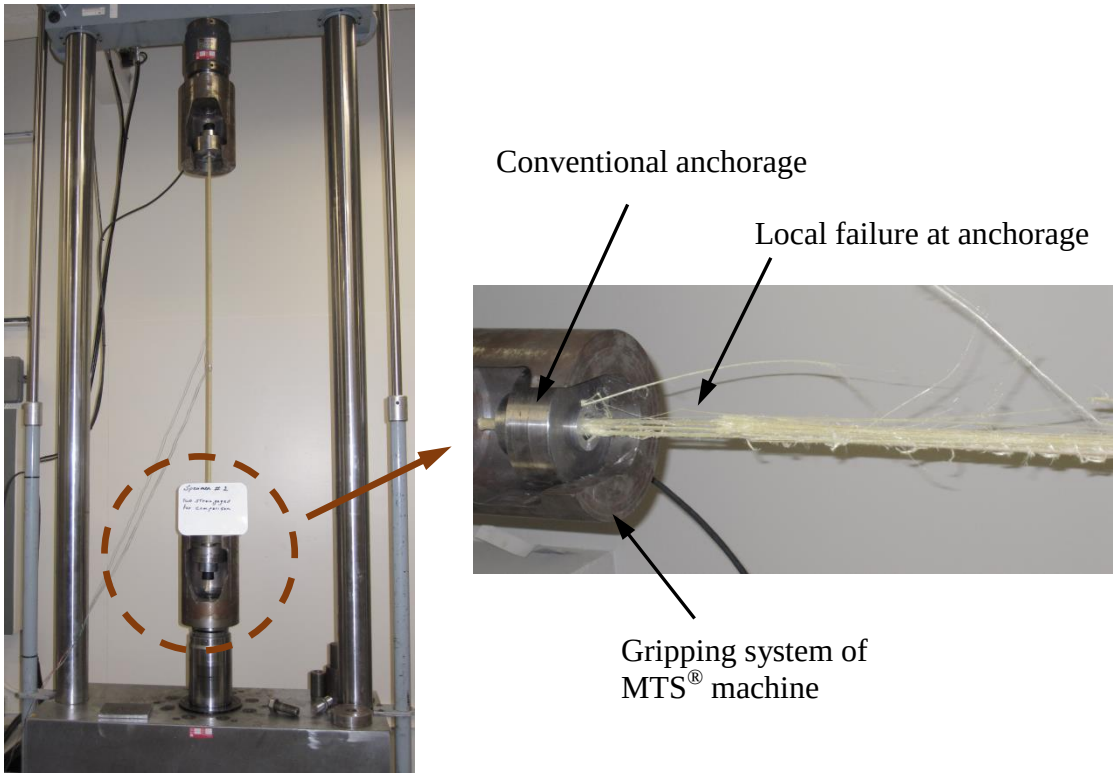

Figure 4-6. Failure of AFRP in Conventional Wedge Anchorage (Pirayeh Gar 2012).

Table 4-1. Comparison of Uniaxial and Conventional Anchorage Test Results (Pirayeh Gar 2012).

Conventional AFRP Anchorage Results		Uniaxial Test Results	
Specimen No.	Failure Stress (MPa [ksi])	Specimen No.	Ultimate Stress (MPa [ksi])
1	1030 (149.4)	1	1549.9 (224.8)
2	1010 (146.5)	2	1448.2 (210.0)
3	1006 (145.9)	3	1431.3 (207.6)
4	1058 (153.4)	4	1358.8 (197.1)
5	1015 (147.2)	5	1464.2 (212.4)
Mean	**1024 (148.5)**	6	1489.1 (216.0)
Standard Deviation (Unbiased Estimator)	**21**	Mean	**1457 (211.3)**
		Standard Deviation (Unbiased Estimator)	**63.4**

As discussed, the prestressing system using wedge-type anchorages benefits from their compactness, ease of assembly, and reusability. However, the main drawback of using wedge anchorages lies in the non-uniform transverse stresses induced by mechanical gripping, which triggers premature failure at the location of stress concentration. Using a sleeve as an intermediate part between the wedge and FRP bar to alleviate the stress concentration and to transfer the load in a more distributed manner could potentially weaken the bond strength. To compensate for the lack of bond strength, some solutions such as increasing the contact pressure, enlarging the contact area, and raising the friction coefficient between anchorages' components have been investigated by researchers, as previously discussed. Although some relative success can be seen in the experimental results, none of these options could be considered a reliable and practical anchorage for universal application. Using a wedge-type anchorage with a sleeve and enhanced bond strength does not offer a simple solution that can be broadly applied in the field for large-scale construction and may not be effective either cost-wise or time-wise. Furthermore, this type of anchorage might be very sensitive to the material type of the sleeve, bond length and

bond strength between the sleeve and FRP bar, contact pressure, and accuracy of assembling. Also, the sustainability of the anchorage needs to be investigated once the load capacity has proved to be sufficient.

4.2.2 Potted Anchorage Systems

A competitor to the wedge-type anchorage with a sleeve and enhanced bond strength, potted anchorage does not suffer from many of these drawbacks and hence has been widely investigated by researchers. Potted anchorages consist of an FRP bar embedded in a potting material that is confined by the walls of a casing. The potting material can vary from non-shrink cement to expansive grout. Potted anchorages grip the FPR by either bonding and interlocking the anchorage components, or generating circumferential pressure, depending on the potting material used. The effectiveness, therefore, is highly dependent on the geometry and bonded length of the anchorage (Zhang and Benmokrane 2004). Potted anchorages, particularly those using expansive grout, do not crush the FRP bar because the radial pressure is uniformly applied and independent of the prestressing load. Hence, the only major failure mode that needs to be designed against is pullout of the FRP from the potted anchorage.

There are basically two types of potted anchorages, a contoured sleeve and a straight sleeve. Contoured anchorages feature a tapered inner profile, such as conical or segmental, and have the ability to generate high radial pressure as the specimen is loaded (ACI 440R-04). The success of this anchorage is highly dependent on the internal geometry of the anchorage. The most common contoured anchorage uses a conical profile with a linear taper. Contoured sleeve anchorages are costly and difficult to manufacture, so straight sleeve anchorages are more widely accepted. Straight sleeve anchorages are easy to manufacture and have been used successfully in engineering practices (Zhang and Benmokrane 2004). Straight sleeve anchorages are also easier to design because the performance of the anchorage is mostly dependent on the bond length, geometry, and potting material.

There are two common types of potting material, resin and cementitious grout. The load transfer mechanism for resin relies on interlocking of the anchorage components. Resin has a high strength and fast curing time, but it is expensive and has the potential to deteriorate. Therefore, cementitious grout is more commonly used as the potting material in potted anchorages. The load transfer mechanism for cementitious grout is based on the circumferential

pressure generated by the expansive grout, which must fully fill the sleeve anchorage. The performance of the grout is largely dependent on the stiffness properties, moisture of curing, and degree of confinement of the grout (Bennitz and Schmidt 2012).

Straight sleeve anchorages were investigated by Zhang and Benmokrane (2004). Three different bond lengths—250 mm (9.8 in.), 300 mm (11.8 in.), and 500 mm (19.7 in.)—were tested on a 7.9-mm (0.311-in.) diameter CFRP Leadline® bar. The steel sleeve had a 35-mm (1.38-in.) outer diameter and 25.4-mm (1-in.) inner diameter with a serrated inner surface to increase the bond strength. A cementitious grout with a 28-day compressive strength of 70 MPa (10.2 ksi) was used in the straight sleeve anchorage. The experimental setup for the pullout tests is shown in Figure 4-7. The anchorage was tested in a universal testing machine with the load applied monotonically at a rate of 22 kN/min (5 kips/min). The results show that all specimens tested failed due to bar rupture, regardless of bond length. Therefore, a bond length of 250 mm (9.8 in.) is sufficient to reach the ultimate capacity of the CFRP bar. However, increasing the bond length improves the stiffness of the anchorage.

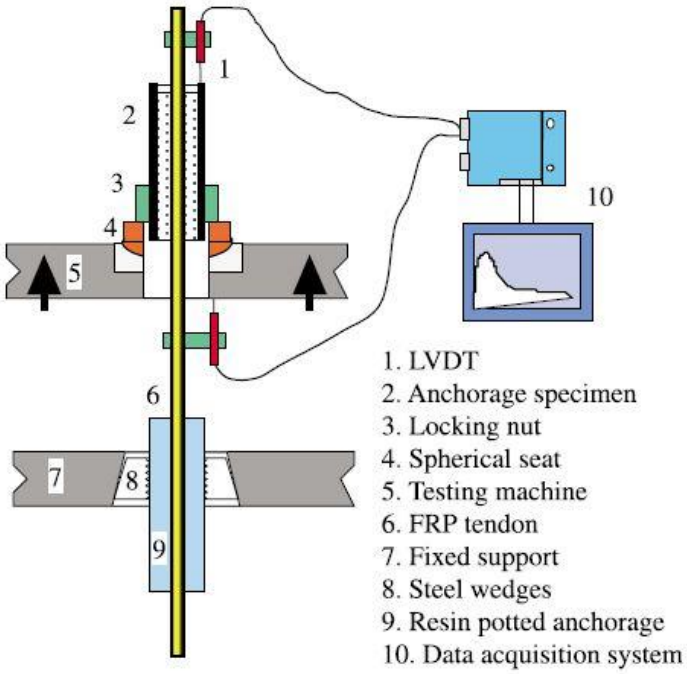

Figure 4-7. Tensile Test Setup (Zhang and Benmokrane 2004).

As previously discussed, Pirayeh Gar (2012) investigated the load capacity of a wedge-type anchorage developed by the manufacturer for AFRP ARAPREE® bars. This anchorage proved to

be insufficient because it caused premature failure of the AFRP bars because the hard plastic wedges crushed the AFRP bar. The wedge-type anchorage was also unable to sustain the prestressing load for a long period of time. Therefore, Pirayeh Gar (2012) developed a practical and reliable anchorage system for prestressing precast panels of FRP concrete bridge deck slabs. The anchorage system was composed of a steel pipe with a 457-mm (18-in.) length, 48-mm (1.9-in.) outer diameter, and 5-mm (0.2-in.) wall thickness filled with an expansive and quick-setting grout. The AFRP ARAPREE® bar was placed in the center of the pipe and held in place by plastic stoppers with central holes. The grout was poured through the first hole until the grout flushed the pipe's surface at the second hole to ensure that no air bubbles were present. Relaxation and creep tests were also performed using this anchorage. Recall the experimental setup shown in Figure 3-2. The pipe at the dead end was grouted first and left to set. The live end consisted of one pipe in front of and one behind the hydraulic jack. The front pipe was grouted, and then after 3 hours, the hydraulic jack was pumped to push the front pipe. The rear locking pipe was then injected with grout to lock the bar, and after 3 hours, the hydraulic jack was released. The anchorage was able to successfully prestress the AFRP bar up to 60 percent of the bar's ultimate capacity, and the anchorage was able to sustain the load without significant prestressing losses. This anchorage was used in the uniaxial tests discussed in Chapter 3, in which the anchorage was able to successfully reach the bar's ultimate stress.

Although this anchorage proved to be applicable and reliable, it is not suited for prestressing the AASHTO I-girder Type I. According to Pirayeh Gar (2012), the hydraulic jack was used to prestress the AFRP bar and was held in place while the locking pipe was grouted and then released after 3 hours once the grout had fully set. However, this is not a feasible solution for prestressing the girder because the prestressing bars are congested in the bottom flange and do not allow the hydraulic jack to be held in place. Therefore, another anchorage system is required.

Potted anchorages have been used in laboratory tests and engineering practices to successfully prestress FRP bars. Potted anchorages generally consist of an FRP bar embedded in a potting material inside a steel housing. The main drawback of potted anchorages is their long curing times, which make them impractical for use in the field. Cementitious grout is the recommended potting material because it is consistent, reliable, and less susceptible to deterioration when compared to resin. Cementitious grout transfers the prestressing load by

generating significant circumferential pressure on the bar due to the expansive properties of the grout. This circumferential pressure grips the FRP bar without crushing it. The performance of potted anchorages is strongly dependent on factors such as geometry and the potting material of the anchorage. Research shows that a straight sleeve anchorage with a 457-mm (18-in.) length, 48-mm (1.9-in.) outer diameter, and 5-mm (0.2-in.) wall thickness filled with an expansive and quick-setting grout is capable of prestressing 10-mm (0.393-in.) diameter AFRP ARAPREE® bars to ultimate capacity.

4.2.3 Research Summary

Two types of anchorage systems are commonly used to prestress FRP, wedge anchorages and potted anchorages. Wedge anchorages are composed of a number of wedges, a conical barrel, and an optional sleeve. The load transfer in a wedge anchorage is primarily through the interlocking of the components of the wedge anchorage. The most significant drawback to wedge anchorages is the fact that high stress concentrations tend to form at the loading end of the anchorage. Because FRP is weak in the transverse direction, stress concentrations often cause premature failure due to the wedges crushing the FPR bar. A sleeve can be added to the FRP bar to uniformly distribute the stress and protect the bar from premature failure. Much experimental research has been conducted on wedge anchorages, but a reliable universal wedge anchorage that can be used with all types of FRP has yet to be produced. Potted anchorages consist of an FRP bar embedded in a potting material that is confined by the walls of a housing (ACI 440R-04). Straight sleeve anchorages are preferred because they are simpler to design and manufacture. Cementitious grout is preferred over resin as the potting material because of its availability, low cost, and ease of preparation (Zhang and Benmokrane 2004). The load transfer mechanism for potted anchorages is based on the circumferential pressure that the grout generates. Because of this, the performance of potted anchorages is highly dependent on the geometry and potting material used. The most significant drawbacks to potted anchorage systems are their difficulty of assembly, long setting times, non-reusability, and the fact that if changes are made, the entire anchorage and bar assembly has to be replaced.

4.3 The Developed Prestressing Anchorage System

As discussed previously, a wedge-type anchorage system is not recommended due to the weakness of the AFRP bars in the transverse direction triggering premature failure. The anchorage developed by Pirayeh Gar (2012) was used to prestress AFRP bars for use in prestressed precast AFRP concrete bridge deck slabs. This anchorage system would not be appropriate for use in prestressing the AFRP bars in the AASHTO I-girder Type I because the bars are spaced too closely. Also, in order to use the anchorage system developed by Pirayeh Gar (2012), the AFRP bars would have to span the entire length of the prestressing bed, which would be uneconomical. Therefore, a new potted-type anchorage system was developed to prestress the bridge girder.

The initial design of the potted anchorage system is presented in Figure 4-8. The anchorage system was composed of a steel pipe with a 914-mm (36-in.) length, 48-mm (1.9-in.) outer diameter, and 5-mm (0.2-in.) wall thickness filled with an expansive and quick-setting grout. A 10-mm (0.394-in.) diameter AFRP bar and a 15-mm (0.6-in.) diameter steel strand were passed through the center of the pipe on either side and held in place by plastic stoppers, which had central holes. Styrofoam was placed in the center of the pipe to separate the grout and allow each side to be grouted individually. Surface holes were drilled in the pipe for injecting the grout. The grout was poured through the first hole until the grout flushed the pipe's surface at the second hole to ensure that no air bubbles were entrapped.

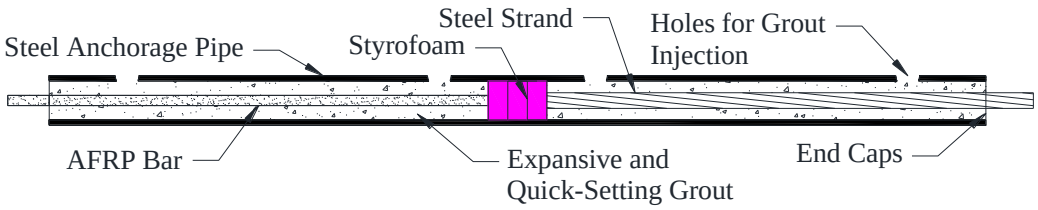

Figure 4-8. Initial Anchorage Design.

4.4 Anchorage Tests

As discussed in Chapter 2, the prestressing anchorage system should be able to sustain the target prestressing load of 60 percent of the bar's ultimate capacity without facing any major loss in prestressing force or premature failure. To verify the capacity and sustainability of the

anchorage, short-term and long-term tests were conducted, respectively. The experimental setup for the ultimate test is shown in Figure 4-9. Two steel angles were anchored to the strong floor at the High Bay Structural and Materials Testing Laboratory via 51-mm (2-in.) diameter threaded rods. The dead end was composed of a steel pipe with a 914-mm (36-in.) length, 48-mm (1.9-in.) outer diameter, and 5-mm (0.2-in.) wall thickness filled with an expansive and quick-setting grout. The AFRP bar was passed through the center of the pipe and held in place by a plastic stopper on one end. An internally threaded bushing was pot-welded inside the pipe on the other end, and a piece of Styrofoam was placed in front of the bushing to prevent the grout from leaking onto the threads. A steel plate with a central bolt was secured to the steel angle to accommodate the dead end. A center-hole jack pushing against a conventional wedge anchor was used to stress the system. A load cell was placed in front of the center-hole jack to measure the prestressing force, and LVDTs were placed at each of the strand-anchorage interfaces to measure the slip of the bars inside the anchorage. The hydraulic center-hole jack was pumped manually in a slow, smooth fashion until failure occurred somewhere in the system. For the load capacity tests, AFRP rupture outside the anchorage zone is the desired failure mode because it indicates that the anchorage load capacity is not less than the bar's ultimate capacity.

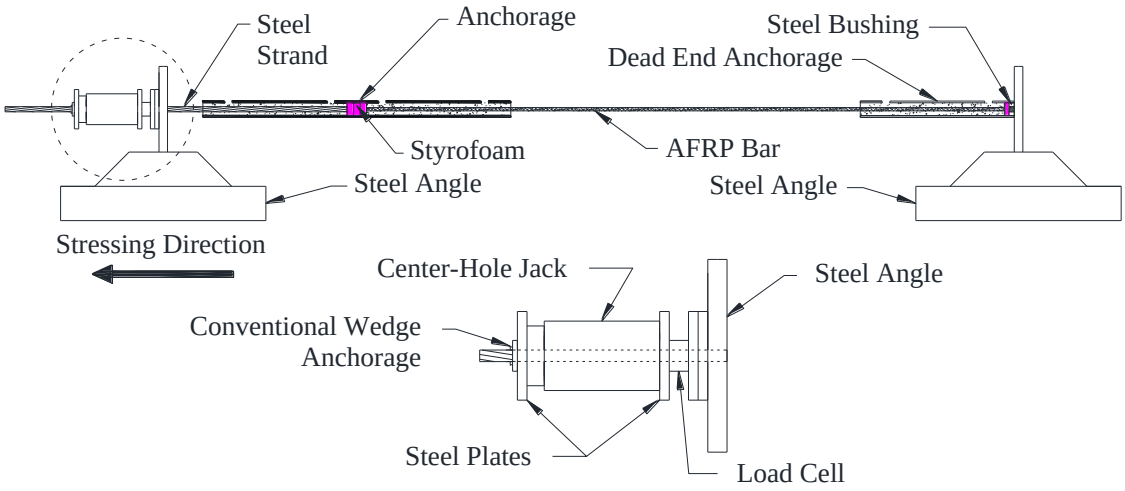

Figure 4-9. Ultimate Test Experimental Setup.

4.5 The Load Capacity Tests

Two specimens using the initial anchorage design were tested in tension until failure. In both cases, the test was terminated due to grout pullout at the steel end of the anchorage and the dead

end, respectively. An example of grout pullout failure is shown in Figure 4-11. Both failures were premature, occurring at about 42 and 50 percent of the bar's ultimate capacity, respectively. Grout pullout failure suggests that the bond between the grout and the anchorage pipe was insufficient. Further investigation after the test revealed an oily residue on the surface of the grout that had been pulled out from the anchorage. A third specimen was tested using anchorage pipes that had been cleaned thoroughly. The dimensions and instrumentation were identical to the previous test. The test was terminated due to grout pullout at the steel end at a prestressing load of about 54 kN (12 kips), corresponding to 50 percent of the bar's ultimate capacity. Figure 4-11 presents the results of the ultimate test of the initial anchorage design. As seen, the load drops significantly any time the grout slips.

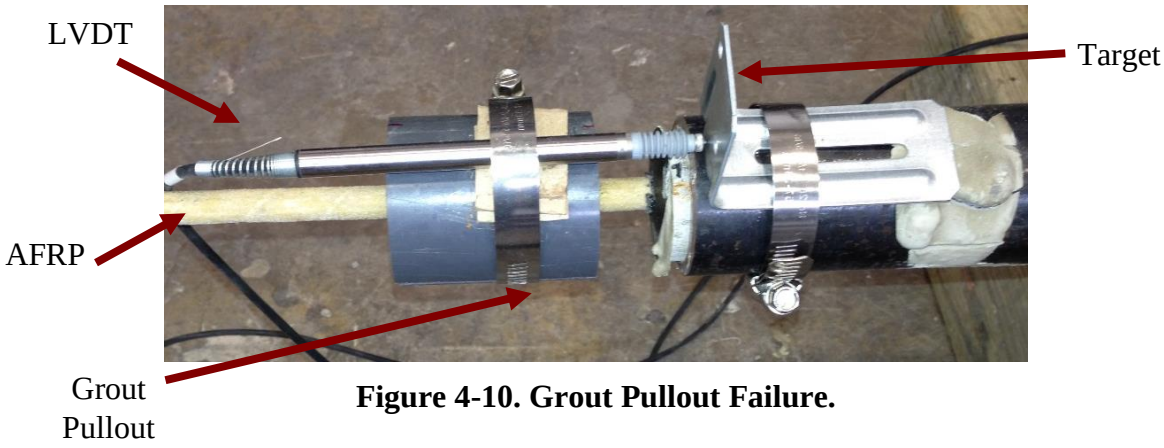

Figure 4-10. Grout Pullout Failure.

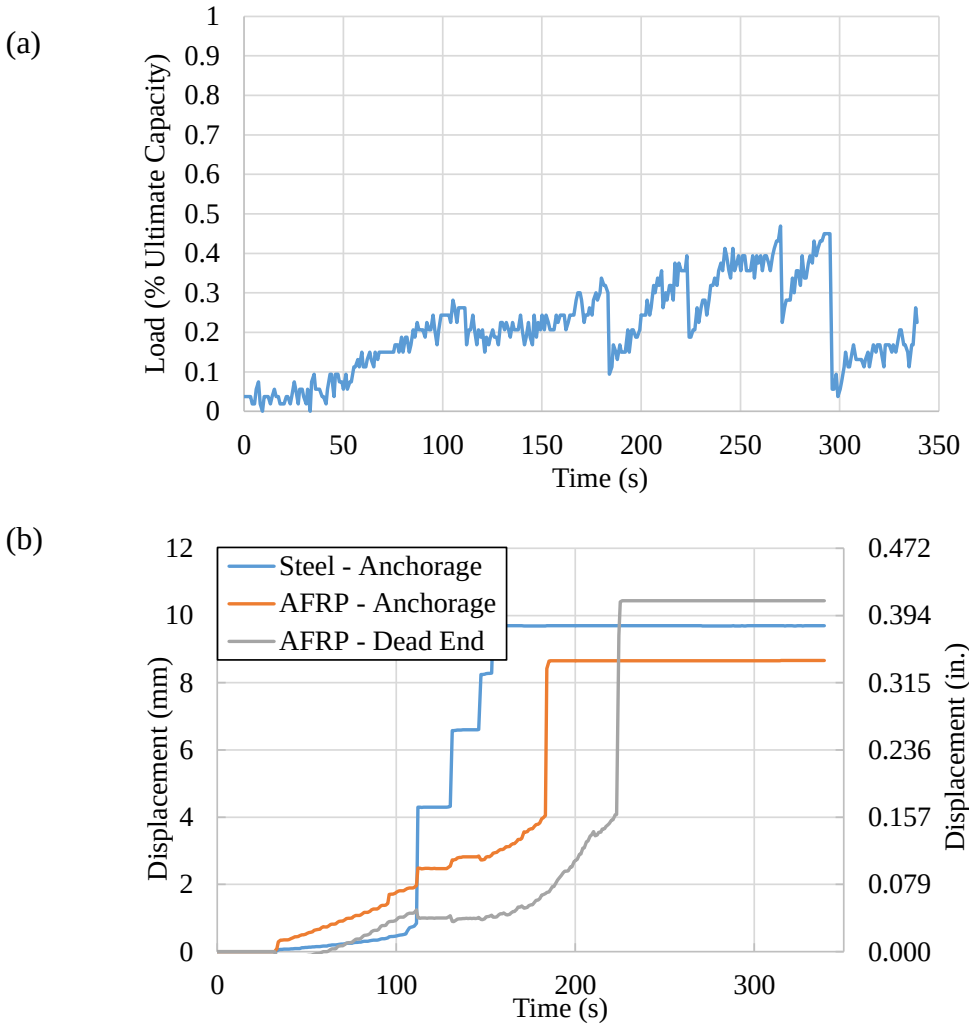

Figure 4-11. Ultimate Test Results of Initial Anchorage Design: (a) Load Capacity and (b) Anchorage Slip.

In order to increase the bond between the grout and the anchorage pipe, the anchorage pipes were crimped as shown in Figure 4-12 to add a mechanical feature. The pipes were crimped using an MTS® machine set to a specific displacement. A 12.7-mm (0.5-in.) deformation was placed every 50.8 mm (2 in.) along the length of the pipe, with a 90° rotation in between crimps. The new crimped anchorage system was tested in tension until failure. The test was terminated due to AFRP pullout at the dead end at a load approximately equal to the bar's ultimate capacity. The results of the ultimate test using the crimped anchorage system are presented in Figure 4-13. As shown, minimal slip was seen in the anchorage system before failure. Although the crimped anchorage system was able to resist a high prestressing load, the desired failure mode was not present. Bar pullout suggests that the bond strength between the grout and the bar was

insufficient. Therefore, the test was repeated to see if the results would be similar. In this test, the anchorage failed due to AFRP pullout at the anchorage location at a load approximately equal to 45 kN (10 kips), corresponding to 42 percent of the bar's ultimate capacity. In all tests, there was a significant amount of torsion occurring in the system. This torsion was likely caused by the steel prestressing strand attempting to unwind as it was pre-tensioned. The presence of torsion could have caused the system to fail prematurely. Although the first test of the crimped anchorage system was a success, the second test suggested that the anchorage was unreliable and should be redesigned.

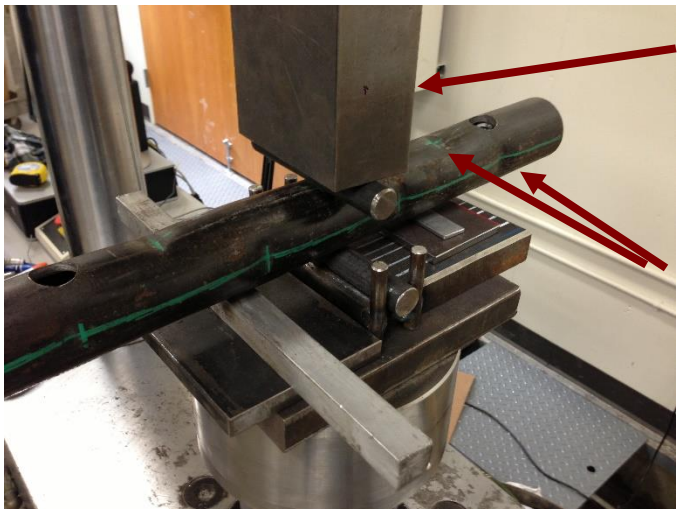

Figure 4-12. Crimped Anchorage Pipe.

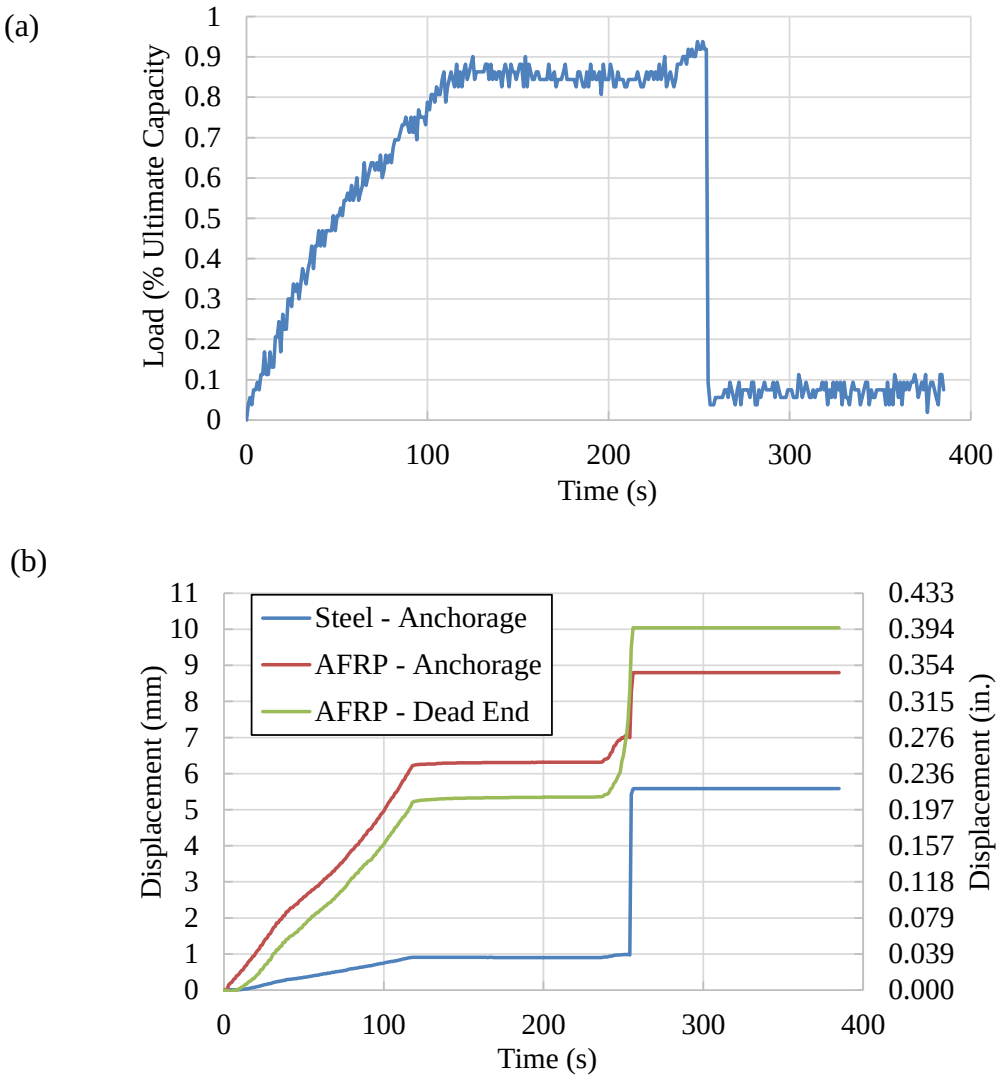

Figure 4-13. Ultimate Test Results of Crimped Anchorage System: (a) Load Capacity and (b) Anchorage Slip.

To find out if the torsion was really causing the anchorage to fail prematurely, the steel strand was removed from the system, and two tensile tests of AFRP ARAPREE® bars were performed using the same potted anchorage pipe. Two steel pipes were used as anchorages having a 457-mm (18-in.) length, 48-mm (1.9-in.) outer diameter, and 5-mm (0.2-in.) wall thickness filled with an expansive and quick-setting grout. A 10-mm (0.394-in.) diameter AFRP ARAPREE® bar with a 1420-mm (56-in.) length was passed through the center of the pipes and held in place by plastic stoppers that had a central hole. The specimen was gripped by the jaws of the MTS® machine, as shown in Figure 4-14, and the load was applied at a constant rate of 22 kN (5 kips) per minute, according to ASTM 638. Both specimens failed in a sudden fashion due

to bar pullout at 78 kN (17.6 kips) and 81 kN (18.2 kips), respectively. Displacements for the tensile tests are shown in Figure 4-15. No slip was seen before the specimen failed due to bar pullout, which implied that the bond between the grout and the bar was insufficient regardless of any torsional effect. However, in both tests the load at failure was higher than that of the load capacity tests, confirming that torsion did not help to increase the strength of the anchorage.

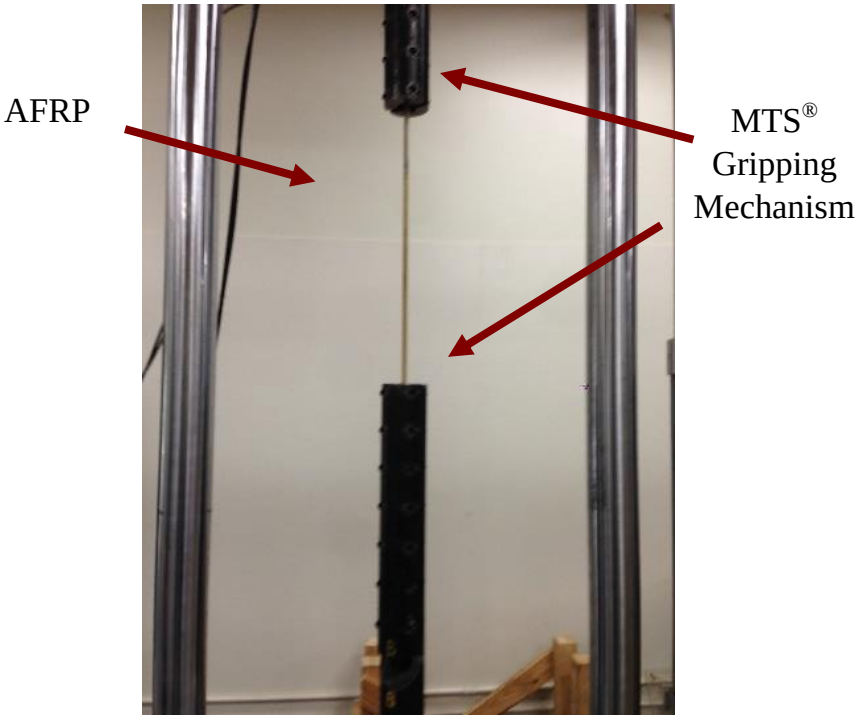

Figure 4-14. Tensile Test Setup.

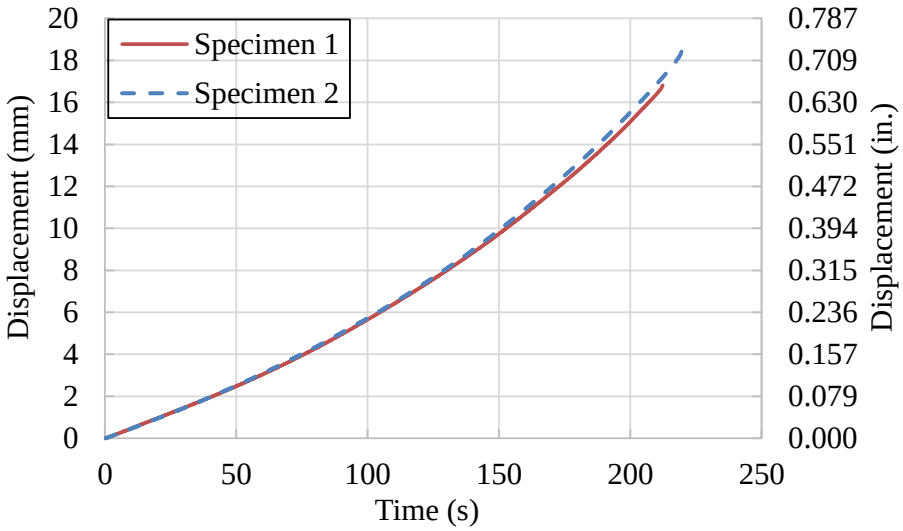

Figure 4-15. Tensile Test Displacement.

The anchorage was redesigned to remove any torsional effect and also to increase the bond strength between the bar and the grout. The 15-mm (0.6-in.) diameter steel strand was replaced with a 14.3-mm (0.563-in.) diameter threaded rod with a minimum tensile strength of 860 MPa (25 ksi) to remove any torsional effects. Furthermore, the grout length was extended to 916 mm (36 in.) at the dead end and 610 mm (24 in.) at the AFRP end of the anchorage, and decreased to only 203 mm (8 in.) at the steel end of the anchorage to enhance the bond strength between the AFRP bar and the grout. The plastic stoppers were replaced with 25.4-mm (1-in.) steel bushings with a central hole pot-welded inside the pipe to prevent grout pullout failure. This pot-welded steel bushing also created a compressive stress on the grout, which increased the tensile capacity of the grout. A long-term test was carried out on the anchorage. The experimental setup for the long-term test is shown in Figure 4-16. The conventional wedge anchorage behind the hydraulic jack was replaced with a steel plate, a washer, and a high-strength nut. A high-strength locking nut was added to hold the load once the desired prestressing load was reached. A steel pipe with a surface hole was placed in front of the jack to adjust and set the locking nut. Once the prestressing load was reached, the locking nut was tightened to sustain the load, and the hydraulic jack was released. The data acquisition system recorded data every 5 minutes for 3 days. A load cell was placed in front of the center-hole jack to measure the prestressing force, and LVDTs were placed at each of the strand-anchorage interfaces to measure the slip of the bars inside the anchorage. The slips inside anchorage components are presented in Figure 4-17. The anchorage was able to sustain the prestressing load with minimal slip for about 50 hours. After 50 hours, significant slip was seen at the AFRP end of the anchorage. Minimal to no slip was seen at the dead end, however. Considering that the grout length at the dead end was 306 mm (8 in.) longer than at the anchorage, a 916-mm (36-in.) grout length at the anchorage should be able to sustain the desired prestressing load with minimal to no slip.

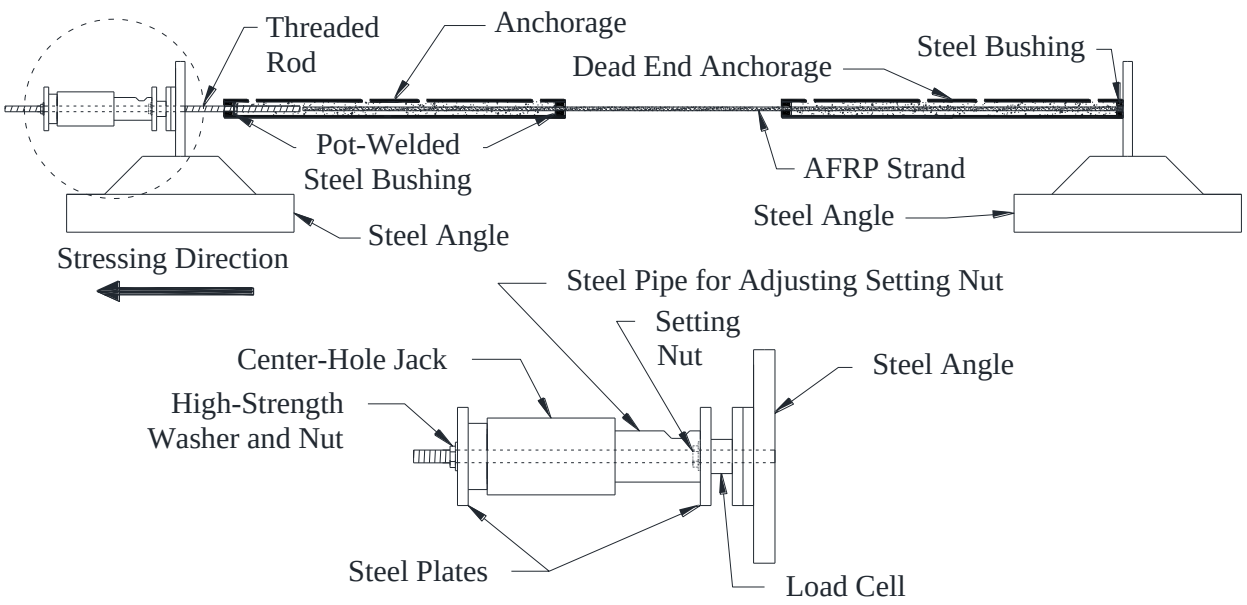

Figure 4-16. Long-Term Test Setup.

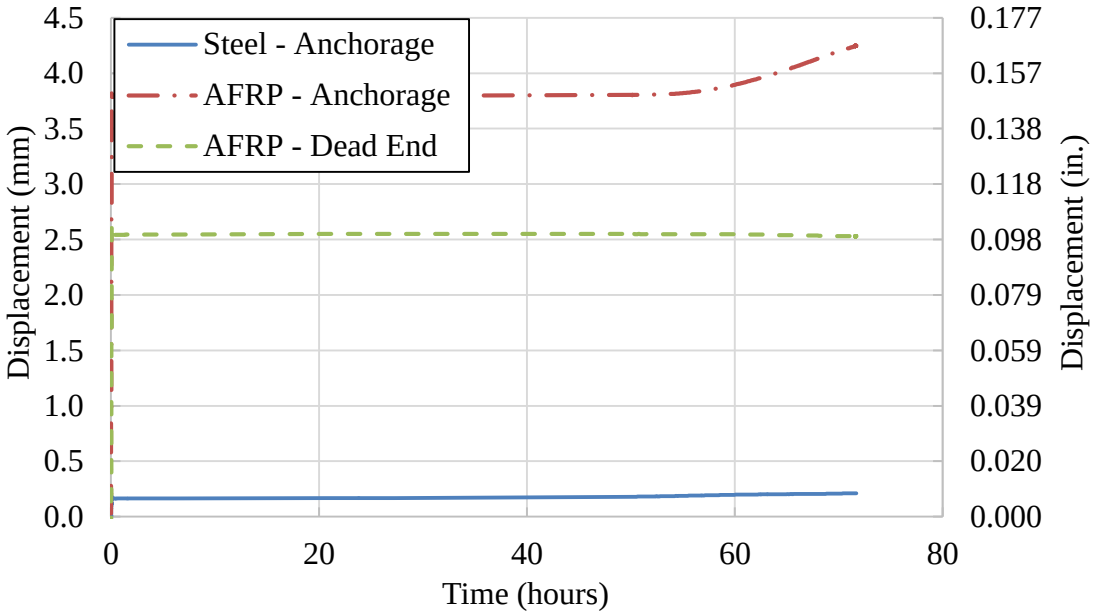

Figure 4-17. Long-Term Anchorage Slip.

The anchorage was eventually redesigned to prevent slip at every location on the anchorage. The grout length was extended to 916 mm (36 in.) at the dead end and the AFRP end of the anchorage, and was removed at the steel end of the anchorage to increase the bond strength between the AFRP bar and the grout. The steel end of the anchorage consisted of a high-strength washer and nut on the threaded rod that was bearing on the pot-welded steel bushing inside the

pipe. The final anchorage was tested using a procedure identical to the previous long-term test. The results of the final anchorage test are shown in Figure 4-18. The anchorage proved to be reliable by sustaining the desired prestressing load for 3 days with minimal to no slip. The final anchorage design is presented in Figure 4-19.

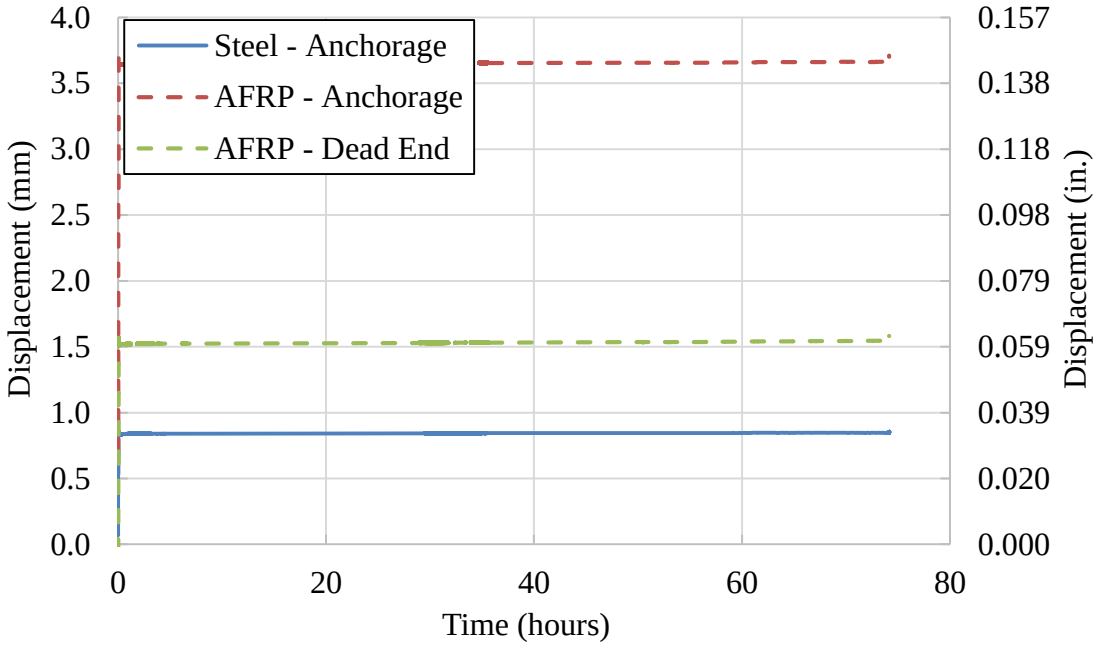

Figure 4-18. Long-Term Slip of Final Anchorage Design.

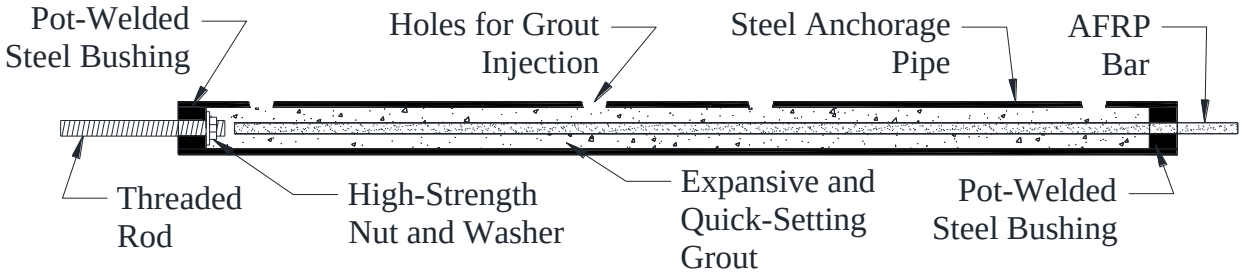

Figure 4-19. Final Anchorage Design.

5 CONSTRUCTION PROCESS

5.1 Introduction

Construction of the AFRP concrete AASHTO I-girder Type I took place over a span of 6 days at a prestressing plant in San Marcos, Texas. The weather was in the high 90s to low 100s for all six days. The special anchorage, as discussed in Chapter 4, was used to pretension all 24 prestressed AFRP bars. Steel side forms in the shape of the AASHTO I-girder Type I and wooden end forms were placed to confine the concrete. Once the girder was constructed, it was transported to a separate prestressing bed, and the formwork for the deck was built around the existing girder. The deck was longitudinally and transversely reinforced with conventional steel rebar. Once the AASHTO I-girder Type I with the topping deck was constructed as a composite section, it was transported to the High Bay Structural and Materials Testing Laboratory on the campus of Texas A&M University for further testing. This chapter discusses the construction process of the AASHTO I-girder Type I composite with the topping deck and points out the construction advantages and issues.

5.2 Girder Reinforcement

As discussed in Chapter 2, the cross section of the AASHTO I-girder Type I is composed of self-consolidating concrete reinforced with both prestressed AFRP and non-prestressed AFRP bars having a 10-mm (0.393-in.) diameter. The dimensions and longitudinal reinforcement layout are shown in Figure 2-3. Twenty-four prestressed AFRP bars were used within the girder section: 22 in the bottom flange and two in the top flange. The two prestressed AFRP bars in the top flange of the girder were attached to the stressing bed using steel extension plates, as shown in Figure 5-1. The extension plates were connected to the stressing bed using a 14.3-mm (0.563-in.) diameter threaded rod and high-strength nuts and washers. Eight non-prestressed AFRP bars were used within the girder section: six in the web and two in the top flange. The non-prestressed bars were placed with the aid of the wooden end form, which will be discussed later.

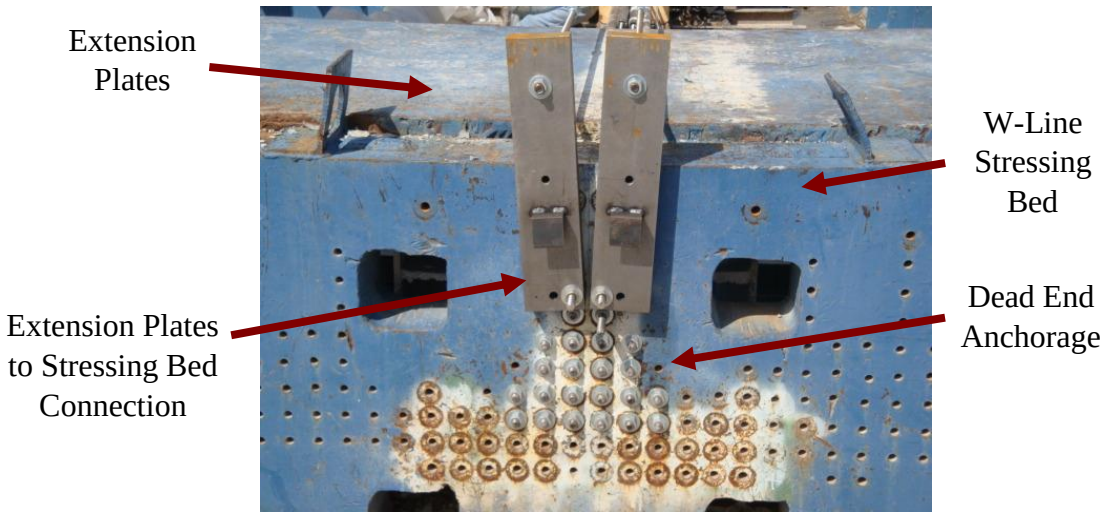

Figure 5-1. Steel Extension Plates.

The shear reinforcement layout is presented in Figure 2-3 and Figure 2-4. R-shape AFRP ARAPREE® bars of a 10-mm (0.393-in.) diameter formed the shear reinforcement. Steel shear bolts with a 381-mm (15-in.) length were added at the deck/girder interface to provide additional shear resistance against the horizontal shear force developed at the deck/girder interface through the composite action. All shear reinforcement was attached to the longitudinal reinforcement with conventional steel rebar ties. The process of placing the shear and non-prestressed longitudinal reinforcement was convenient and quick due to the light weight of the AFRP bars.

5.3 AFRP Bar-Bending Procedure

The R-shape stirrups were bent out of the straight AFRP bars at Texas A&M University using the bending process previously investigated by Pirayeh Gar (2012). The bending process is shown in Figure 5-2 and includes heating the bar with a heat gun to somewhat soften the resin matrix and then pressing the bar using a rubber mallet and a mediator plate to avoid damaging the fibers. The bars are eventually bent around the bending apparatus and are kept in their final bent position as the resin very quickly cools off.

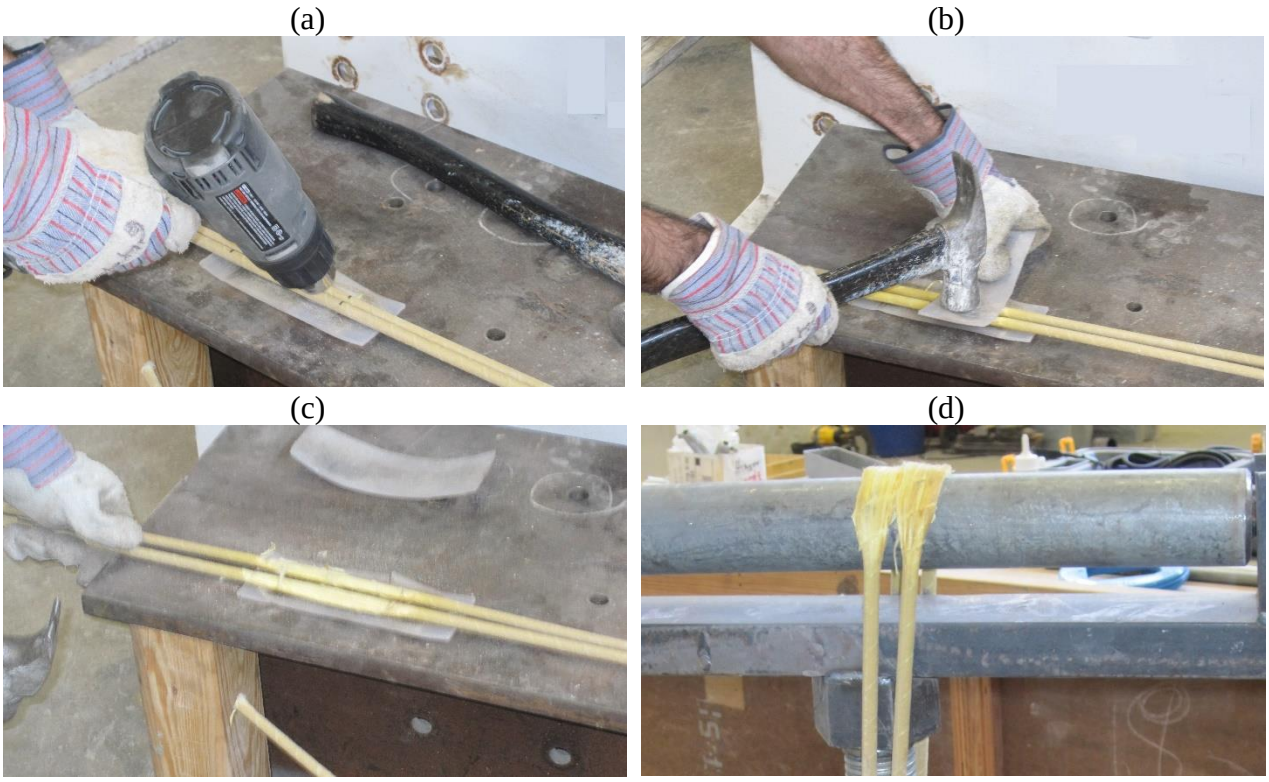

Figure 5-2. AFRP Bar-Bending Process: (a) Heating the Bar with a Heat Gun, (b) Pressing the Bar, (c) Viewing the Softened Resin Matrix, and (d) Bending the Bars (Pirayeh Gar 2012).

5.4 Deck Reinforcement

Conventional steel rebar was placed within the topping deck to reinforce the slab either longitudinally or transversely. AFRP reinforcement was not used in the topping deck because the deck was built only to provide a composite action with the girder. The longitudinal reinforcement was composed of two D16 (#5) rebar bisecting the center, six D13 (#4) rebar spaced at 203 mm (8 in.) apart in the bottom, and nine D13 (#4) rebar spaced at 178 mm (7 in.) centered in the top. The transverse reinforcement was composed of sixty D13 (#4) rebar placed 203 mm (8 in.) apart on the top and bottom. The deck reinforcement detail is shown in Figure 2-5.

5.5 Prestressing Operation

The AASHTO I-girder Type I, with composite deck, was constructed using a 24-m (79-ft.) long W-line stressing bed at a prestressing plant in San Marcos Texas. The 16.75-m (55-ft.)

AFRP bars were pre-tensioned using the anchorage system as discussed in Chapter 4. The prestressing anchorage consisted of a 914-mm (36-in.) long steel pipe filled with an expansive and quick-setting grout and is shown in Figure 4-19. The AFRP bar was passed through the length of the pipe and held in the center by a steel bushing pot-welded inside the pipe with a central hole. A 14.3-mm (0.563-in.) diameter threaded rod was fastened at the opposite end of the pipe with a high-strength nut and washer bearing on a pot-welded steel bushing. The anchorage at the dead end for each AFRP bar was grouted at Texas A&M University and transported to the prestressing plant.

The threaded rods at the dead ends were passed through the holes in the stressing bed and anchored with high-strength washers and nuts. The AFRP bars were then passed through the holes of two wooden formworks shaped as the cross section of the AASHTO I-girder Type I. The anchorages at the live end were then grouted and left to set before the bars were pre-tensioned. Once the live end anchorages were set, the threaded rod at the live end was passed through the holes in the stressing bed and secured with a setting nut and washer. The live end of the prestressing system is shown in Figure 5-3 and Figure 5-4. A hydraulic center-hole jack was used to pre-tension AFRP bars individually, where the prestressing load was monitored through the pressure from the hydraulic jack. The steel pipe had a surface hole to allow the setting nut to be adjusted as the bar was pre-tensioned. The hydraulic jack pushed against a steel plate held in place by a high-strength nut and washer to stress the AFRP bar. The threaded rod at the live end was extended via a coupling nut and another section of threaded rod. As the hydraulic jack was extended, the setting nut in front of the coupling nut was tightened periodically with a screwdriver to hold the prestressing load. This process was repeated for each AFRP bar in the girder's cross section. Each bar required about 10 minutes to be prestressed. Due to some failures that occurred, as will be discussed, the entire prestressing operation lasted approximately 6 hours.

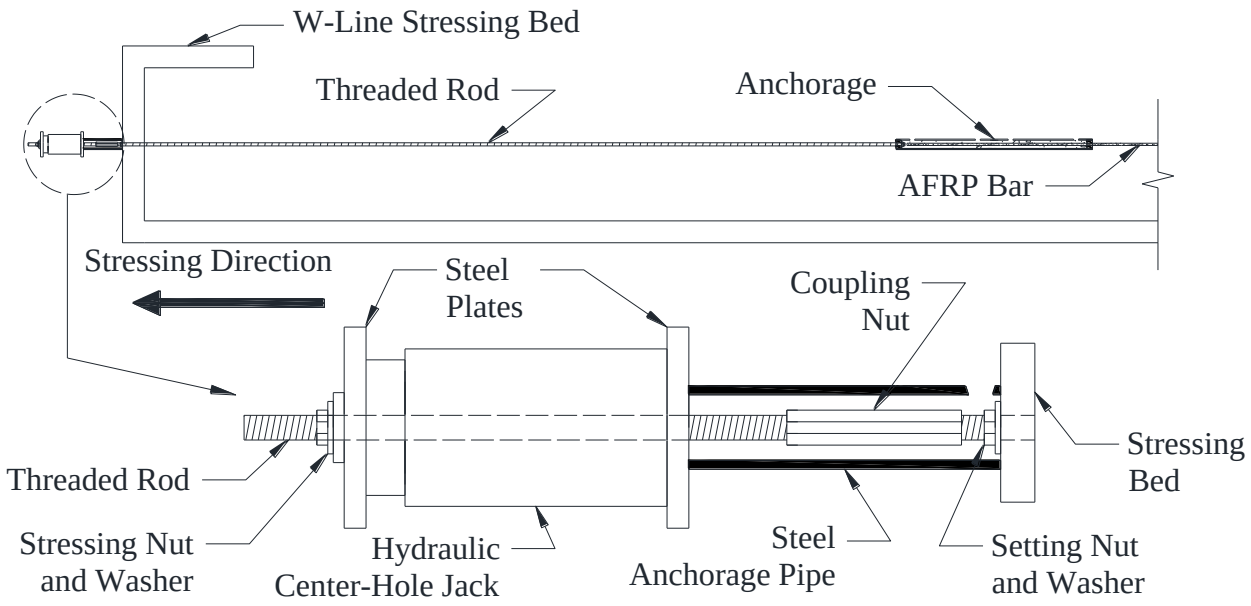

Figure 5-3. Stressing End Detail.

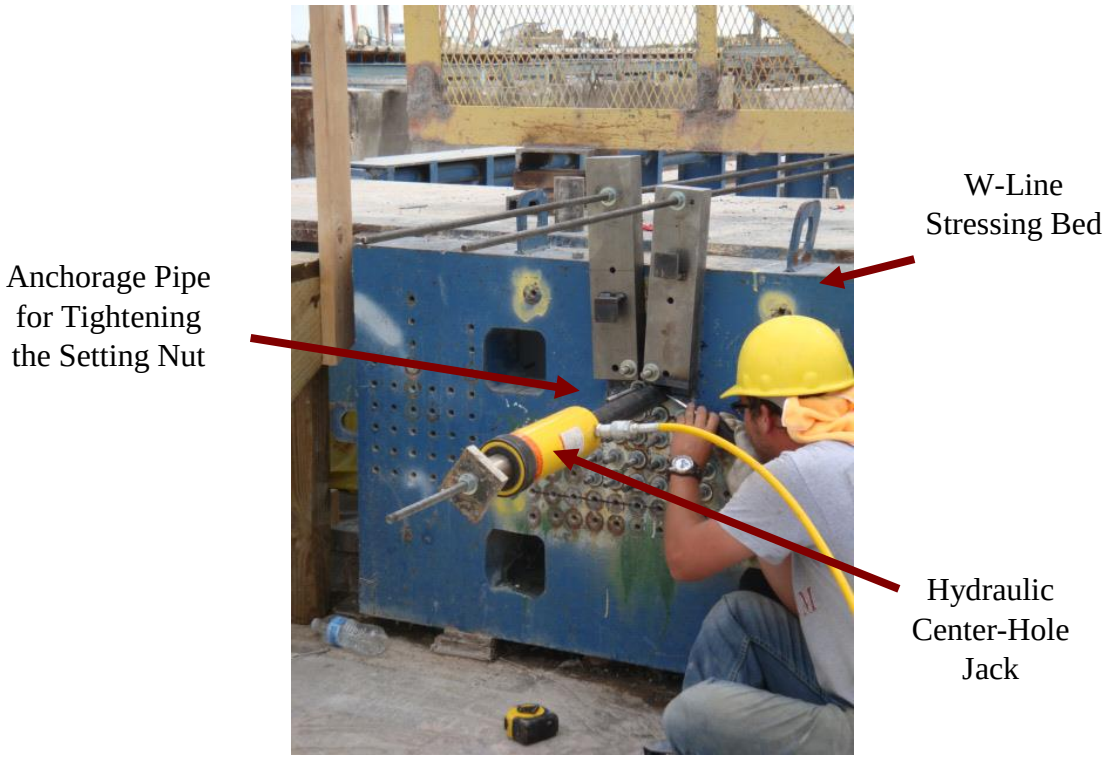

Figure 5-4. Prestressing Setup—Live End.

Once all of the AFRP bars were pre-tensioned, the wooden end forms were placed to create a girder with a 12.2-m (40-ft.) length. The non-prestressed AFRP bars were cut to the target length, placed in the proper position, and held in place by the wooden end form. Once all of the

longitudinal reinforcement was in place, the shear reinforcement was placed and tied to the AFRP bars using conventional steel rebar ties. Form oil was applied to the steel formwork and wooden end forms for the AASHTO I-girder Type I and placed using a Mi-Jack crane. The formwork and reinforcement of the girder are presented in Figure 5-5. Steel brackets were used at the top and bottom of the steel forms to keep the forms in place while the concrete was poured. Two lifting points made of steel strands were placed at 2.5 m (8 ft.) from each end to transport the girder.

Figure 5-5. Girder Formwork and Reinforcement.

5.6 Concrete Placement

The concrete for the girder was poured using one batch of self-consolidating concrete and left to cure for 3 days. Before the concrete was poured, a sample was taken in order to determine the fresh characteristics of the concrete including slump, unit weight, and concrete strength tests, as discussed in Chapter 3. The target 28-day strength of concrete was about 69 MPa (10 ksi). The falling height of the concrete did not exceed 1.5 m (5 ft.) at any time during the pour. Self-consolidating concrete does not require vibration; however, the steel side forms were vibrated in order to remove any unwanted air bubbles. The concrete itself was not vibrated to avoid possible damage to the AFRP bars. Once the concrete for the girder was poured, the top surface of the girder was roughened using a steel brush to provide more shear interlocks at the deck/girder interface. The concrete was covered with burlap, and moisture was added using a mechanical soaker for the duration of the curing period. Figure 5-6 shows the casted concrete girder.

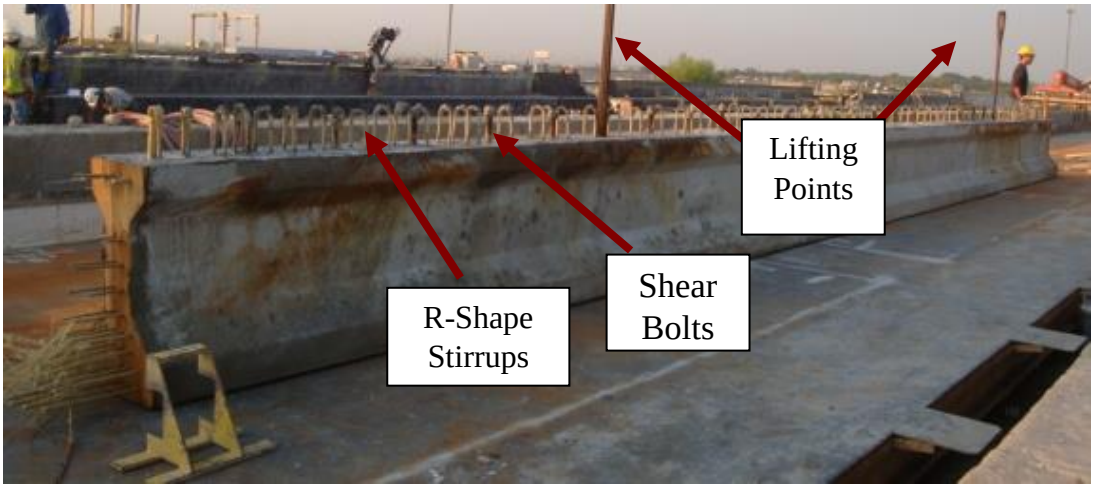

Figure 5-6. AFRP-Reinforced AASHTO Type-I Bridge Girder.

After 3 days of concrete curing, compressive strength tests showed a concrete strength of 55 MPa (8 ksi). The AFRP bars were then cut with a hacksaw, and the specimen was transported to a separate stressing bed to build the formwork for the deck. A plywood platform was built up around the girder and used as the bottom formwork for the topping deck. Prefabricated wooden forms were then secured to the plywood platform to create a 203-mm (8-in.) high formwork for the sides of the deck. The formwork was coated with form oil, and the conventional steel reinforcement for the deck was placed. The formwork and steel reinforcement for the deck are shown in Figure 5-7.

The concrete for the topping deck was poured using two batches of self-consolidating concrete and left to cure overnight before the formwork was removed. Before each batch was poured, a sample was taken to determine the fresh characteristics of the concrete. As discussed in Chapter 3, the target 28-day strength of concrete was about 69 MPa (10 ksi). The falling height of the concrete did not exceed 1.5 m (5 ft.) at any time during the pour. The concrete was vibrated using a mechanical vibrator to ensure no unwanted air bubbles were present. The top surface of the deck was finished with a concrete float to create a smooth surface. The concrete was covered with burlap, and moisture was added using a mechanical soaker for the duration of the curing period. After 1 day of curing, the concrete reached a strength approximately equal to 34.5 MPa (5 ksi), and hence the formwork was removed. The AASHTO I-girder Type I with composite deck is presented in Figure 5-8.

Figure 5-7. Deck Formwork and Reinforcement.

Figure 5-8. AFRP-Reinforced AASHTO I-Girder Type I with Composite Deck.

5.7 Constructability Issues

The original prestressing plan required each AFRP bar to be prestressed up to 54 percent of the AFRP bar's ultimate capacity. During the prestressing process, three AFRP bars failed due to AFRP rupture outside of the anchorage. These bars were replaced, re-grouted, and pre-tensioned up to 40 percent of ultimate capacity successfully except one, which was prestressed up to only 24 percent of ultimate capacity. Therefore, to reduce the risk of further failures, the remaining AFRP bars were all similarly pre-tensioned to 40 percent of the ultimate capacity. The final prestressing load for each AFRP bar is presented in Figure 5-9.

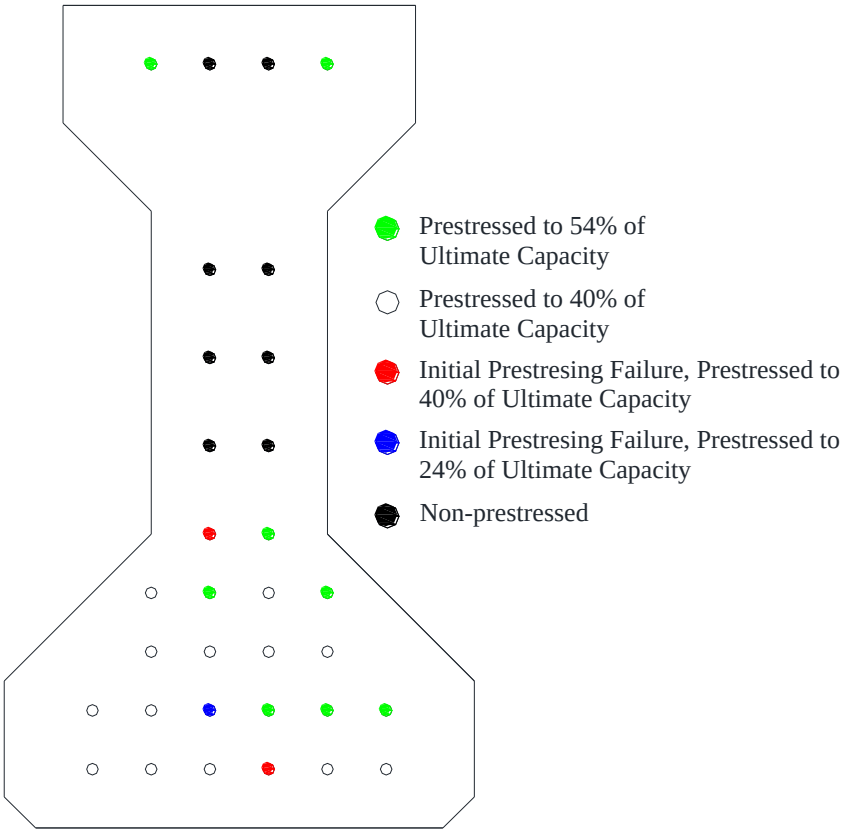

Figure 5-9. Individual Prestressing Loads.

Due to the intense heat, complications arose during the grouting process. The water used for mixing the grout was too hot, which caused the grout to set extremely quickly. Because of this, grouting was delayed until very early the next morning when the outside temperature was more reasonable. The authors recommend to use ice water during the grouting process when the outside temperature is very high to avoid premature setting of the grout.

5.8 Conclusion

The process of placing the shear and non-prestressed longitudinal reinforcement was convenient and quick due to the light weight of the AFRP bars. One person could easily carry and place the bars without assistance from heavy machinery. This is the main advantage of AFRP bars for construction compared to conventional steel rebar. The transportation of reinforcement alone can be costly and time consuming when constructing large structural members reinforced with conventional steel reinforcement. The light weight of AFRP provided ease of placement in the field and lower transportation costs. Furthermore, any possible

replacement of reinforcement due to future repair and rehabilitation plans will cause shorter downtime compared to conventional reinforcement.

Also, once the AFRP bars are bent, the shape can be easily adjusted to fit the need. For example, if the angles of the bends for the top and bottom bars are not exactly correct, they can be adjusted by hand to fit into the cross section of the girder. This is not an option with conventional steel reinforcement.

The construction process took place over a span of 6 days. The main constructability issue was the premature failure that occurred for some of the AFRP bars during the prestressing operation. A few of the prestressed AFRP bars failed during the pre-tensioning process due to AFRP rupture outside of the anchorage. This suggests that the anchorage itself had a sufficient grip on the bar, but the capacity of the AFRP bar was exceeded. This failure could be attributed to either inconsistencies in the material properties or damage during transportation. The prestressing operation required the majority of the time to be spent manufacturing the girder. A large component of this time was the fact that the potted anchorages at the live end required on-site manufacturing. Prefabrication of the potted anchorages at both ends of the prestressed AFRP bars would have dramatically shortened the construction schedule.

6 EXPERIMENTAL RESULTS

6.1 Introduction

This chapter discusses the experimental performance of the AASHTO I-girder Type I in both flexure and shear tests. The specimen was tested in flexure and shear at the High Bay Structural and Materials Testing Laboratory on the campus of Texas A&M University. The main focus of the flexure test was on the load and deformation capacities, moment-curvature relationship, failure mode, and crack patterns. Furthermore, the experimental deflection profile and curvature distribution along the girder were also studied to better understand the global response of the girder at post-cracking levels of loading. The numerical analysis of the flexural behavior was conducted and compared with experimental results. After the flexure test, two shear tests were conducted at both uncracked ends of the girder to measure the shear capacity, failure mode, and crack patterns, and to verify the embedment length. Finally, all the experimental results were compared with the control specimen reinforced with conventional steel rebar and prestressing strands.

6.2 Flexure Test

The flexure test was conducted under a four-point configuration of loading, which was increased monotonically until flexural failure. The flexure test setup is illustrated in Chapter 2. A 2700-kN (600-kips) actuator, which was attached to the steel loading frame, was used to apply load on the specimen. The load points were spaced 914 mm (36 in.) apart and provided a constant moment region at the midspan of the specimen. The specimen was manually loaded under displacement control at a rate approximately equal to 44 kN (10 kips) per minute before first cracking at the midspan, and then load was decreased to 22 kN (5 kips) per minute. The load was halted periodically to record and mark the flexural cracks.

6.2.1 Load and Deformation Capacity

Figure 6-1 presents the experimental and analytical moment-curvature graphs. As expected, the moment-curvature response seems to be linear before and after cracking. The cracking moment and the moment capacity are respectively equal to M_{cr} = 542.3 kNm (400 kft.) and M_n = 1563.2 kNm (1153 kft.). If the dead load of the girder and slab is deducted from the service

load calculated in Chapter 2, 841 kNm (620 kft.), the share of live load and dead loads of barrier and future wearing will be equal to 611 kNm (450 kft.), which is greater than the cracking moment, 542.3 kNm (400 kft.). Hence, the girder is categorized as a partially prestressed beam.

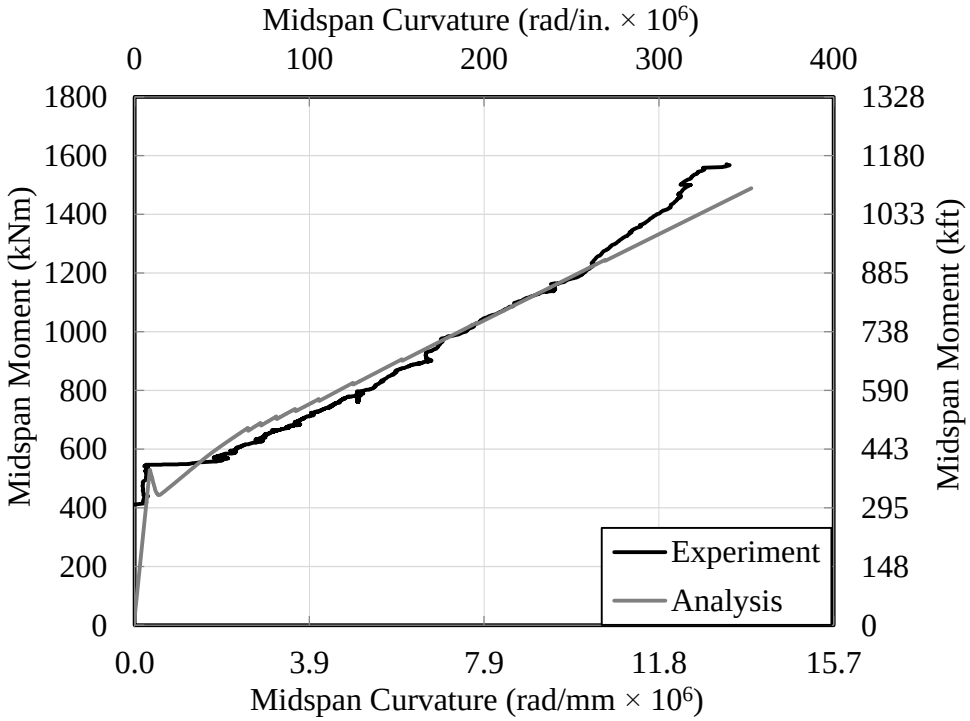

Figure 6-1. Moment Curvature Response.

The moment capacity, M_n = 1563.2 kNm (1153 kft.), is greater than the maximum AASHTO factored load of 1326 kNm (978 kft), thereby satisfying the ultimate limit state. The curvature capacity is considerably greater than the cracking curvature and equals 1.34×10^{-5} rad/mm (3.36×10^{-4} rad/in.). Such a large post-cracking curvature originates from the lower elastic modulus of the AFRP bars, compared to conventional steel, which enhances the flexural deformability of the girder. The numerical analysis was conducted using the fiber element method, where the results reasonably match the experiment.

Figure 6-2 shows the experimental and analytical load-deflection graphs possessing a similar pattern to the moment-curvature response, linear before and after cracking. The results show the cracking and ultimate loads equal to P_{cr} = 197.5 kN (44.4 kips) and P_u = 569.8 kN (128.1 kips), respectively. Given the analytical moment-curvature relationship, the load-deflection response was numerically calculated using the conjugate beam theory, where the results match the

experiment, showing the high fidelity of the analysis. The linear trend of the load-deformation response of the specimen prior to failure implies that the compressive concrete within the deck could not develop considerable inelastic stresses.

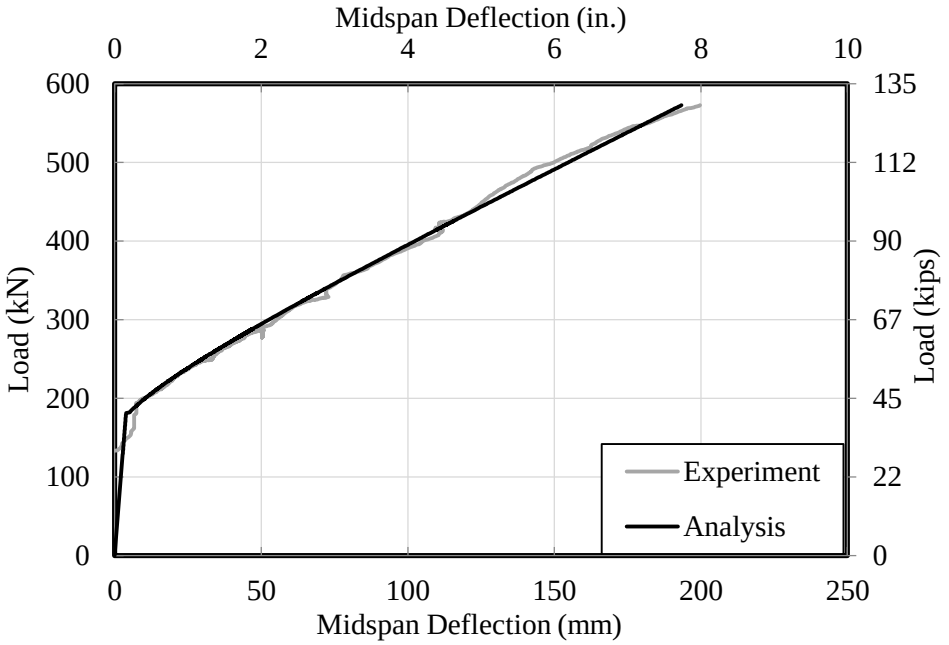

Figure 6-2. Load Deflection Response.

The deflection of the girder under the vehicular live load, M_L = 550 kNm (405 kft.) equivalent to P_L = 200 kN (45 kips), is equal to 11 mm (0.44 in.), which is less than the girder's length over 800 equivalent to 14.8 mm (0.58 in.), thereby satisfying the deflection-related serviceability limit state according to the AASHTO *LRFD Bridge Design Specification* (AASHTO 2010).

6.2.2 Failure Mode and Cracking Pattern

Flexural cracks were observed at the midspan upon reaching the cracking load, and then propagated beyond the constant moment region (shear span) as the load was monotonically increased. In the shear span, the flexural cracks were inclined due to the presence of shear and propagated toward the end supports. The crack spacing was between 152.4 mm (6 in.) and 203.2 mm (8 in.), which is close to the stirrup spacing. Because the shear-span-to-depth ratio (a/d = 6.9) was close to 7, the beam was categorized as a very slender beam (Park and Paulay 1975), and hence the failure mode of the girder was expected to be mostly governed by flexure

or beam action. Such a failure mode was confirmed by the test where the girder failed due to tendon rupture before the compressive concrete within the topping deck could reach a strain capacity of −0.003.

Figure 6-3 presents the cracking pattern at three different load levels: close to cracking, post-cracking, and prior to failure. A grid net of vertical lines with a 305-mm (12-in.) spacing was used to map the cracks. After a load level of P = 300 kN (67.4 kips), the flexural cracks at the midspan began to enter the topping deck labeled from A to Q. The extensive flexural cracks with considerable width, particularly at the midspan, provided enough warning to imply an impending failure. As discussed in Chapter 2, the failure mode of the girder was predicted as tendon rupture since the reinforcement ratio was considerably less than the brittle ratio and the section was categorized as an under-reinforced section. A close view of the failure zone at the bottom flange with tendon rupture is presented in Figure 6-4.

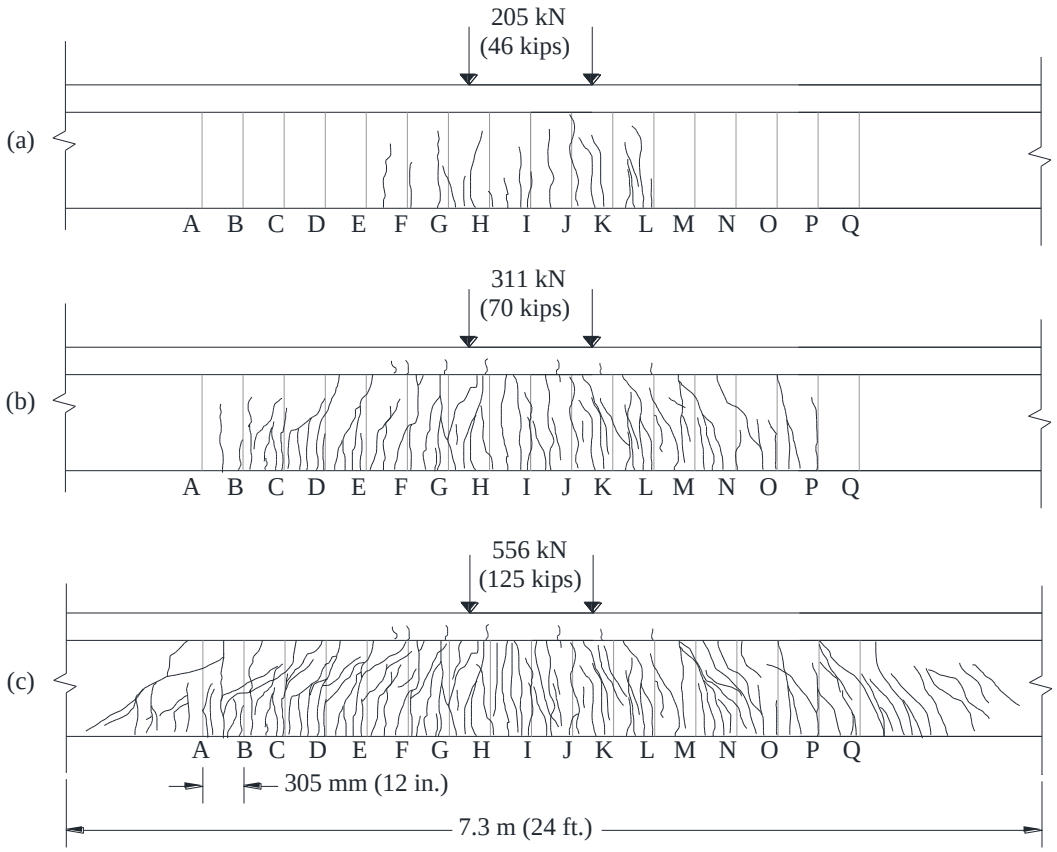

Figure 6-3. Crack Pattern at Different Load Levels: (a) Cracking, (b) Post-cracking, and (c) Prior to Failure.

Figure 6-4. Tendon Rupture at the Bottom Flange as the Failure Mode.

6.2.3 Strain Measurement

During the test, strain was measured at different locations over the height of the section, including at the most-top fiber of the section, at the bottom of the girder, and at the top of the girder underneath the deck. By knowing the strain at the top and bottom fibers of the section, curvature could be computed assuming the plane section remained plane after bending. The strains were measured using LVDTs distributed within and beyond the constant moment region. Figure 2-10 shows the layout of the LVDTs with a gage length of 609.6 mm (24 in.). The strain can be measured if the output of the LVDT is divided by the gage length.

As shown in Figure 6-5, the experimental results show that the maximum compressive stress within the topping deck is approximately equal to −0.002, which is physically less than the strain capacity of −0.003. Thus, concrete crushing was not the failure mode of the girder. On the other hand, the maximum tensile strain was observed at LVDTs #7, #8, and #9 as expected. The strains at LVDTs #7 and #9, which are beyond the theoretical constant moment region, are interestingly somewhat greater than those at #9, which is right at the constant moment region. This can be justified by recalling the actual constant moment region and considering the effect of inclined shear cracks. In other words, the actual constant moment region is longer than the theoretical constant moment region; therefore, the total tension in the constant moment region including LVDTs #7, #8, and #9 is constant. Since more flexure-shear cracks passed through LVDTs #7 and #9 compared to #8, the contribution of the concrete to bear tension, called tension stiffening, was less. Therefore, the strain in the AFRP tendons and the subsequent crack widths at LVDTs #7 and #9 were somewhat larger than those of LVDT #8. The maximum tensile strain at LVDT #7 seems to be equal to 0.016. This strain includes the strain due to AFRP tendons plus the

slippage of the tendons with respect to concrete due to de-bounding. As discussed in Chapter 2, the strain capacity of the AFRP tendons left for flexure was estimated at about 0.0125, accounting for the effect of prestressing and loss in prestressing force.

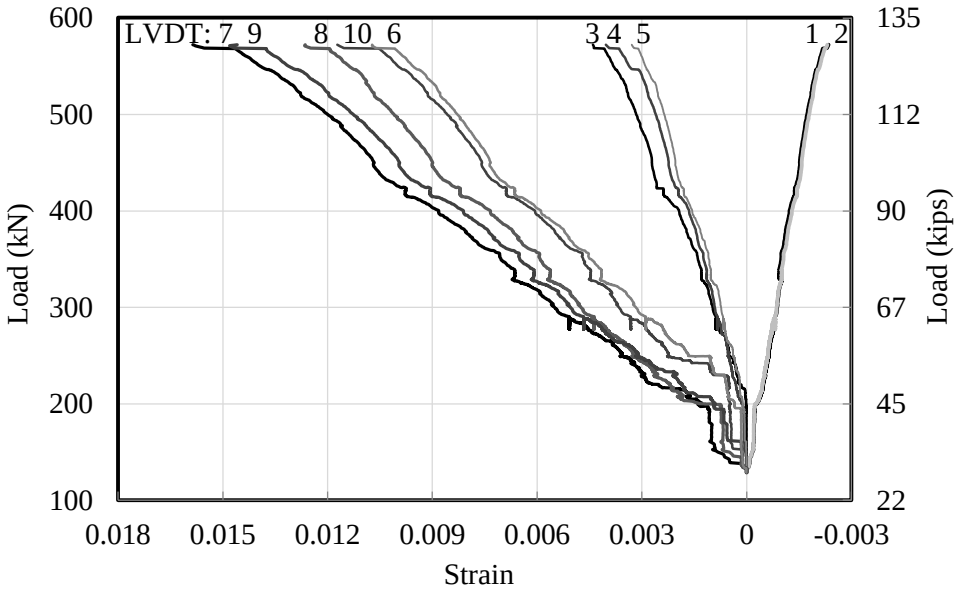

Figure 6-5. Strain at Different Locations over the Height of the Section.

6.2.4 Deflection Profile and Curvature Distribution

To better understand the flexural response of the AFRP prestressed girder, the experimental and analytical deflection profile and curvature distribution are studied here. The experimental deflections were recorded through the string pots, as discussed in Chapter 2. The experimental curvatures were calculated based on the experimental deflections using the finite difference method. Knowing the curvature distribution provides insight into the deflection calculations, where the serviceability requirements need to be satisfied.

Figure 6-6 and Figure 6-7 present the deflection profile and curvature distribution graphs for two different post-cracking load levels. The experimental and analytical results are in good agreement and show small negative curvatures close to the end supports. Further investigation revealed that these negative curvatures are due to a small amount of friction at the end supports going on between the concrete girders and rubber pads. This friction was accounted for in the numerical analysis.

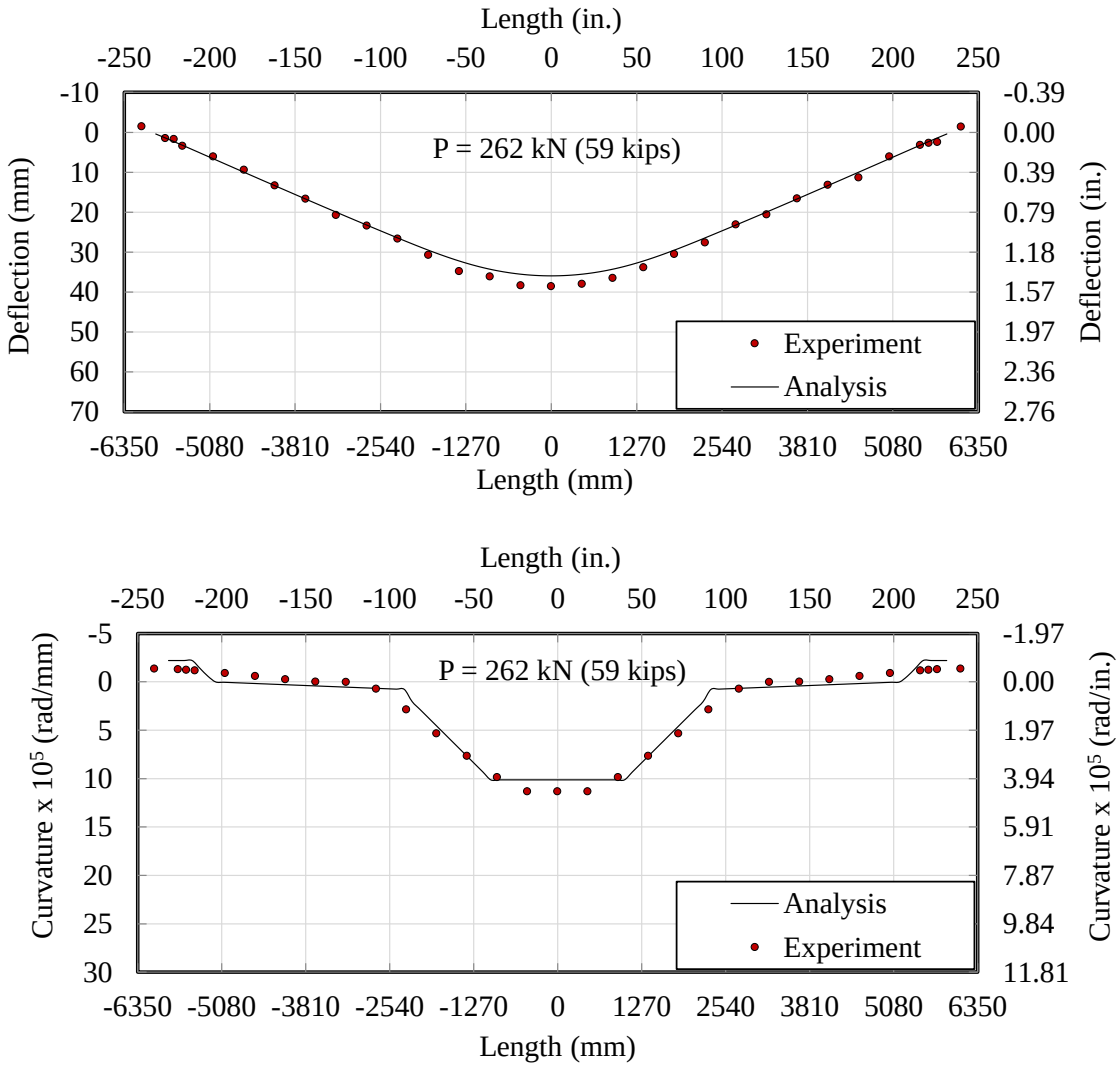

Figure 6-6. Deflection Profile and Curvature Distribution along the Girder P = 262 Kn (59 kips).

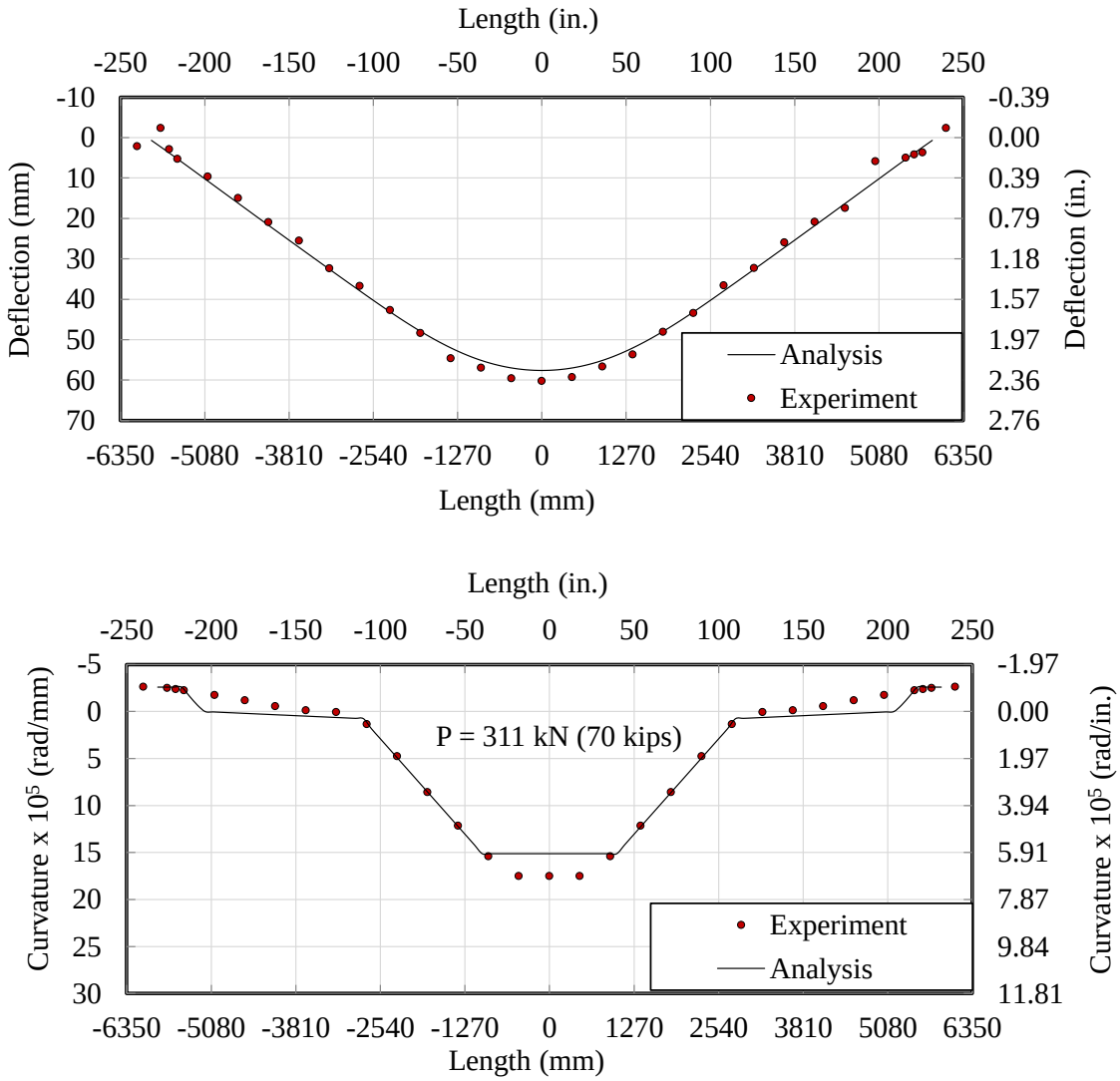

Figure 6-7. Deflection Profile and Curvature Distribution along the Girder P = 311 kN (70 kips).

The effect of the inclined shear-flexure cracks was also accounted for to adjust the constant moment region and compute the curvatures. The analysis underestimated the deflection for about 6 percent of the experimental values. This is basically due to a small difference between the analytical and experimental curvatures at midspan, as apparent in curvature distribution graphs. As noted in Figure 6-1, the experimental results showed a small shift in curvature once the specimen was cracked, which is not seen in the numerical analysis assuming a perfect bound between the AFRP bars and concrete.

The results confirm that a bilinear moment-curvature relationship for the AFRP prestressed section accurately predicts the curvature and deflection at the shear span and somewhat (6 percent) underestimates them at the midspan.

6.2.5 Comparison with Control Specimen

Figure 6-8 shows the comparative moment-curvature graphs for AFRP and control specimens. Due to less prestressing force applied in the AFRP specimen, the cracking moment of the control specimen was greater; however, the moment capacities of both specimens were almost equal. As opposed to the AFRP specimen, where the failure mode was due to tendon rupture, the failure mode of the control specimen was due to crushing of the compressive concrete at the topping deck (Trejo et al. 2008). For the control specimen, the steel prestressing strands began to yield when the cracking load was exceeded, and the neutral axis gradually shifted upward to resist the load applied. Since the strain capacity of the steel reinforcement was considerably large, between about 0.2 and 0.3, the upward shift of the neutral axis continued until the strain capacity in the compressive concrete was achieved and the specimen failed in a flexural manner due to concrete crushing. The moment capacities of both specimens, M_n = 1563.2 kNm (1153 kft.), were about 18 percent greater than the maximum factored AASHTO load of M_u = 1326 kNm (978 kft.).

Although the AFRP specimen exhibited a linear post-cracking behavior, as opposed to the ductile post-cracking response of the control specimen, the curvature capacities of both specimens were very close, which implies a large deformability of the AFRP specimen. Similar to the classic ductility concept commonly used for steel-reinforced concrete sections, the ductility concept is defined for FRP concrete sections, which indicates the ability to bear post-cracking deformations prior to failure.

Figure 6-9 presents the comparative load-deflection graphs of the AFRP and control specimens. The load and deformation capacities of both specimens were very close; however, the control specimens exhibited a greater cracking load due to a greater prestressing force. The considerable deformability provided by the AFRP specimen lies in the lower elastic modulus of AFRP bars over the steel strands, about one-third. Due to the lower elastic modulus of AFRP bars, the post-cracking flexural stiffness decreased, and the deflection increased subsequently. As long as the deflection is lower than the allowable value and the serviceability requirement is

satisfied, the deformability provided is appealing for the design engineer because extensive flexural cracks can develop, which indicate an impending failure.

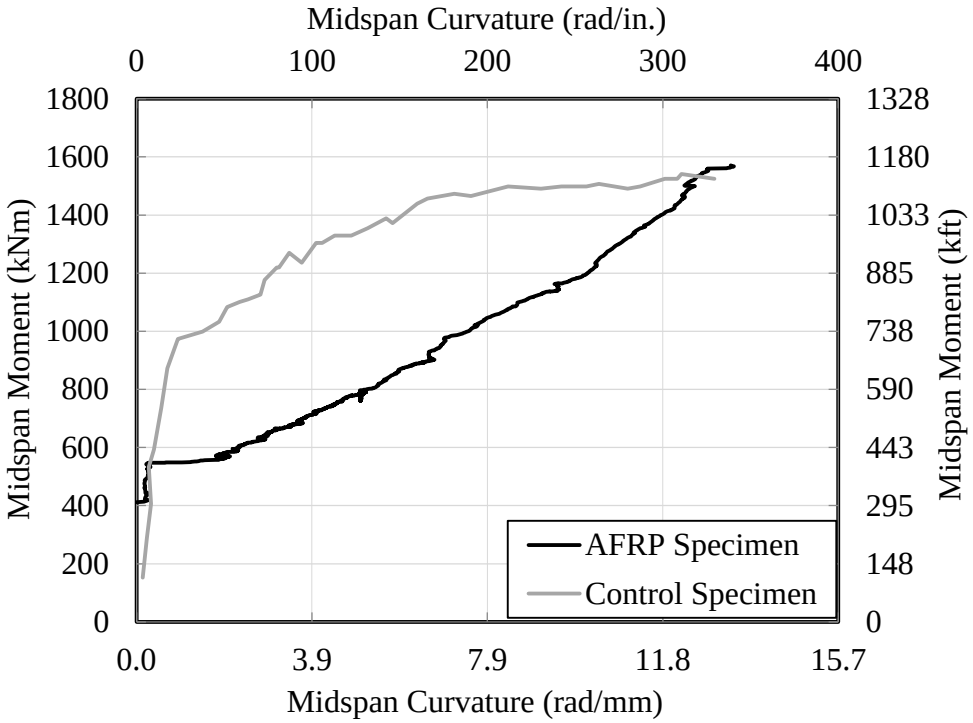

Figure 6-8. Comparative Moment-Curvature Graphs for AFRP and Control Specimens.

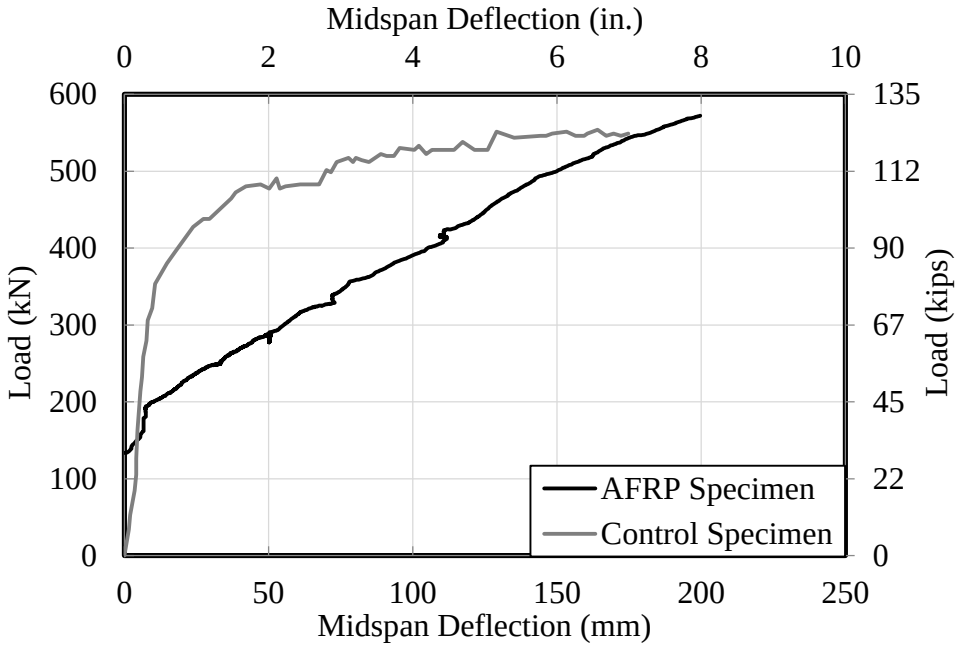

Figure 6-9. Comparative Load-Deflection Graphs for AFRP and Control Specimens.

Figure 6-10 shows the comparative flexural crack pattern for both AFRP and control specimens prior to failure starting from the midspan and then propagating toward the end supports, where the flexural cracks became inclined in the shear span due to the presence of shear force. The AFRP specimen exhibited more extensive flexural cracks over the control specimen, which provided a considerable deformability and sufficient warning of an impending failure. In the control specimen, however, the ductility was provided by yielding of the steel prestressing strand between the cracks, which indeed prevented larger crack extension. Since the stirrup spacing in the AFRP specimen (away from the support) was 203 mm (8 in.), the flexural cracks in the shear span were more inclined compared to those in the control specimen where the stirrup spacing was 150 mm (6 in.).

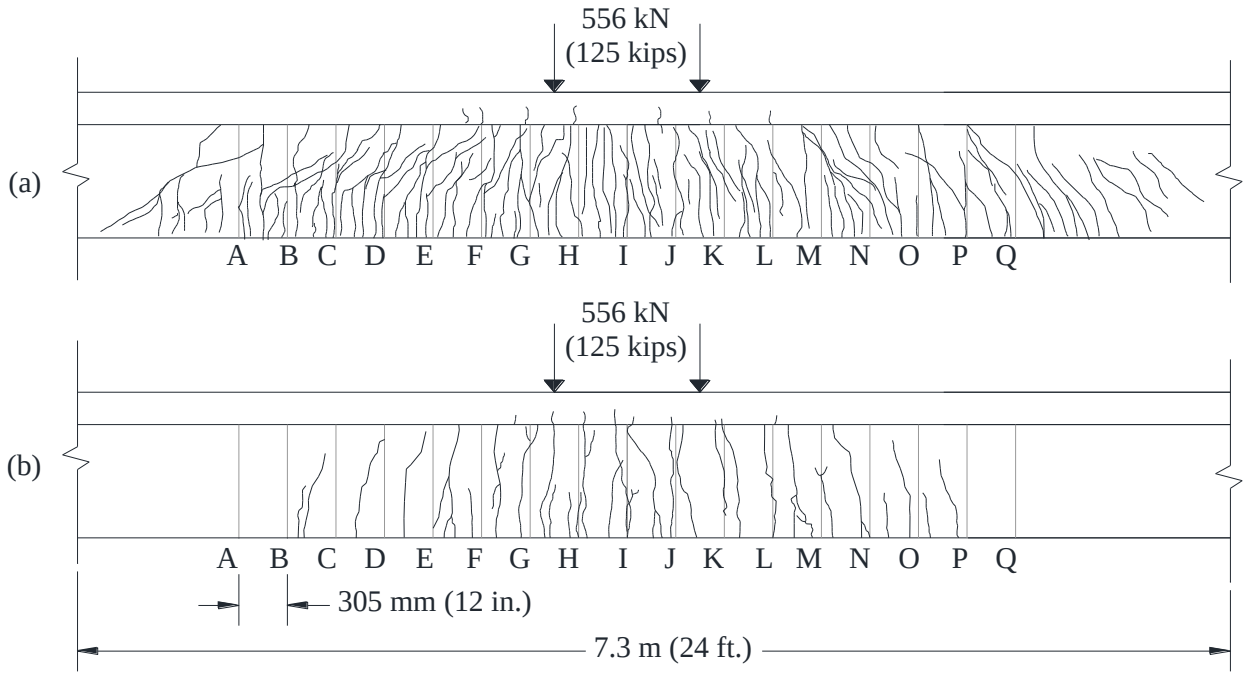

Figure 6-10. Comparative Crack Pattern under Flexure Test: (a) AFRP Specimen and (b) Control Specimen.

6.3 Shear Test

As explained in Chapter 2, two shear tests were conducted at both uncracked ends of the AFRP specimen. In shear test 1, the concentrated load was located 1.78 m (70 in.) away from the right end support of the girder. Eight LVDTs were mounted on both sides of the girder's web, four at each side, where the center of the LVDTs was located 813 mm (32 in.) away from the

support. LVDTs were mounted to measure the strain at the girder's web in *x*, *y*, and two diagonal directions, each with a 45° inclination angle. The second shear test was similarly conducted; however, the concentrated load and the center of the LVDTs were respectively located 1.5 m (60 in.) and 686 mm (27 in.) away from the left end support of the girder.

6.3.1 Shear Load Capacity

Figure 6-11 presents the location of LVDTs on the girder's web to measure tensile and compressive strains. The load was monotonically increased at a rate of 44.5 kN/min (10 kips/min) until shear failure occurred. In shear test 1, the cracking began at about 900 kN (202 kips), and shear failure happened at 1149 kN (258 kips) when the web of the girder crushed due to the compressive stresses developed via arch action. In the second shear test, where the concentrated load was closer to the end support, the cracking began at 934 kN (210 kips), and shear failure happened at 1218 kN (274 kips) when the web of the girder crushed as a result of compressive forces due to arch action between the load point and support. In both shear tests, the shear load capacity was almost twice the maximum factored AASHTO shear load of V_u = 566.12 kN (127.275 kips), as discussed in Chapter 2.

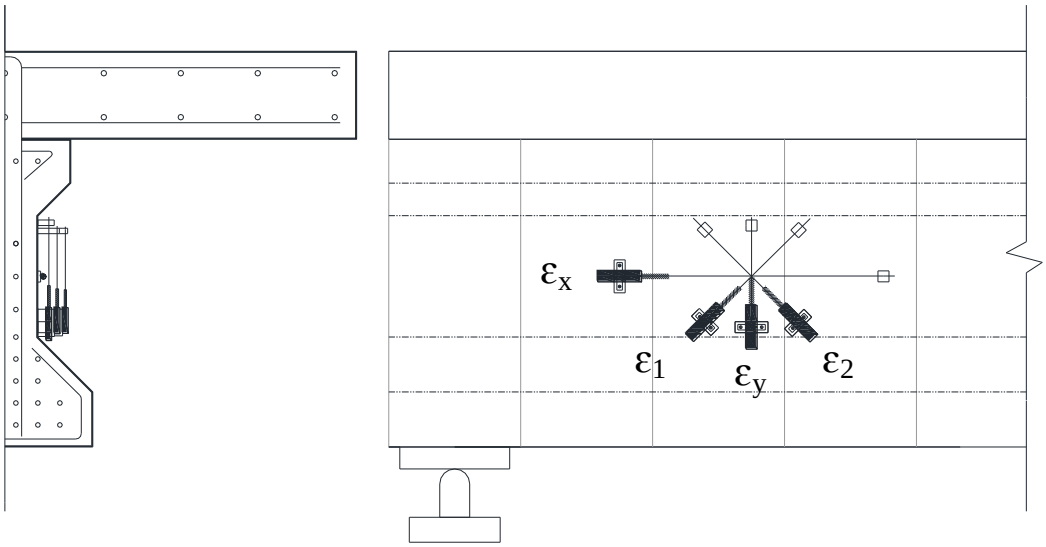

Figure 6-11. LVDT Layout.

6.3.2 Crack Pattern and Strain Measurement

Figure 6-12 shows the crack pattern for both shear tests at different load levels prior to failure. Greater load capacity was observed in the second shear test because the concentrated

load was closer to the support, and the arch action was fully developed. This was implied by the crack pattern where more disturbed regions with lesser crack spacing, compared to shear test 1, were observed between the load and support.

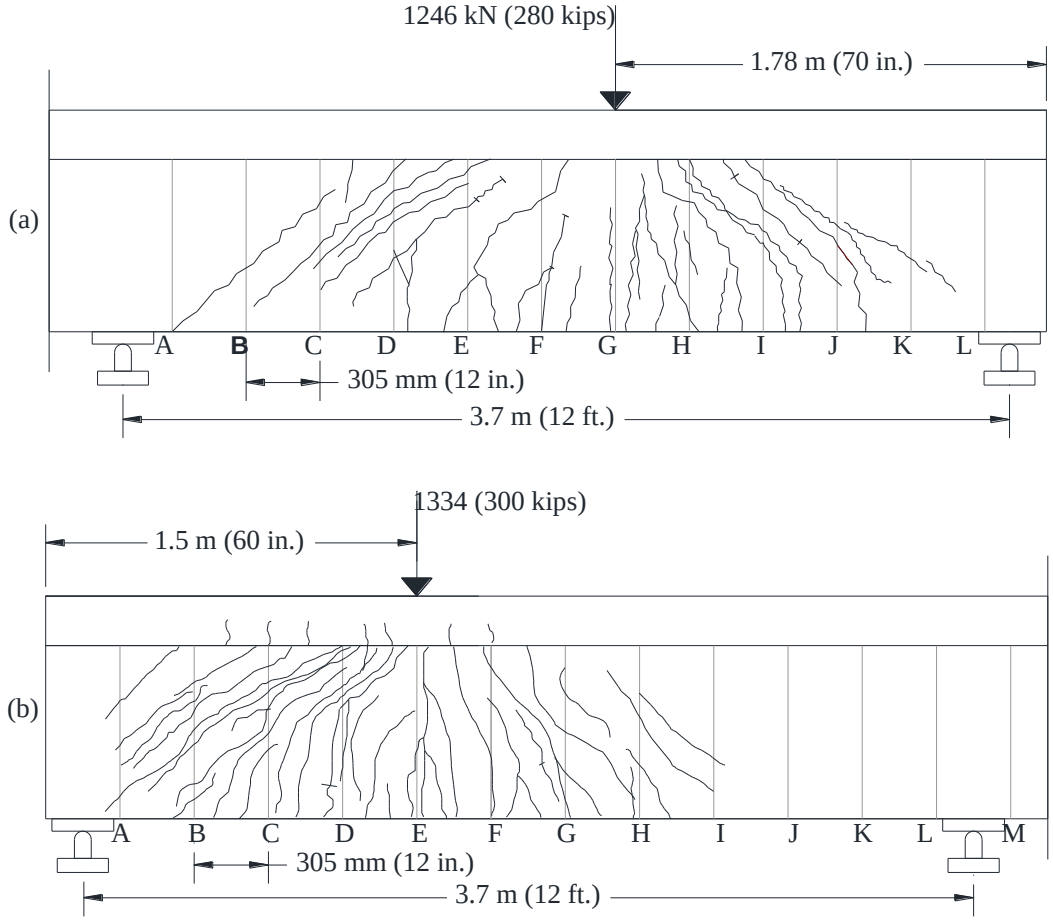

Figure 6-12. Crack Pattern under Shear Tests: (a) Shear Test 1 and (b) Shear Test 2.

The tensile and compressive strains in *x*, *y*, and diagonal directions were respectively ε_x = +0.0013, ε_y = +0.0021, ε_1 = +0.0019, and ε_2 = −0.0002 for shear test 1. For the second shear test, considerably greater values of strains were measured due to complete shear failure of the girder: ε_x = +0.0068, ε_y = +0.0089, ε_1 = +0.0116, and ε_2 = −0.0004.

6.3.3 Comparison with Control Specimen

The control specimen was also tested similarly to the first shear test of the AFRP specimen. The failure mode was similarly the crushing of the girder's web due to the compressive stresses transferred through the arch action between the point load and the support. The control specimen

failed at 1290 kN (290 kips), 3 percent more than that of the companion AFRP specimen. The similar behavior of both specimens is because of the governing arch action, which is mostly affected by the section geometry and concrete compressive strength, rather than the reinforcement.

The shear test confirmed that the development length of AFRP prestressed tendons was enough to sustain the tensile force as a balance to the horizontal components of the diagonal compression. Moreover, the AFRP stirrups provided sufficient lateral confinement for the arch action, similar to the steel stirrups. The crack patterns corresponding to the AFRP specimen and control specimen is displayed in Figure 6-13.

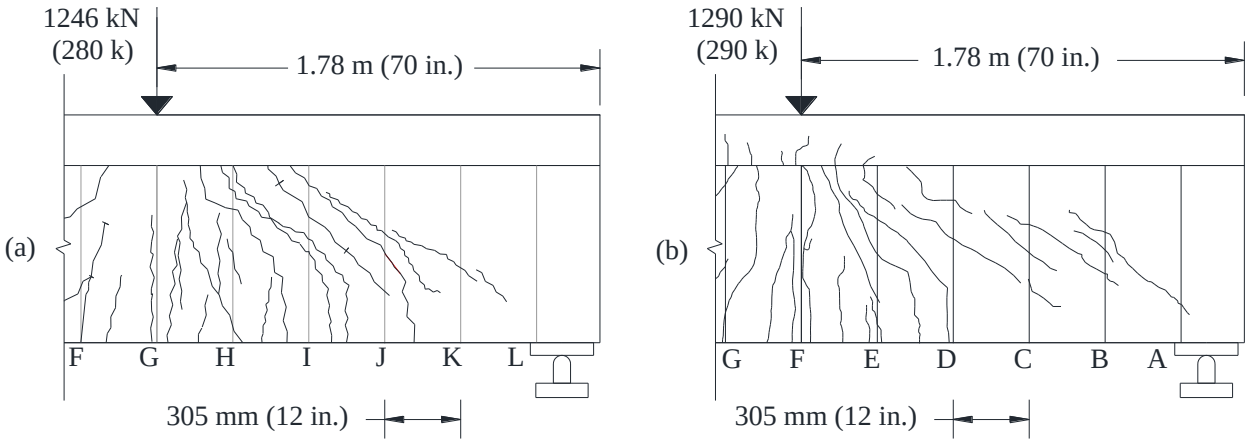

Figure 6-13. Crack Patterns under Shear Tests: (a) AFRP Specimen and (b) Control Specimen.

7 CONCLUSIONS

An FRP prestressed concrete girder (AASHTO I-girder Type I) was experimentally investigated under full-scale flexure and shear tests to evaluate its structural performance. AASHTO LRFD criteria were used to design the specimen and to evaluate the experimental results. The results were also compared with a companion control specimen prestressed with conventional steel strands. The major conclusions are as follows:

- This experimental research showed that the conventional steel reinforcement of prestressed concrete girders, either prestressing strands or reinforcing steel rebar, can be successfully replaced with equivalent AFRP bars, where the serviceability and ultimate limit states of design are satisfied.
- The moment capacity of both AFRP and control specimens was equal to M_n = 1563.2 kNm (1153 kft.), which is about 18 percent more than the maximum factored AASHTO load of M_u = 1326 kNm (978 kft.); therefore, the ultimate limit state of design was met.
- The cracking moment of the AFRP specimen was equal to 542.3 kNm (400 kft.), which is less than the unfactored live load plus dead loads of barrier and future wearing, 611 kNm (450 kft.); therefore, the girder, as opposed to the control specimen, was categorized as a partially prestressed beam. It was difficult to provide a fully prestressed girder due to the limited capacity of the prestressing anchorage system used for AFRP bars.
- Since the AFRP specimen was partially prestressed, the moment-curvature response showed a small flat plateau upon cracking, which resembled a trilinear behavior including pre-cracking, cracking, and post-cracking stages. The load deflection behavior, however, showed an approximate bilinear trend.
- The failure mode of the AFRP specimen was tendon rupture at the bottom flange of the girder, as opposed to the control specimen where the failure mode was due to concrete crushing preceded by yielding of the steel, which provided enough ductility. However, due to the lower elastic modulus of AFRP bars over conventional steel, extensive flexural cracks and larger deflections at load levels greater than the service

load provided sufficient deformability, implying a warning of impending failure. Both the AFRP and control specimens exhibited a similar deformation capacity equal to 1.34×10^{-5} rad/mm (3.36×10^{-4} rad/in.).

- Since the AFRP specimen was partially prestressed, the deflection of the girder under the vehicular live load of M_L = 550 kNm (405 kft.), 11 mm (0.44 in.), was close to the serviceability limit of *l/800* = 14.8 mm (0.58 in.) per the LRFD *Bridge Design Specification* (2010) but was still acceptable. Hence, the deflection under service load is recognized as critical for design.
- At post-cracking load levels, the curvature distribution over the length of the AFRP girder followed a bilinear trend approximately. However at the midspan zone, the experimental curvatures were up to 15 percent greater than the bilinear model.
- Two shear tests revealed the shear capacity of the AFRP prestressed girder to be almost twice the maximum factored AASHTO shear load of V_u = 566.12 kN (127.275 kips), where the failure mode was crushing of the girder's web due to compressive stresses transferred from the loading point to the support through an arch action. The control specimen showed a shear capacity 3 percent greater than that of the AFRP specimen; however, the crack pattern and failure mode were quite similar to the AFRP case.
- The combination of AFRP R-bars as stirrups and high-strength steel bolts as shear studs was satisfactory to provide enough shear resistance at the girder-to-deck interface; therefore, a full composite action was achieved.
- A high strength-to-weight ratio is one of the major advantages of AFRP bars over conventional steel. Implementation and placement of lightweight AFRP bars made the construction easier and quicker. The main construction challenge is to use an appropriate anchorage system that suits both the design and construction requirements. The average prestressing level achieved by the anchorage system that was developed for this project was about 45 percent of the AFRP ultimate capacity.

The following items are recommended for further research and future work:

- Since this project investigated and verified the adequacy of structural performance under instantaneous loading (short term), the long-term structural performance of the AFRP girder needs to be verified as well.
- To increase the flexural strength and deformability of AFRP prestressed girders, the researchers recommend concentrically prestressing the girder and reinforcing it with non-prestressed AFRP bars at the bottom fibers of the section.
- In this project, the shear resistance between the deck and girder was provided through a combination of AFRP R-bars as stirrups and high-strength steel bolts as shear studs. Further research is required to see if AFRP R-bars as stirrups are adequate to bear the entire horizontal shear at the girder-to-deck interface.
- Although the flexural behavior was successfully predicted and verified through numerical analysis, a reliable method to compute the shear capacity is needed. A compatibility strut and tie model is recommended to be studied for FRP application.

REFERENCES

AASHTO. (2010). AASHTO LRFD Bridge Design Specification. 5th Edition, Washington, D.C.

Abdelrahmaan, A. A., G. Tadros, and H. S. Rizkalla (1995). "Test Model for the First Canadian Smart Highway Bridge." *ACI Structural Journal*, 92(4): pp. 451–458.

Abdelrahmaan, A. A., and H. S. Rizkalla (1997). "Serviceability of Concrete Beams Prestressed by Carbon Fiber-Reinforced-Plastic Bars." *ACI Structural Journal*, 94(4): pp. 447-454.

Al-Mayah, Adil, Khaled Soudki, and Alan Plumtree (2001a). "Experimental and Analytical Investigation of a Stainless Steel Anchorage for CFRP Prestressing Tendons." *PCI Journal*, March–April.

Al-Mayah, Adil, Khaled Soudki, and Alan Plumtree (2001b). "Mechanical Behavior of CFRP Rod Anchors under Tensile Loading." *Journal of Composites for Construction*, May.

Al-Mayah, Adil, Khaled Soudki, and Alan Plumtree (2005). "Effect of Sandblasting on Interfacial Contact Behavior of Carbon-Fiber-Reinforced Polymer-Metal Couples." *Journal of Composites for Construction*, July/August.

Al-Mayah, Adil, Khaled Soudki, and Alan Plumtree (2006). "Development and Assessment of a New CFRP Rod-Anchor System for Prestressed Concrete." *Springer*, August.

Al-Mayah, Adil, Khaled Soudki, and Alan Plumtree (2007). "Novel Anchor System for CFRP Rod: Finite-Element and Mathematical Models." *Journal of Composites for Construction*, September/October.

ASTM C138. (2009). Standard Test Method for Density (Unit Weight), Yield, and Air Content of Concrete. In *Annual Book of ASTM standards.* West Conshohoken, Pennsylvania: The American Society for Testing and Materials.

ASTM C1611. (2009). Standard Test Method for Slump Flow of Self-Consolidating Concrete. In *Annual book of ASTM standards.* West Conshohocken, Pennsylvania: The American Society for Testing Materials.

ASTM C31. (2003). Standard Practice for Making and Curing Concrete Test Specimens in the Field. In *Annual book of ASTM standards.* West Conshohocken, Pennsylvania: The American Society for Testing and Materials.

ASTM C39. (2004). Standard Test Method for COmpressive Stregnth of Cylindrical Concrete Specimens. In *Annual book of ASTM standards.* West Conshohoken, Pennsylvania: The American Society for Testing and Materials.

ASTM C469. (2010). Standard Test Method for Static Modulus of Elasticity and Poisson's Ratio of Concrete in Compression. In *Annual book of ASTM standards.* West Conshohoken, Pennsylvania: The American Society for Testing and Materials.

ASTM C496. (2011). Standard Test Method for Splitting Tensile Strength of Cylindrical Concrete Specimens. In *Annual book of ASTM standards.* West Conshohoken, Pennsylvania: The American Society for Testing and Materials.

ASTM C78. (2010). Standard Test Method for Flexural Strength of Concrete (Using Simple Beam with Third-Point Loading). In *Annual book of ASTM standards.* West Conshohoken, Pennsylvania: The American Society for Testing and Materials.

Bazant, Z. P., & Novak, D. (2001). Proposal for Standard Test of Modulus of Rupture of Concrete with Its Size Dependence. *ACI Material Journal*, 79-87.

Bennitz, A., Schmidt, J. W. (2012). Failure Modes of Prestressed CFRP Rods in a Wedge Anchorage Set-up. *ACIC*, 104-114.

Daczko, J. A. (2012). *Self-Consolidating Concrete: Applying What We Know.* New York: Spon Press.

Dolan, C. W.; & Burke, C. R. (1996). Flexural Strength and Design of FRP Prestressed Beams. *Proceedings of the Second International Conference on Advanced Composite Materials in Bridges and Structures (ACMBS2)*, Montreal, Quebec, Canada, 383-390.

Dolan, C.W. Nanni, A. Hamilton, H.R., & Bakis, C.E. (2001) Design Recommendations for Concrete Structures Prestressed with FRP Tendons. *FHWA, V. III: FRP Prestressing for Highway Bridges* Cont. DTFH61-96-C-00019.

Gutierrez, P. A., & Manuel, F. C. (1995). The modulus of elasticity of high performance concrete. *Materials and Structures*, 559-568.

Khayat, K. H. (1999). Workability, Testing, and Performance of Self-Consolidating Concrete. *ACI Materials Journal*, 346-354.

Lu, Z. (1998). Flexural Performance of Fiber Reinforced Polymer Prestressing Bars. M.S. Thesis, Pennsylvania State University, University Park, PA.

McKay, S., & Erki, M. A. (1993). Flexural Bahvior of Concrete Beams Pretentioned with Aramid Fiber Reinforced Plastic Tendons. *Canadian Journal Civil Engineering*, 688-695.

Naaman, A. E. (2004). Prestressed Concrete Analysis and Desingn: Fundamentals. 2nd Edition, Michigan, USA.

NACE. (2013). *Corrosion Cost of Highways and Bridges.* Retrieved from NACE International: http://www.nace.org/Corrosion-Central/highways-and-bridges/

Okamura, H., & Ouchi, M. (2003). Self-Compacting Concrete. *Journal of Advanced Concrete Technology*, 5-15.

Okamura, H., & Ozawa, K. (1996). Self-Compacting High Performance Concrete. *Structural Engineering International*, 269-270.

Park, R.; and Paulay, T. (1975). Reinforced Concrete Structures. *John Wiley & Sons*, New York.

Pincheira, J. & Woyak, J. Anchorage of Carbon Fiber Reinforced Polymer (CFRP) Tendons using Cold-Swaged Sleeves. *PCI Journal*. Nov-Dec (2001)

Pirayeh Gar, S. (2012). Structural Performance of a Full-Depth Precast Bridge Deck System Prestressed and Reinforced with AFRP Bars. PhD Dissertation, Texas A&M Univ., College Station, TX.

Pirayeh Gar, S. (2013). Comparative Experimental Performance of Bridge Deck Slabs with AFRP and Steel Precast Panels. *Journal of Composites for Construction*. Web. 26 Nov. 2013. <http://ascelibrary.org/doi/full/10.1061/(ASCE)CC.1943-5614.0000380>.

Rashid, M. A., Mansur, M. A. & Paramasivam, P., (2005). Behavior of Aramid Fiber-Reinforced Polymer Reinforced High Strength Concrete Beams Under Bending. *Journal of Composites for Construction*, 117-127.

SeshaPhani, S., Sekhar, S., Rao, S., & Sravana, P. (2013). Evaluation of Relationship Between Mechanical Properties of High Strength Self Compacting Concrete. *American Journal of Engineering Research*, 67-71.

Shahawy, M.A., & Beitelman, T. (1995). Static flexural response of members pretensioned with multiple layered aramid fiber bars. *Journal of Composites Part B: Engineering*, 253-261.

Shrive, N. G. (2000) Prestressing Anchorage System for Fiber Reinforced Plastic Tendons. U.S. Patent 6,082,063.

Toutanji, H. A. & Saafi, M. (2000). Flexural Behavior of Concrete Beams Reinforced with Glass Fiber-Reinforced Polymer (GFRP) Bars. *ACI Structural Journal*, 712-719.

Trejo, D. Hueste, M. B. Kim, Y. H. & Atahan, H. (2008) Characterization of Self-Consolidating Concrete for Design of Precast, Prestressed Bridge Girders. Report No. FHW A/TX-09/0-5134-2, *Texas A&M Transportation Institute,* College Station, TX, 1-364.

University of Washington. (n.d.). Retrieved from http://courses.washington.edu/me354a/chap5.pdf

Zhang, B. & Benmokrane, B. (2004). Design and Evaluation of a New Bond-type Anchorage System for Fiber Reinforced Polymer Tendons. *NRC Canada*. 14-26. Web. 25 Nov. 2013. <http://cjce.nrc.ca>.